USF Tampa Graduate Theses and Dissertations   USF Graduate Theses and Dissertations

10-14-2014

Investigation of Enhanced Titanium and Zinc Oxide Semiconductors for the Photodegradation of Aqueous Organic Compounds

Innocent Udom
University of South Florida, iudom@mail.usf.edu

Follow this and additional works at: https://digitalcommons.usf.edu/etd

Part of the Chemical Engineering Commons

Investigation of Enhanced Titanium and Zinc Oxide Semiconductors for the

Photodegradation of Aqueous Organic Compounds

by

Innocent Udom

A dissertation submitted in partial fulfillment
of the requirements for the degree of
Doctor of Philosophy in Chemical Engineering
Department of Chemical and Biomedical Engineering
College of Engineering
University of South Florida

Major Professor: D. Yogi Goswami, Ph.D.
John Kuhn, Ph.D.
Babu Joseph, Ph.D.
Elias Stefanakos, Ph.D.
Manoj K. Ram, Ph.D.
Sarina Ergas, Ph.D.
Aloysius Hepp, Ph.D.

Date of Approval:
October 14, 2014

Keywords: Photocatalysis, TiO2, ZnO, Phenol, Optimization

DEDICATION

To my wife, Kimberly, and Son, Gabriel; my father, Peter Okon Udom, and mother, Martha

Udom.

ACKNOWLEDGMENTS

TABLE OF CONTENTS

LIST OF TABLES

LIST OF FIGURES

v

ABSTRACT

Growing demand and shortages of potable water sources due to industrialization have become a great concern worldwide. Various approaches and solutions have been adopted to provide cleaner and quality water. In a preliminary study, a method of treating wastewater was investigated in which algae were used to remove nutrients (nitrogen and phosphorous) from wastewater and then the algae were harvested for use as a biofuel. The results from this investigation are included in the Appendix B. Employing traditional oxidants, such as hydrogen peroxide, chlorine, and ozone, for treatment of recalcitrant organic compounds have achieved less promising results. However, photocatalysis, an advanced oxidation process (AOP), which is a low-cost and high-efficiency technique, has been widely recognized as a promising approach for water purification and elimination of organic constituents in wastewater. Photocatalysis is the increase in the rate of a chemical reaction by employing a catalyst in the presence of photons. Generally, for a high performance photocatalyst, light of appropriate wavelength is used to activate a catalyst in close contact with contaminants, thereby modifying the rate of the reaction. The presence of these contaminants could pose potential health and environmental concerns, especially in a controlled environment such as on a space station or during long-term manned missions. Thus, the development of energy efficient and "green" technologies to reduce or eliminate organic constituents in wastewater has important potential applications.

This research investigated the supported semiconductor photocatalysts (TiO_2 and ZnO), particularly ZnO nanorods and nanowires, their synthesis methods, properties and

corresponding effectiveness in photocatalysis. The effect of transition metal co-catalysts on the photocatalytic properties of TiO_2 was investigated. Although TiO_2 is the most extensively studied photocatalyst for water decontamination, ZnO, as presented in this work, could be a substitute because of its lower cost, relative energy bandgap and higher visible light photoactivity. Both photocatalysts were doped and screened for the decomposition of model contaminates, rhodamine B (RhB), phenol and methyl orange, under ultraviolet and/or visible light irradiation. In the photodegradation of RhB, TiO_2/Ru 1% showed a superior photocatalytic activity relative to P25-TiO_2 under broad-band irradiation, while doped ZnO-Ag resulted in better photodegradation of methyl orange, compared to P25-TiO_2, under visible light irradiation.

The morphology and estimated chemical composition of photocatalysts were determined by energy dispersive spectroscopy (EDS) and scanning electron microscopy (SEM). Brunhauer, Emmett and Teller (BET) analysis was utilized to measure mass-specific surface area(s). A X-ray diffraction (XRD) study was carried out to confirm the identity of photocatalyst phase(s) present. The cause of low photocatalytic activity under an inert atmosphere, the simple effective fabrication technique of doped ZnO nanowires over TiO_2 and properties of the photocatalyst are also discussed.

CHAPTER 1: INTRODUCTION AND BACKGROUND

1.1 Introduction

Daily, an enormous amount of dyes and other organic chemicals produced by industrial processes are discharged into the environment. The presence of these contaminants in water causes considerable problems to aquatic ecosystems and public health [1-14].

Approximately 1-15% of the total dye produced in the world is wasted in the production process and released into the environment [15-17]. The discharge of these colored, contaminated wastewaters into the environment represents a significant cause of pollution and could create hazardous byproducts through chemical reactions occurring in the wastewater stream [17].

Decontamination of dyes in polluted wastewaters has therefore attracted increased attention and several purification methods have been proposed. Conventional treatment methods for textile wastewaters include coagulation, sedimentation, filtration and adsorption. Chemical oxidation processes, using chlorine, ozone, or electrochemical methods, have also been used. Problems with these processes include poor removal of color and trace organic compounds, production of chemical sludges that are difficult to dispose, and production of toxic by-products [18-21] [22, 23] . [24-26]. Forgacs et al. [27] reported that conventional wastewater treatment techniques have proven to be mostly unsuccessful for removing textile dyes from wastewater stream due to the resilient and stability of these pollutants.

―――――――――

[1]Portions of this chapter have been previously published (I. Udom, M.K. Ram, E.K. Stefanakos, A.F. Hepp, D.Y. Goswami, One dimensional-ZnO nanostructures: Synthesis, properties and environmental applications, Materials Science in Semiconductor Processing, 16 (2013) 2070-2083.)

A large amount of textile dyes are resistant to chemical and biological degradation to be mostly unsuccessful for removing textile dyes from wastewater stream due to the resilient and stability of these pollutants; they also verified that most of the azo dyes tested in their investigation was untreated after the activation sludge process. To summarize, the aforementioned processes have wide-ranging limitations in efficacy for the decontamination of dyes from industrial wastewater.

To minimize these limitations, advanced oxidation processes (AOPs), have received enormous research attention as innovative treatment techniques [28-33]. The rationale of these AOPs is based on the production of powerful oxidant for the decomposition of "stubborn" constituents of the dyes from industrial wastewater, pathogens and trace organics [34]. Among these AOPs, heterogeneous photocatalysis is a tertiary water treatment process and has attracted increased attention in the past decades, because of its ability to completely mineralize many target pollutants [35-40].

Heterogeneous photocatalysis semiconductor using catalysts (Fe_2O_3, CdS, TiO_2 and ZnO) have shown good effectiveness in photo-induced oxidation processes to decompose organic compounds and destroy pathogens, such as viruses and bacteria [41-44]. Over three decades, Titanium has become one of the significant candidates for photocatalysis and has been the most commonly studied as an environmentally friendly water treatment technology for the decontamination of organic compounds [45-49]. Titanium has been employed in the degradation of numerous organic compounds including acetaldehyde [50], acetone [51], chlorophenols [52], insecticides (e.g. monocrotophos) [53] and dyes (Rhodamine B *(RhB)* methyl orange [54-57]. Anatase, rutile and brookite are the main crystalline phases of Titania, while anatase and rutile both exhibit higher photocatalytic activity in mixed phase. Anatase, brookite and rutile have been

reported to be most stable nanoparticle within the range of < 11 nm, $11 - 35$ nm and < 35 nm, respectively [58]. Photocatalytic activities of TiO_2 are greatly enhanced when doped with transition metals and some non-metals. Doping shifts the optical adsorption edge, reduces recombination rates and improves charge transfer of titanium [59]. In addition, many studies have reported that the photoreactivity of doped titanium depended on the type, energy level and concentration of dopants, as well as the distribution of dopants within the titanium lattice and the light intensity. The doping of titanium with various metals and subsequent improvement in photocatalytic results are discussed in Chapter 2 of this work.

Zinc oxide could be a substitute to TiO_2 due to its similar band gap (BG) energy (3.3 eV) [60] with titanium (3.2eV) [61] and comparatively lower cost of production [62-64]. In comparison with TiO_2, ZnO is a better candidate due to the numerous point defects mainly from oxygen vacancies, higher production of hydroxyl ions and relatively greater rate of reaction. In addition, ZnO has been found to be safe and biocompatible for most environmental applications [65-69].

Figure 1 depicts schematic crystal structures of three ZnO phases: wurtzite, zinc blende and rocksalt. Generally, under normal conditions, the wurtzite structure is the most stable, while rocksalt structures may be fabricated at high pressure and the zinc blende structure can only be synthesized on cubic substrates. Wurtzite, a hexagonal crystal system belonging to the space group C6v4 (No. 186, P6$_3$mc), possesses two lattice parameters a=3.2495Å and c=5.2069 Å with a ratio of c/a = 1.60. This axial value correlates with the ratio (1.633) of an ideal crystal [64][70]. Although ZnO exhibits a slight covalent bonding, the ionic character in the Zn-O is very strong. It has facets that exhibit massive surface reconstruction unlike the basal plane [71-74]. ZnO reveals a number of novel structures by modifying the fabrication conditions. One of the major

factors that predict the morphology of the fabricated structure is the relative surface activity

under controlled growth conditions. However, three dimensional and well-defined crystallites

with low index crystallographic faces can be developed during growth after an initial phase of

seed layer formation [74].
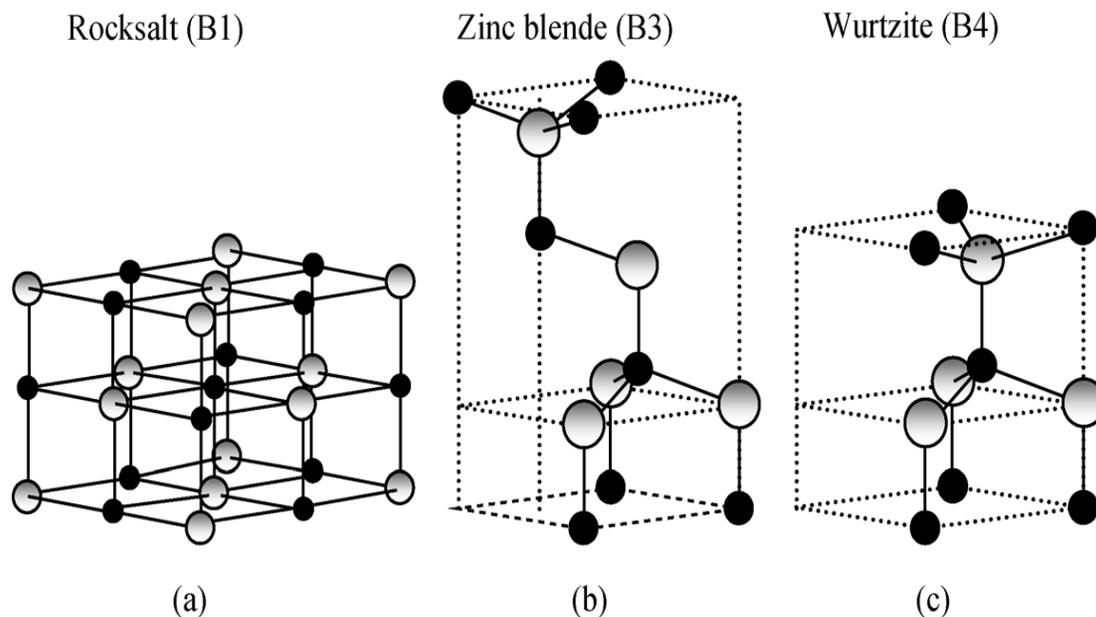
Figure 1 Stick-and-ball representation of ZnO crystal structures. (a) cubic rocksalt (B1), (b) cubic zinc blende (B3), and (c) hexagonal wurtzite (B4). Shaded gray and black spheres denote Zn and O atoms, respectively. (Reproduced with permission from [70] Copyright @ 2009 WILEY-VCH

The review presented in Chapter 2 of this dissertation assesses recent studies on ZnO

nanowires, with an emphasis on one-dimensional (1D) ZnO-based nanostructures employed as

photocatalysts for the decomposition of environmental contaminants, particularly textile and

industrial dyes under appropriate light irradiation. In this work, we have investigated different

ZnO photocatalysts, discuss their properties, and highlight fabrication techniques for the ZnO

nanowire (nanorod) and its characterization. We also present the photocatalytic degradation of selected contaminants (dyes) using the 1D-ZnO based photocatalyst.

The long term goal of this work is to develop a simple and commercial photocatalyst for the degradation and decontamination of organic pollutants in an aqueous matrix under visible irradiation. The overall objective of this research is the preliminary development of a new photocatalyst and illustration of photocatalysis as an effective technique for the decontamination of organic materials in wastewaters.

The overall objective will be achieved via the successful accomplishment of the following specific goals: (1) investigate the effect of a transition metal dopant in photocatalytic materials, (2) develop a simple, inexpensive, scalable and effective Ag-ZnO nanowire (NW) photocatalyst by modifying the morphology via a synthesizing method, and (3) optimize the photocatalytic degradation of phenol using simple photocatalytic reactor.

Although this research was not carried out with real textile wastewater, studies have shown that wastewater originating from the textile industry contains unreacted dyes, dispersing agents, surfactants, salts and organics. Generally, the wastewater is characterized by high pH variation (2-12), elevated total dissolved solids, chemical oxygen demand (COD) and color density [23].

In real textile wastewaters, surfactants could compete with other solutes for reactive sites at the surface of the photocatalyst, which could influence the photocatalytic degradation of the target compound. Other compounds in the matrix, such as dissolved organic matter and salts, can reduce the hydroxyl radicals produced at the photocatalyst surface resulting in lower photocatalytic performance. Dissolved oxygen presents an opposite effect, enhancing photocatalytic activity, by acting as electron scavenger, resulting in improved parting of

electron–hole and allowing for more proficient movement of the charge carriers into the photoreaction sites.

Finally, in order to optimize the efficiency of photocatalysis in the removal of colors from real textile wastewater, it is paramount that upstream treatment processes be applied prior to photocatalysis. Figure 2 outlines how the proposed alternative can be approached. The figure illustrates pretreatment of dye-containing wastewater by the addition of coagulants to facilitate the removal of dissolved and suspended solid by coagulation, flocculation and sedimentation. Afterward, the discharged water is biologically treated to reduce chemical oxygen demand (COD) and nutrients. The pH of the treated wastewater is then adjusted and the wastewater is aerated to achieve the optimal photocatalytic performance.
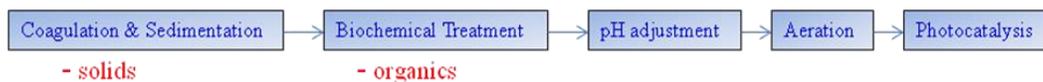
Figure 2 Alternative photocatalytic purification train for textile wastewater

1.2 Photocatalysts

Photocatalysis is the enhancement of a chemical reaction using a catalyst under light irradiation. Generally, the catalysts participate in and accelerate the reaction but remain unaltered at the end of the reaction. The catalyst uses the characteristics of semiconductors in a photochemical reaction to decompose organic pollutants [75]. The semiconductor possesses a band gap which separates the electron-packed valence band (VB) from the empty conduction band (CB) (Fig. 2). When a photon's energy ($h\nu$) is greater than the band gap energy, it excites an electron from the valence band to the conduction band , thereby, producing an electron (e^-) and a positive hole (h^+), in the CB and VB, respectively. The electron (e^-) and hole (h^+) both

6

migrate to the catalyst surface to recombine or facilitate a redox reaction with compounds absorbed on the catalyst. A powerful hydroxyl radicals (OH·), is produced from the combination of H_2O and/or H_2O_2 with the positive hole (h^+), that oxidize the organic compounds in the photocatalytic system. Simutaneously, oxygen atoms absorbed on the photocatalyst are reduced by the electrons in the conduction band [76, 77].

As illustrated in Fig. 3, during the photocatalytic process, superoxide radical (O_{2-}), and other reactive groups are produced, resulting from reactions with moisture oxygen (O_2). Although ZnO and TiO_2 have similar bandgaps and low production cost, more recently, ZnO has been investigated by a large body of researchers due to its higher photoactivity (by a factor of 2-3) in visible light irradiation for the decontamination of water [78, 79]. Furthermore, due to
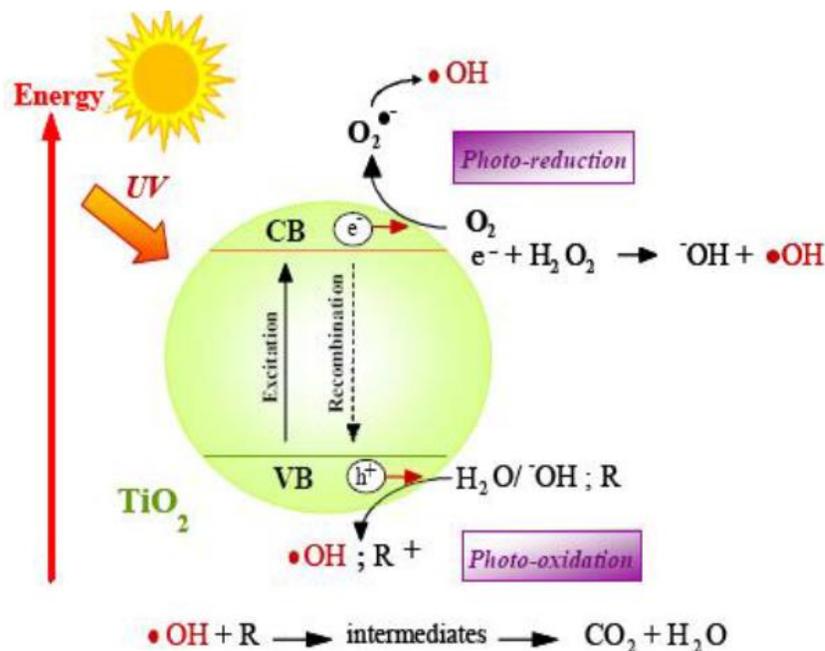
Figure 3 A schematic of the principle of photocatalysis (reproduced with permission from [52] © 2010 Elsevier)

ZnO's higher efficiency in the production of hydroxyl radicals (OH·) and reduced recombination of photoinduced electron-hole pairs, it has been considered to be more photoactive [80-86].

Generally, the surface area as well as the number of defects on the surface of the catalyst are significant for effective photochemical reaction. Although nanoparticles offer a larger surface area, they are limited in their use in a water suspension because of the dificulty and high cost of separation and recovery. One dimensional (1D) nanostrutures, such as nanorods (NRs) and nanowires (NWs), present improved photocatalytic performance [87-89], and could be well alligned on most surfaces with no post-treatment of the catalyst. A comparison of various ZnO nanostrutures for photocatalytic applications is presented in Table 1.

Table 1 Comparison of different ZnO nanostructures used in photocatalytic applications (reproduced with permission from [80] © 2012 Hindawi Publishing Corporation)

Nanoparticles		Nanowires		Nanothin film	
Advantages	Disadvantages	Advantages	Disadvantages	Advantages	Disadvantages
Could be suspended in a solution	Particles aggregation in a solution leads to a reduced surface area	Growth could be well aligned on most substrates	Growth conditions are most restricted	Coated on certain substrates	Lower performance because of small surface area
High performance because of larger surface areas	Post-treatment for catalyst removal is required	Offer larger surface area compared to Nanothin film	Lower surface area compared to nanoparticles	Post-treatment for catalyst removal is not required	
	Difficult to recover all the catalyst	Post-treatment for catalyst removal is not required			
		Lower crystallinity and more defects			

As illustrated, ID nanostructures, such as nanowires, nanorods and nanotubes, provide elevated aspect ratio (surface area to volume ratio) in contrast to thin films (two-dimensional nanostructures). Among the one-dimensional nanostructures, zinc oxide NWs has been significantly studied because of their simple fabrication techniques and applications [52-56].

1.3 Synthesis of ZnO Nanowires

There are two primary approaches for the fabrication of ZnO nanomaterials: Gas phase synthesis (GPS) and solution phase synthesis, the section that follows includes a description of each method as well as an overview of the advantages and disadvantages.

1.3.1 Gas Phase Synthesis

Gas phase synthesis (GPS) includes several synthesis processes such as: vapor-liquid-solid (VLS) growth [81][90], chemical vapor deposition (CVD) [82][91], metal organic chemical vapor deposition (MOCVD) [83][92], physical vapor deposition (PVD) [84][93] , molecular beam epitaxy (MBE) [85][94], metal organic vapor epitaxy (MOVPE) and pulsed laser deposition (PLD) [95]. GPS is the most commonly used-approach for the fabrication of 1D nanostructures [87][96]. Generally, the ZnO source material is sublimed with the assistance of elevated temperature (500-1500°C) and low pressure. Under specific conditions, the vapor condenses onto a surface of a solid substrate and produces high-quality nanowires/nanorods, nanobelts, nanobows, nanohelixes/nanorings. Because the growth conditions can be better manipulated, nanowires/rods are predominately produced by using a horizontal tube furnace, an alumina tube, and a gas supply.

Although the vapor-liquid-solid (VLS) process was initially developed by Wagner and Ellis to fabricate microstructures over four decades ago [88][97], recently, it has been modified and broadly employed for the synthesis of 1D nanorods. It is a simpler, less expensive method

and can be employed to grow ZnO on large wafers [89][98]. In a VLS fabrication method, ZnO nanoparticles will nucleate homogeneously once the thermodynamic kinetic and supersaturation conditions are favorable, followed by an orderly growth of the crystalline wires and rods. Wang et al. [99] successfully fabricated precisely ordered zinc oxide nanowire arrays on specific substrates (GaN and $Al_{0.5} Ga_{0.5}N$).

Using the VLS method aligned large scale zinc oxide nanowires have been effectively synthesized on nitrides and on a common contact [100, 101]. Furthermore, Chu et al. [93][102] adopted the VLS method to produce well-aligned ZnO nanowires for enhanced photocatalytic and field properties by optimizing the aspect ratio, temperature (600-950 ^{o}C) and pressure (0.75-3 torr). They also reported a decrease in the growth rate and length of the nanowires at elevated chamber pressures.

Another common fabrication technique used to produce ZnO nanowires is CVD. Protasova et al. [82] reported a novel production technique to grow Palladium doped on the surface of zinc oxide catalysts. The fabricated catalyst was employed in the hydrogenation of acetylene alcohols. The well arranged zinc oxide nanowires were fabricated by CVD technique onto a zinc oxide seed layer by an atomic layer deposition at 553K. This method provides a strict control of the growth of the nanowires at various stages. After numerous reaction cycles, the as prepared ZnO nanowires showed stability and relative same performance at 323K.

MOCVD is a catalyst-free-low-temperature method of fabricating ZnO nanowires. The MOCVD of ZnO, compared to other deposition techniques, presents a number of benefits, including the potential for larger amount of composition, easy shape control and commercial scale fabrication process. In addition, well arranged zinc oxide nanowires can be fabricated without the initial formation of a seed layer. Fabrication of high quality ZnO at low temperature

10

via MOCVD offers great potential for higher performance nanoscale photonic and electronic device applications.

Ashraf et al. [83] investigated the synthesis of well-aligned ZnO nanowire via the MOVCD technique using chelating bidentate ether adducts of dimethylzinc. They showed that the latter prevents initial reaction with oxygen and, under most favorable conditions, leads to the fabrication of well arranged zinc oxide NWs by MOCVD. The nanowires were prepared in the absence of a seed layer on a glass substrate and silicon wafer. In another paper, Zeng et al. [103] used near 100% purity diethylzinc and nitrous oxide (N_2O) to supply zinc and oxygen, respectively, at an optimal working pressure (10^{-5} – 50 torr) and temperature (400-650°C) to fabricate well arranged ZnO NWs.

Physical vapor deposition (PVD), like vapor-solid (VS) processing, involves the sublimation of a source material without the use of a catalyst [96]. Typically, the PVD technique is a combination of thermal evaporation, oxidation (Zn powder) and deposition of ZnO nanowires on a substrate. Tigli and Juhala [104] reported the growth of high quality ZnO NWs by subliming Zn powder at elevated temperature and deposition of the vapor on the silicon substrate at about $500^{o}C$ in a relatively lower temperature chamber. Zhang et al. [105] fabricated numerous high quality ZnO NWs using the PVD method. In another fabrication via PVD, they obtained well arranged superior ZnO nanowires on Si substrates with high aspect ratio and uniform diameter (100 nm). The ZnO nanowires were synthesized in a reactor chamber, with Zn powder as the Zn^{+2} source, at a rapidly elevated temperature (500°C) under the stream of a N_2 gas flowing at 50 cm^3/min for 60 minutes.

11

1.3.2 Solution Phase Synthesis

Typically, the fabrication technique in a solution phase process is carried out in an aqueous solution, such as an organic solution, at a relatively low temperature ($<200^{o}$C). Currently, the solution phase synthesis technique has emerged as one of the most important methods due to its numerous advantages, such as low production cost, scalability and reduced temperature.

Hydrothermal synthesis provides another commonly used methodology for generating ZnO NWs or NRs [106, 107]."Growth occurs at a relatively low temperature, compatible with flexible organic substrates; there is no need for the use of metal catalysts, and thus it can be integrated with well-developed silicon technologies" [108]; and, also there a number of variables that can be effectively controlled to provide the desired morphologies and properties of the prepared catalyst. Hydrothermal synthesis is superior to other solution phase techniques due to the many point defects of ZnO NWs mainly because of oxygen vacancies [42]. Baruah and Dutta [109] showed the enhancement of the photocatalytic activities of ZnO NW by intentionally creating defects in the crystal lattice through the hydrothermal method without doping with transition metals. The typical mechanism for well-aligned ZnO NWs fabricated on specific surfaces is as follows:

a. The ZnO nanoparticle forms a seed layer on the surface by sputtering or spin coating. At a lower activation energy, the film induces a homogeneous nucleation and a precisely ordered array of ZnO nanowires; lower energy non-polar planes being more stable [110, 111].

b. A commonly used precursor (growing solution) is prepared that contains an aqueous-mixture of an alkaline reagent, such as NaOH or hexamethylenetetramine (HMT), also known as hexamine, and zinc nitrate (source of Zn^{2+}).

c. The substrate is then positioned upturned such that the seeded plane faced down in the growth solution for certain duration of time and temperature. The resultant product is washed and dried.

Generally, NaOH and KOH are the most frequently used alkali compounds in the preparation of zinc oxide via a solution phase method. Typically, "the solubility of ZnO in an alkali solution increases with the alkali concentration and temperature, and super saturation allows a growth zone to be attained" [112]. Usually, potassium hydroxide is preferred to sodium hydroxide due to the lower possibility of integration of potassium ion, K^+, into the zinc oxide lattice because of its bigger radius ($K_r^+ > Na_r^+$) [113]. In addition, the development of a capping layer by the sodium hydroxide ions prevents the formation of nanocrystals during the fabrication process. The major reactions involved in the formation are shown by the following equations [114, 115]:

$$Zn^{2+} + 2OH^- \rightleftarrows Zn(OH)_2 \qquad (1)$$

$$Zn(OH)_2 + 2OH^- \rightleftarrows [Zn(OH)_4]^{2-} \qquad (2)$$

$$[Zn(OH)_4]^{2-} \rightleftarrows ZnO_2^{2-} + 2H_2O \qquad (3)$$

$$ZnO_2^{2-} + H_2O \rightleftarrows ZnO + 2OH^- \qquad (4)$$

$$ZnO + OH^- \rightleftarrows ZnOOH^- \qquad (5)$$

$$HMTA + 6H_2O \rightleftarrows 4NH_3 + 6HCHO \qquad (6)$$

$$NH_3 + H_2O \rightleftarrows NH^{4+} + OH^- \tag{7}$$

$$Zn^{2+} + 4NH_3 \rightleftarrows [Zn(NH_3)_4]^{2+} \tag{8}$$

$$Zn^{2+} + 2OH^- \rightleftarrows Zn(OH)_2 \tag{9}$$

$$Zn(OH)_2 \rightleftarrows ZnO + H_2O \tag{10}$$
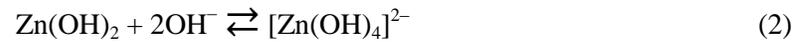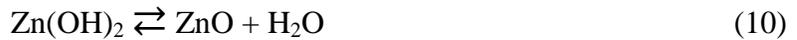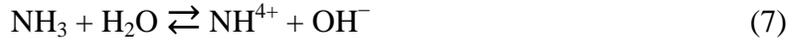
Table 2 Comparison of ZnO NWs growth mediated by alkaline or HTM solutions [122-126]

ZnO NWs growth mediated by alkaline solution	ZnO NWs growth mediated by HTM aqueous solution
Commonly used alkali compounds: KOH and NaOH.	
O^{2-} ions in ZnO comes from the base not from the solvent (H_2O)	H_2O molecules provides the O^{2-} ions
Growth does not necessary require solvent to be water could be organic solvents e.g methanol, ethanol or even ionic liquids	HMT hydrolyze in water (main solvent) and produces HCHO and NH_3
Polarity and saturated vapor pressure of the solvents control ZnO NWs morphology	Growth time and temperature control the ZnO NWs morphology.
Aspect ratio (AP) of ZnO NWs is directed by the relative growth rate of polar and nonpolar surfaces; AP increases on going from more polar solvent methanol to less polar solvent 1-butanol.	Aspect ratio of ZnO NWs is dictated by the growth time and temperature.
Under alkali conditions, the reactions could take place at room temperature by adjusting the ratio of Zn^{2+} and OH	There's an increase in entropy during reaction, so increasing the reaction temperature will push the equilibrium forward.

In equation (2), the product could be in the form of $ZnOH^+$, $Zn(OH)_2$ or $Zn(OH)_3^-$, depending on certain parameters such as the pH value and the concentration of Zn^{2+}. When hexamethylenetetramine $(CH_2)_6N_4$ or HTM and Zn $(NO_3)_2$ are chosen as precursors, the main reactions involved in the growth are illustrated by the following equations [116-118]. Equations (1) to (5) summarize the reaction process, however, in reality; the process is more complicated than what has been expressed above. For example, O_2 plays a important function in the formation

of the final crystal quality of the ZnO NW. Tang et al. [119] reported that high quality ZnO NW

was grown with sharp top surfaces when H_2O_2, which decomposes into H_2O and O_2, was added

to the growth solution. Conversely, other researchers have suggested the formation of very

ragged surfaces if the solution (synthesized with steam distilled water) is used in the process to

eliminate the dissolved O_2. Preparation of ZnO nanowires using $Zn(NO_3)_2$ and HMT as

precursors, is most commonly used in the hydrothermal method [120, 121]. Table 2 compares

the ZnO NW mediated by an alkaline and HTM aqueous solution, the latter providing the Zn^{2+}

ions required for the formation of ZnO nanowires. The H_2O molecules provide O^{2-} ions in the

system unlike the alkali-mediated process. There are many advantages of the ZnO NWs growth

mediated by HTM as shown in the Table 2.

1.3.3 ZnO Seeding Layer on Substrates

Besides cost effectiveness and scalability, the major benefit of wet chemical methods is

that zinc oxide seeds can be used in the formation of thin films or nanoparticles. ZnO NWs can

be developed on numerous substrates including silicon wafers (smooth [112], pillar array [127],

dimethicone E900 [128], thermoplastic polyurethanes (TPU) [129], paper [121], fibers [130-132]

and carbon fibers [133]. The bond of the nucleation layer (seedling layer) to the substrate is

important to improve the quality of the NWs vertically grown alignment. Kang et al. [134]

reported the dependence of NWs on the Si substrate orientation. Qin et al. [137] suggested that

the "adhesion of the seed layer to the substrate can be improved by depositing an intermediate

metal layer, such as Cr or Ti, on inorganic substrates , and by introducing an interfacial bonding

layer, such as tetraethoxysilane molecules, on a polymer substrate". Green et al. [135] examined

the influence of calcination on the growth of the seed layer and formation of well-aligned ZnO

NWs. They reported that the optimal temperature ranges for seed alignment and seed

crystallinity were 100 to 350°C and 150 to 200°C, respectively. At a temperature of 350°C, images revealed a uniform film of ZnO nanoparticles, while for T > 450°C, more nanoparticles were crystallized [136]. Because of the rapid oxidation of zinc film in air or in aqueous solution, it can be employed as a potential seedling layer [137]. Fang et al. [138] effectively fabricated uniform, well arranged, and ultrathin zinc oxide nanowires on a zinc material by the hydrothermal treatment of a zinc foil in a mixture containing water, alcohol and ammonia, at lower temperature in the absence of a catalyst. They demonstrated that the thickness of the zinc oxide seed layer affects the morphology of the zinc oxide nanowires preparation.

Gbayour et al. [139] investigated the effect of the ZnO film thickness on the morphology of the ZnO nanorods, and concluded that the aspect ratio and the density decreased as the film thickness increased.. In another experiment, an increment in seed layer thickness resulted in an increase in diameter (50 to 130 nm) and decrease in nanorods (wire) density (110 to 60 μm^{-2}) [140]. Liu et al. [141] established that, when the thickness of the nucleation layer (seed layer) was increased from 1.5 nm to 3.5 nm by sputtering, the concentration of the ZnO arrays changed from 6.8×10^4 to 2.6×10^{10} nanowires/cm^2. The effect of epitaxial growth of ZnO films with different thickness, 40-120 nm, on the preparation of ZnO nanorods was investigated by Solis-Pomar et al. [142]. The result revealed that nanorods with ~34.5 nm diameter were obtained from 40-nm films, and ~51.5 diameter from 120-nm film. When the seed layer thickness was beyond the range 6.8×10^4 to 2.6×10^{10} nanowires/cm^2, the nanowire density was less sensitive. No formation of ZnO NWs can be achieved if the seedling layer thickness is extremely low, due to the effect of the surface area and the partial molar free energy of the multi-crystalline layers. Generally, the heteronucleation is favored over homogeneous nucleation due to the higher activation energy barrier associated with the latter. To facilitate the nucleation and growth of

16

well aligned nanowires, the substrate and crystal must have an interfacial energy which is lesser than the energy between solution and crystals.

Again, in some cases, in the absence of zinc oxide seed layer, nanowires could still be fabricated on a substrate. Tian et al. [143] developed a "simple seedless method for growing vertical, ultradense and ultra long ZnO nanowire arrays on Au/glass and Au/Si substrates. By adding an adequate amount of ammonium hydroxide to the nutrient solution, the density and the growth rate of ZnO nanowires significantly increased. ZnO nanowires of more than 22 μm long could be readily obtained within 24 h without refreshing the nutrient solution".

1.4 Doping of Zinc Oxide Nanowires

A number of groups have reported on doping as the primary technique of modifying semiconductors characteristic such as electrical conductivity. Several metals including Co [144] , Ga [145], Eu [146], Al [147] , Cu [148], and Ni [149], and non-metals such as: C [150], N [151], P [152], and Cl [153] have been effectively integrated inside the crystalline lattice of zinc oxide nanowires.

Zhou et al. [154], for example, "produced wool-like films of ~65 nm diameter ZnO nanowires doped with 1-5 % of Cu by using intermixed CuI- ZnI_2 powders as the growth precursors". The data from XRD, TEM, and high-resolution TEM microscopy propose that the nanowires are monocrystals, with the fast-growth path equivalent with vertical orientation (101). They" also show that other precursors, particularly high purity powders of Cu, Zn, and graphite mixed in the proportion of Zn:Cu:C=3:1:1 can be also used to produce crystalline Cu:ZnO nanowires. In this case, the growth of the nanowires was achieved at ~800 ^{0}C in an Argon atmosphere with an Argon flow rate maintained at 0.12 L/min".

Li et al. [155] doped ZnO NWs with Cr, Co and Mn using an aqueous solution of zinc

nitrate, HTM and hydrated nitrates of the dopants (Cr, Co and Mn). Gu et al. [156] fabricated

heterogeneous Ag/ ZnO NWs via a facile 2-stage chemical technique in a commercial scale. The

heterogeneous catalyst consisted of extremely dense well arranged (0001) zinc oxide nanowires

as branches and numerous individual crystals of silver nanorods as trunks. After zinc oxide

nanowires (diameter 60-400 nm) were fabricated on the 6 sided-surfaces of the silver doped

nanorods. Das et al. [154] used a hydrothermal by sputtering method to fabricate co-doped ZnO

nanowires. The latter was heated in a NH_3-saturated reactor chamber at $500^{\circ}C$ for 30 min. Wang

et al. [157] "demonstrated the deposition of large-scale ZnO–CdTe core–shell nanowire arrays

on indium-tin-oxide (ITO) substrates through a electrodeposition method (pH 8.3), which was

compatible with the ZnO nanowires".

1.5 Properties

Scanning electron microscopy and X-ray diffraction methods have been employed to

characterize ZnO NW array structures. Figure 3 illustrates the SEM image of the as-prepared

ZnO NWs with a diameter < 100nm. As observed, well-aligned ZnO NWs with hexagonal tips

were produced and position perpendicular to the substrate surface. Figure 4 shows the XRD

pattern of ZnO nanowire arrays and thin films. Although there are some extra peaks in Spectrum

b to Spectrum a, the predominant peak from the (002) atomic plane shows that the ZnO nanowire

structures were fabricated with a c-axis orientation normal to the material surface, data from

SEM and XD revealed the hexagonal crystal structure of ZnO nanowires.

Transmission electron microscopy (TEM) was employed to describe the fabricated ZnO

NWs and to examine the effect of elevated temperature on its structure. Figure 5a depicts a TEM

data which illustrates the crystallinity of the nanowires with average diameter of about 150-200

18

nm. The data also show a significant consistency in the aspect ratio in the density of the nanowires [158]. HRTEM and SAED data in Fig. 5b show the high-purity of the fabricated nanowires. It established that a well arranged vertical zinc oxide NWs are produced due to the lowest surface energy between the crystal and the solution [159]. "The (0 0 2) texture of the zinc oxide NW must form in an effective equilibrium state where enough surface mobility is given to impinging atoms under a certain deposition condition" [160].

Raman measurements were used to explore the sample features and purity, so as to comprehend the phonon-electron interaction of the material [161]. In Figure 6, dominant peaks $(100 – 438 \text{ cm}^{-1})$, represented by the E2 optical mode were observed, which are usually identified in the wurtzite structure of zinc oxide. A more careful study of the E2 on the elevated mode of prepared samples shows that the crystalline superiority of the zinc oxide thin films was enhanced with increased temperature. For instance, well-aligned zinc oxide crystal material was achieved when the Raman spectrum of the ZnO film was prepared at an elevated temperature $(400 \text{ }^{\circ}\text{C})$.

The superior morphology of zinc oxide nanostructures, including the presence of profound native defects can be examined by photoluminescence (PL) [162]. Figure 7a shows a PL spectrum of the fabricated sample consisting of a wide asymmetric near bandgap band with a prominent tail in the area of low energy photons. Similarly, the same observation has been previously reported by using vastly doped zinc oxide samples fabricated by diverse techniques [99]. Typically, a PL band is due to the direct movement of electrons between the CB to the VB tail. Furthermore, the elevated concentration of native defects produces broadening band edges due to induced potential fluctuations [163]. The hydrothermal treatment $(> 400 \text{ }^{\circ}\text{C})$ of the sample produces a truncated PL band and elevates the intensity by multiple folds (Fig. 7b). Heating the

19

sample in air within the temperature range 150–400 ∘C also elevates the PL intensity by three times (Fig. 7c and d) [149]. The broadening of the PL band involved can be accounted for by the broadening of the band edges due to potential fluctuations induced by the high concentration of intrinsic defects or impurities. The width of the band tails, and the dependence of the full width at half-maximum (FWHM) of the PL band on carrier concentration, can be calculated using the model for broadening of impurity bands in heavily doped zinc oxide. The electron density in the prepared sample can be estimated by the correlation of the different treatment temperature of the sample as a function of FWHM in the PL band.
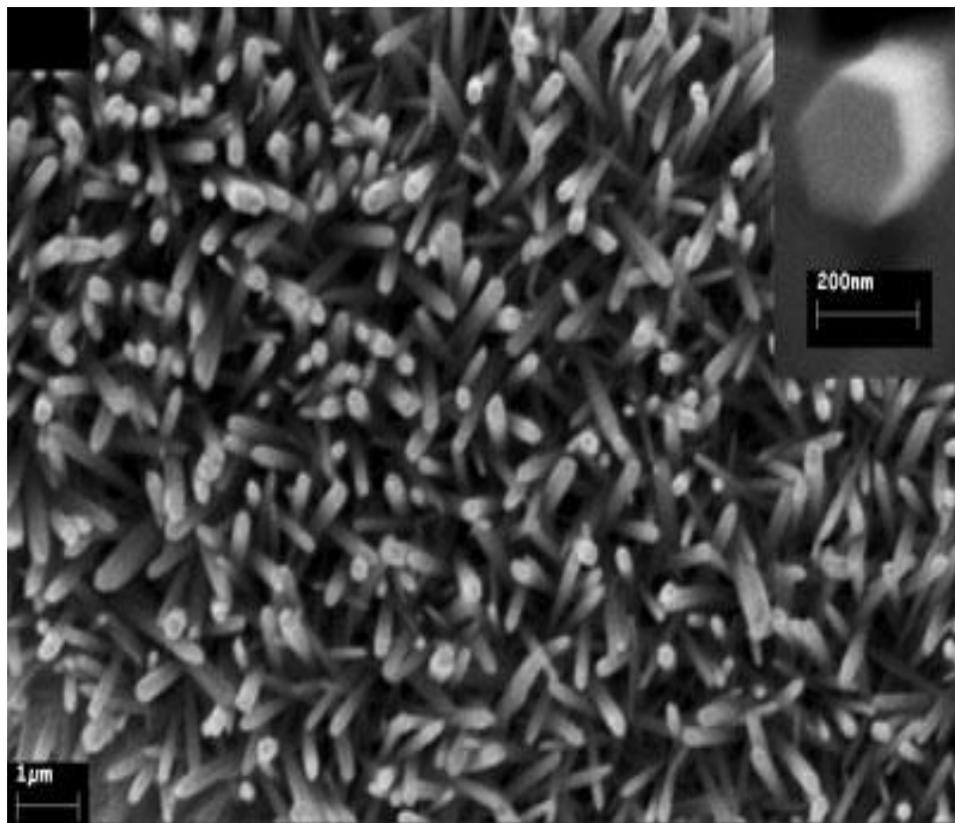
Figure 4 Scanning electron microscopy (FE-SEM) images of ZnO nanorods (reproduced with permission from [164] ©2003, Elsevier)
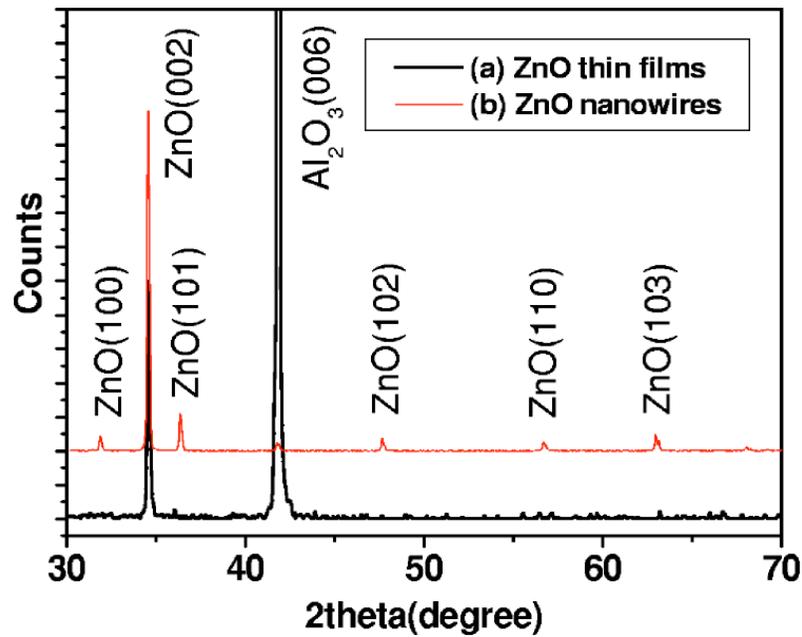
Figure 5 XRD results of ZnO thin films and synthesized ZnO nanowire arrays (reproduced with permission from [64] @ 2005 The American Institute of Physics)
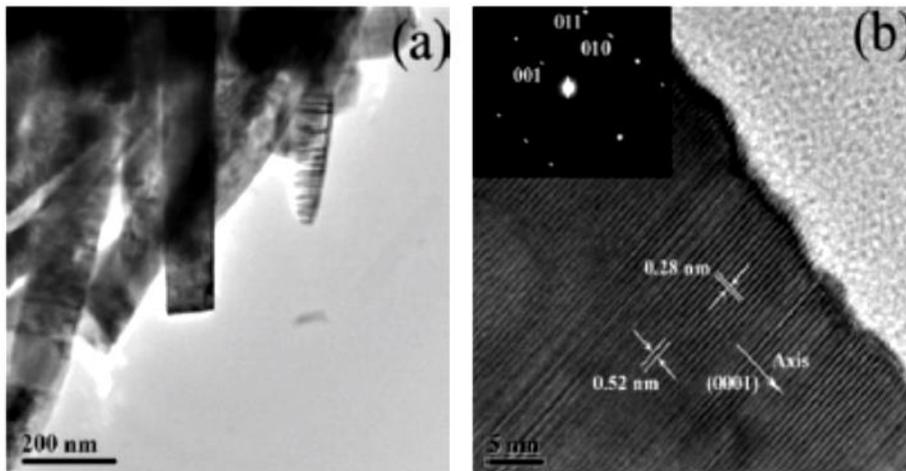
Figure 6 TEM and HRTEM data of ZnO NW. (a) A general view of TEM of ZnO nanowires on an ITO substrate. (b) Individual nanowires with [0 0 2] growth direction shown in HRTEM image. The inset shows selected electron diffraction (SAED) patterns (reproduced with permission from [149] ©2010, Elsevier).
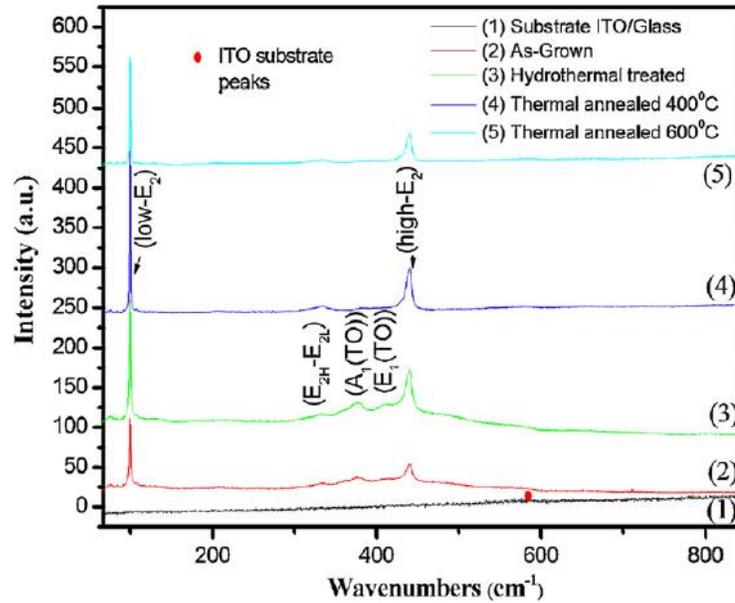
Figure 7 Raman spectra of hydrothermally treated ZnO NW (reproduced with permission from [149] ©2010, Elsevier)
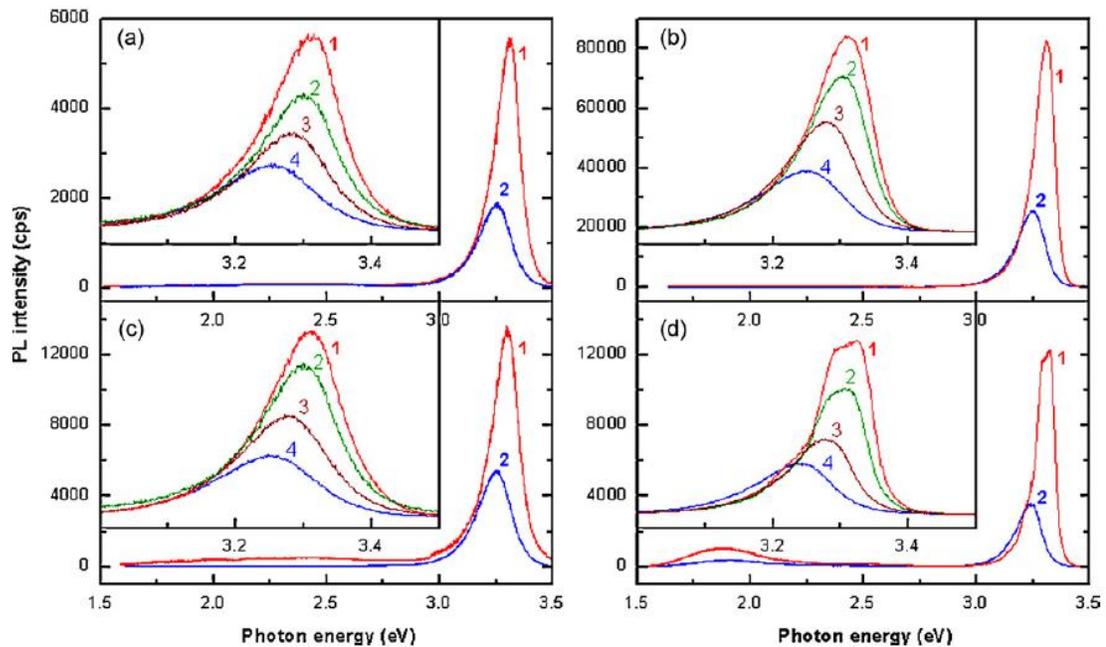
Figure 8 Bandgap photoluminescence (PL) data of doped ZnO NW. (a) Near bandgap PL spectrum of the as-prepared sample with ZnO NWs on an ITO substrate; (b) the sample subjected to the HT treatment; (c) the sample annealed in air at 150 °C (c); and (d) 400 °C. The spectra were measured at T = 10K (curve 1) and T = 300K (curve 2). Inset shows the spectra measured in the near bandgap spectral ranges (reproduced with permission from [149] ©2010, Elsevier).

1.6 Photocatalytic Applications

Photocatalysis is one of the main application areas of zinc oxide NWs where the native surface defect play the most essential role. "The photocatalytic activity of the ZnO NW is expected to be enhanced not only because of its increased surface area and aspect ratio but also because of changes of surface properties such as surface defects and oxygen vacancies" [165]. Sugunan et al. [166] described the incorporation of a synthesized ZnO NW, on a poly-L-lactide nanofiber in a continuous flow system, for photocatalytic water decontamination. Several organic contaminants that have been mineralized under UV irradiation include monocrotophos (MCP, an organophosphate insecticide), N-Phenylbenzenamine (DPA) and methylene blue. The authors also reported good photocatalytic mineralization of multiple organic pollutants, the scalability of the entire photocatalytic water purification system and that it can be used in remote or rural areas.
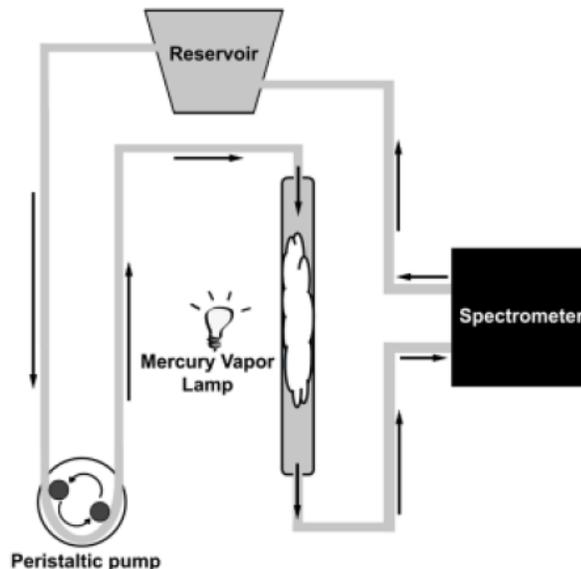
Figure 9 Schematic of a continuous – flow photocatalytic water treatment system (reproduced with permission from [157] © 2010 The American Ceramic Society)

Table 3 shows a selected list of common wastewater dyes /organic contaminates

degraded using one-dimensional (1D) ZnO nanostructures. Liu et al. [158][167] demonstrated

the preparation of ZnO nanofibers from a solution using *N,N*-dimethylmethanamide

(DMF)/propanone, cellulose acetate (CA) and zinc acetate (ZnAc), are employed as a solvent, a

fiber template and a precursor, respectively. They reported that "from the solution system, ZnO

nanoparticles smaller than 40 nm in diameter are obtained by the direct calcination of ZnAc/CA

composite nanofibers, whereas ZnO fibers with radii down to about 12 nm are synthesized by the

calcination of Zn (OH) $_2$ cellulose composite nanofibers, which is obtained from the hydrolysis

of ZnAc/CA composite nanofibers in a base solution" [158]. The photocatalytic performance of

zinc oxide nanorods was assessed and evaluated with that of zinc oxide particles by measuring

the photodegradation of dyes, including Rhodamine and Amido black 10B. ZnO nanofibers with

a diameter of 23 nm, under visible light irradiation for 1 hr, demonstrated higher photocatalytic

efficiency (30%) than ZnO nanoparticles (14%) in degrading some RhB. Additionally, Li et al.

[158] reported the" porphyrin heteroaggregate modified ZnO microrods, prepared by simply

mixing ZnO microrods with the TAPPI-CoTPPS porphyrin heteroaggregate". The enhanced

photocatalysts demonstrate a vital bond involving the zinc oxide and porphyrin heteroaggregate,

which is essential to channel electron from porphyrin to the CB of the zinc oxide nanostructure.

They reported that ZnO/TAPPI-CoTPPS is a very effective photocatalyst for the

photodecomposition of RhB (16%/h) in aqueous solution under visible light irradiation. This

could be extended to water purification in a wastewater treatment sector.

In another decontamination study, using ZnO NWs, Zhao et al. [150] fabricated

homogeneous silver coated ZnO NW arrays. Dried zinc oxide arrays were immersed into an

aqueous solution of $AgNO_3$, and subsequently placed in growth solution to initiate the deposition

of Ag film. The decomposition of RhG dye molecules by NaBH4 was studied in the absence and presence of the fabricated Ag-coated zinc oxide NW arrays. Evidently, without the photocatalyst, R6G was photodecomposed by ~70%/hr. While 80% photodecomposition of R6G was achieved using zinc oxide NWs and Ag-coated zinc oxide NWs at about 0.5 h and 0.25 h, respectively.

Baruah et al. [151] fabricated ZnO nanorods via a simple hydrothermal technique. Zinc oxide nanorods were tightly attached to cellulose fibers and the fabricated materials were used multiple times during the experiment. Photodecomposition of about 93% and 35% were achieved for methyl blue and methyl orange, respectively, under the irradiation of white light at $963W/m^2$ for 2 hrs in the presence fabricated photocatalyst (zinc oxide NRs).

Gu et al. [147] investigated the fabrication and photodegradation performance of dendrite–like ZnO/Ag nanostructures. Dendrite-like ZnO/Ag nanocrystals were prepared by a facile solution base technique. They reported that "crystalline Ag nanowires were first synthesized by the polyol process, then highly dense ZnO nanorods with diameters of about 50 - 400 nm were vertically grown on the lateral surface of the Ag nanowires, by a simple aqueous solution route, with a uniform growth along the (0001) direction" [147]. Afterward very thin zinc oxide nanowires with a radii < 15 nm were synthesized on top of the ZnO nanorods. The ZnO/Ag NRs exhibited a superior photocatalytic performance when compared to undoped ZnO nanorods, and the ZnO/Ag with ~ 8% Ag revealed the highest photocatalytic activity. In a similar decontamination of MB, zinc nanowires, grown by the hydrothermal method, were found to be more effective (12-24%) compared to nanofilms due to numerous point defects from the oxygen vacancies. In the same work, Baruah et al. [78] reported a 7% increase in photocatalytic activity, under visible irradiation after 3hr, using a hydrothermal method compared to other conventional techniques.

Guo et al. [160] prepared "ZnO and TiO$_2$ 1D nanostructures (nanorods and nanotubes) by low-cost, low-temperature, solution-based methods and their properties and photocatalytic performance were studied, after 90 min, it was reported that faster MO degradation under simulated solar illumination was observed for ZnO NRs (51%) , while under UV illumination faster degradation was observed for TiO$_2$ (57%)". The absorption spectra and the surface defect on the zinc oxide nanowires accounted for the huge variation in photocatalytic performance when compared to titanium under different light irradiation in UV and visible range.

Sun et al [161] prepared a well –arranged monocrystal zinc oxide nanobelt arrays on a silicon wafer by a carbothermal reduction route with the assistance of a SnO$_2$/Sn species. The as-prepared ZnO nanobelts decomposed > 94% of MO in a solution after 5h of UV irradiation.

Hamedani et al. [162] successfully prepared zinc oxide nanorods via a hydrothermal technique. Congo red was employed to study the catalyst performance for the photodegradation of contaminants. For example, under UV light irradiation (30W), the photodegradation of Congo red was reported to be 90% in about 2.5 h.

Mohan et al [163] investigated the photodegradation performance of zinc oxide NWs with different diameters within 30-300 nm, under UV light irradiation (80 W/cm^2), for the decomposition of Resazurin dye (RZ) in the aqueous solution. The zinc oxide nanorods were fabricated by a mixture of carbon powder and zinc oxide particles in a horizontal tube furnace via a vapor pressure technique. The addition of the carbon powder considerably reduced the decomposition temperature of the catalyst. The mixture was placed in a 100 cm long quartz tube, bubbled with high purity argon stream from one side with the other end of the quartz joined to a water bubbler. At 900°C, oxygen gas flowing at 25 sccm was introduced for 0.5 h, and then allow to cool to room temperature. The nanowires were collected 60 cm away from the source.

The degradation efficiency of RZ for 30 nm and 300 nm nanowires were 75% and 18%, respectively, under a 40 min UV exposure time. It was revealed that the 30 nm diameter ZnO NW showed the highest photocatalytic activity. The results also revealed that as the intensity of the RZ peak ($\lambda = 604$ nm) decreased, concurrently, a new peak (575 nm) was observed which correspondents to the formation of Resarufin (RF). Hence, the photocatalytic reaction involves 2 steps: photo reduction (RZ into RF) and photo degradation (RZ and RF).

Furthermore, ZnO nanofibers were used to remediate dye molecules such as acid fuchsin and amido black 10B. Zinc oxide nanofibers were fabricated via electrospinning a precursor solution of zinc acetate (ZnAc)/cellulose acetate (CA) mixed in the solvent *N, N*-dimethylmethanamide (DMF)/acetone. After photocatalytic activity for 0.5 h, under UV irradiation, 95% of the acid fuchsin was decomposed and decolorized. In the same time interval, 85% of the amido black 10B was degraded, with the color changing from dark to light blue. It was also reported that in 0.3 h the decomposition efficiency of acid fuchsin was 73% and 85% by zinc oxide nanoparticles and nanofibers, respectively, signifying that the photocatalytic performance of the ZnO nanofibers was superior to zinc oxide nanoparticles.

Although a well – arranged less than 10-nm monocrystal zinc oxide nanobelt arrays were obtained by Sun et al [161] prepared on a silicon wafer via a carbothermal reduction route, little has been documented on the fabrication of well-aligned zinc oxide nanowires with radii of less than 20 nm. Therefore, one of the fabrication challenges of nanowire materials is to reduce the nanowire diameter and, at the same time, align the nanowires in a controlled fashion. The solution to this challenge is proposed in this work.
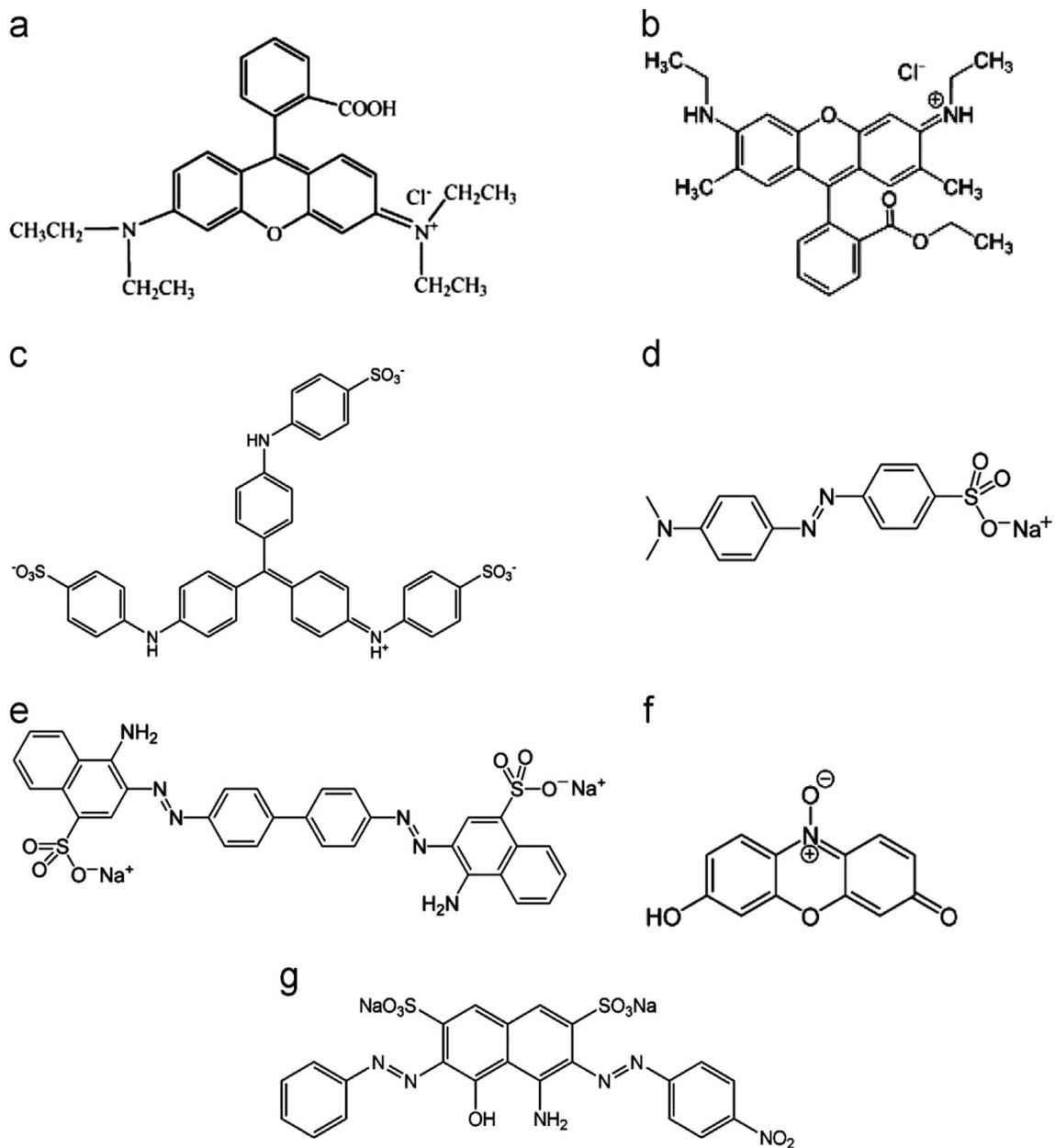
Figure 10 Structures of selected dyes. (a) Rhodamine B(RhB), (b) Rhodamine 6G (Rh6G), (c) Methyl blue (MB), (d) Methyl orange (MO), (e) Congo red (CR), (f) Resazurin (RZ) and (g) Amido black (AB)

Table 3 Selected list of common wastewater dyes /organic matter degraded using one-dimensional (1D) ZnO nanostructures [87], [159, 160], [167-172]

Compound	Formula	Photocatalyst	Light source	% Degradation (Duration)	ef.
RhB	$C_{28}H_{31}ClN_2O_3$	ZnO/ TAPPI-CoTPPS	Visible $\lambda \geq 420nm$	98 (1hr)	58
		ZnO nanofibrous mats	Visle (500w)	60 (2hr)	59
RhB 6G	$C_{28}H_{31}N_2O_3Cl$	Silver-coated ZnONW	UV	80 (14 min)	50
		photocatalytic paper with ZnO nanorods	visible (963w/m^2)	>95 (2 hr)	51
Methyl blue	$C_{16}H_{18}N_3SCl$	ZnO NR/Ag 8% atom		>75(5.5 hr)	60
		ZnO nanorods	visible	98 (3hr)	8
		photocatalytic paper with ZnO nanorods	white light (963w/m^2)	>35 (2hr)	51
Methyl Orange	$C_{14}H_{14}N_3NaO_3S$	ZnO NRs	UV	51 (90 min)	60
		ZnO nanobelts	UV	94 (5hr)	61
Congo Red	$C_{32}H_{22}N_6Na_2O_6S_2$	ZnO nanorods	UV (30W)	90 (160 min)	62
Resazurin	$C_{12}H_7NO_4$	ZnO NW	UV (80/cm^2)	75 (40 min)	63
Amido black 10B	$C_{22}H_{14}N_6Na_2O_9S_2$	ZnO nanofiber (23nm)	Visible (500W)	85 (30 min)	58

ZnO/ TAPPI-CoTPPS = ZnO microrods and nanoheteroaggregates containing tetrakis (4-trimethylaminophenyl) porphyrin (TAPPI) and tetrakis (4-sulfonatophenyl) porphyrin cobalt (II) COTPPS)

1.7 Conclusions

Although titanium has been thoroughly investigated as an effective photocatalyst, zinc oxide has been considered an appropriate substitute since it is less expensive and possesses a similar band gap (~ 3.3eV). Compared to TiO$_2$, ZnO has been reported to produce better degradation due to the higher efficiency of photoexcitation under visible light for

decontamination of water. Furthermore, ZnO is considered a better candidate than TiO_2 due to its higher activity because of the larger number of surface defects, oxygen vacancies and the facile preparation of well-aligned crystalline nanowires, all of which significantly enhance the photocatalysis process. To further improve the photoactivity, there is a need to increase the photocatalyst surface area, for optimal mass transfer and efficient dye degradation, without additional equipment cost in catalyst separation from water. To this end, one-dimensional (1D) ZnO nanostructures such as rods, wires, and tubes provide improved photocatalytic performance due to their higher aspect ratio (interactive surface). This paper highlighted the fabrication, properties and water treatment applications of 1D ZnO nanostructures; many methods can be employed in the preparation of ZnO NW-based photocatalysts. Nevertheless, the hydrothermal technique is widely used because the method is simple, scalable, and efficient. In addition, it facilitates the fabrication of quality nanoscale crystalline ZnO-based photocatalysts. Evidently, ZnO has proven to be a potent tool for water purification, via photocatalysis, as well as other environmental applications, this obviously provides the motivation for advances in the fabrication of high quality ZnO nanowires (nanorods).

CHAPTER 2: TiO$_2$ PHOTOCATALYST FOR GREEN SPACE EXPLORATION

2.1 Introduction

Work is underway at NASA Glenn Research Center (GRC) and numerous other research laboratories to develop technologies based upon heterogeneous photocatalysis to decompose organics and/or decontaminate wastewaters [1-3, 41, 44, 173, 174]. The presence of these contaminants in water could pose potential health and environmental problems in a controlled environment such as on a space station or during long-term manned missions. There are also significant terrestrial concerns about chemicals, such as azo dyes and pesticides that are discharged to the environment; many of these are toxic, carcinogenic, mutagenic, and/or resistant to biodegradation [4, 7, 175-178] Additionally, conventional wastewater treatment techniques are usually ineffective in the decontamination of these compounds. Thus the development of energy efficient and "green" technologies to reduce or eliminate organic wastes has important potential dual-use applications.

To this end, semiconductors like titanium oxide (TiO$_2$), zinc oxide (ZnO) and other transition metal compounds (mostly oxides) are being studied for their photocatalytic properties to decompose a number of contaminates and organic compounds into harmless inorganic such as CO$_2$ and H$_2$O [41, 44]. The basic principles concerning these catalysts are well understood; when a light source of sufficient energy illuminates a photocatalyst, electron/hole (e$^-$/h$^+$) pairs will be formed as electrons absorb the energy from the irradiated photon, the electron tunnel from the VB to the CB, leaving the positive charged holes in the VB (see fig 3). Hence, the produced pair initiates series of photochemical reactions that lead to the decomposition of contaminates

31

adsorbed on the surface of the catalyst in aqueous solution. Transition metals serve as co-catalysts by trapping free electrons and prevent the electron/hole pair-recombination process resulting in higher photocatalytic performance. Titanium (TiO_2) is the most commonly used photocatalyst due to its excellent optical properties and ability to facilitate very rapid light-induced reactions. TiO_2 exists in three phases: rutile and anatase (most commonly) and brookite. Compared to most catalysts, titanium dioxide is quite inexpensive, chemically very stable, and readily available.

In this study, Rhodamine B (RhB) an organic dye (see Figure 11), a model compound for organic waste, was decomposed by TiO_2 photocatalysts with various transition metals added as co-catalysts by traditional catalyst processing methods, and were characterized by Brunauer, Emmett and Teller analysis (BET), X-ray diffraction (XRD) and scanning electron microscopy (SEM).
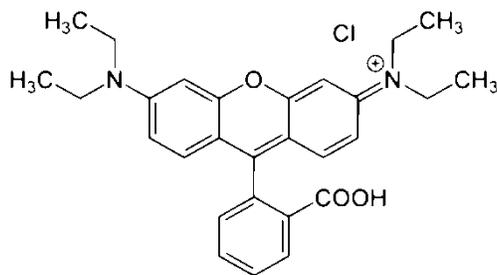
Figure 11 Molecular structure of rhodamine B

This research intends to probe TiO_2 photocatalytic activity by enhancing its efficacy with different transition metal co-catalysts such as: copper (Cu), palladium (Pd), platinum (Pt), silver (Ag), gold (Au). and ruthenium (Ru). To achieve this purpose, different metal-co-catalyst-titanium photocatalysts were synthesized on either anatase or a 4:1 mixture of anatase and rutile

(P25), one of the better reference photocatalysts. All photocatalysts were tested in a broadband photoreactor to determine their effectiveness in dye degradation.

RhB is a common dye often used as a tracer in water to study flow rate and direction (Figure 11). It is reddish violet, highly soluble in water, and dangerous if swallowed. The maximum absorbance (λ_{max}) of RhB is around 550-555 nm [179] The color of this family of dyes results from conjugated chains or rings that absorb light at visible wavelength [176].

2.2 Materials and Methods

All chemicals were of high purity (> 99%) and used as received. To process the promoter-loaded photocatalysts, a Büchi Rotavapor 210 with a Vacuum Pump (V-700) was used, see Fig. 2 below. Experimental and instrumentation details not given below are described in a recent report from the group at NASA Glenn Research Center [180].

The following promoters or co-catalyst precursors were used: tetraamine platinum (II) nitrate ($Pt(NH_3)_4(NO_3)_2$), ruthenium (III) nitrosyl nitrate ($RuNO(NO_3)_3$), palladium (II) chloride ($PdCl_2$), and sodium tetrachloroaurate (III) dihydrate 99.99% ($NaAuCl_4 \cdot 2H_2O$); all were packaged under argon and obtained from Alfa Aesar of Ward Hill, MA. Silver nitrate ($Ag(NO_3)_3$) and RhB (packaged under argon) were obtained from Acros Organics, Morris Plains, NJ and cupric nitrate ($Cu(NO_3)_2$) was obtained from Fisher Scientific of Pittsburgh, PA. A 8.0 x 10^{-6} M RhB solution was prepared from a stock solution containing 0.447 g of RhB dissolved into 100 ml of deionized water. The stock and the diluted solutions had very dark reddish-purple and pink colors, respectively.

2.3 Preparation of Transition Metal-Promoted TiO$_2$ Photocatalysts

Either 1% or 5% of the metal complex was dissolved in 20 ml of water. The only exception was the catalyst using 1% Pd. In the latter case, a few drops of HCl were added to the solution and stirred overnight to completely dissolve the palladium complex (H$_2$PdCl$_4$). The solution (metal complex + water) was added dropwise to 10 g of TiO$_2$, either anatase or Degussa P25. Then, it was dried in a rotary evaporator (rotovap) at 200 torr in an 80°C water bath (Fig. 2). Occasionally, the photocatalyst was scraped off the walls with a spatula and the flask was placed back on the rotovap. When the powder was dry, it was stored in an oven until calcinations were performed. Prior to calcining, the photocatalysts were ground with an alumina mortar and pestle. All the catalysts were calcined using a Thermolyne 21100 Tube Furnace at 400°C for 2 hours under a flow of dry air. Calcining removes the volatile substances in the photocatalyst, typically nitrate released as nitric oxide (NO) or chloride released as HCl or Cl$_2$. Air is allowed to flow through the tube at about 5 ml/min to ensure that the catalyst does not decompose. After that, photocatalysts were characterized and screened for decomposition of RhB in a broadband photoreactor (Ace Glass).

2.4 Promoted TiO$_2$ Photocatalytic Studies

Photocatalytic experiments were carried out with 10 mg of catalyst added to 10 ml of an 8.0 x 10^{-6} molar RhB solution in a quartz photoreactor. The solution was irradiated with broadband light in air and nitrogen from pressurized cylinder tanks through a bubbler. The gas flow maintained the suspended photocatalyst in a motion while providing a good stir to the solution. Aliquots from the reactor (1.5 ml) were taken using a Pasteur pipette at pre-determined time intervals for up to one hour and centrifuged. The concentration of RhB was measured by a

Perkin Elmer Lambda 950 UV/Vis spectrophotometer; UV/Vis spectra were recorded to monitor dye decomposition.

Figure 12 (a) Bench scale reactor system (b) Dried and calcinated photocatalysts

2.5 Results and Discussion

Native or metal co-promoted (enhanced) titanium (TiO_2) photocatalyst powders were subsequently characterized by traditional methods and then screened for organic matter decomposition efficacy as discussed below. Exploiting this technology for space missions would entail design, testing and construction of a light-driven system that utilizes photocatalysis, as briefly described in the following section.

2.6 Characterization of Photocatalyst Samples

Analyses of promoted-titanium photocatalysts were performed by X-ray diffraction (XRD), scanning electron microscopy (SEM), BET and energy dispersive spectroscopy (EDS) instruments. The BET analysis (Table 4) determined that the photocatalysts with the largest surface areas were anatase-TiO_2/Ru 1% and anatase-TiO_2/Pt 1%; while that with the smallest surface area was anatase-TiO_2/Ag 5%, although all samples differed by at most 2 m^2/g. The surface area of our native anatase TiO_2 was 10 m^2/g; this is much lower than the surface area of unmodified P25 TiO_2 (~50 m^2/g). It was anticipated that for the lower percent metal containing

samples, the specific surface area would be higher because the metal promoter would not occupy

as many surface sites. EDS analysis confirmed the presence of metal promoters on the surface of

titania photocatalysts. The analysis for the promoter shows a weight percent range of 1.11% -

2.48% for the photocatalysts with a target value of 1% loading. In the case of the desired 5%

promoter loading, the range was 3.78 - 8.68 %. Each catalyst had the same promoter wt%

calculated and added but the EDS analysis showed that samples often either exceeded or were

under their desired loadings as a result of processing variability. A typical XRD powder pattern

is shown in Fig. 3 for a 1% Ru-promoted anatase sample.

Table 4 EDS and BET analysis for metal-doped titanium photocatalysts

Sample	% wt. Ti	% wt. O	% wt. Promoter	% Degradation after 60 min	Surface area (m^2/g)
Anatase TiO_2/Ag 1%	47.00	51.90	1.11(Ag)	66	8.38
Anatase TiO_2/Pd 1%	47.24	51.36	1.40 (Pd)	74	8.75
Anatase TiO_2/Pt 1%	48.74	48.84	2.24 (Pt)	72	9.49
P25 TiO_2/Cu 5%	42.51	48.80	8.68 (Cu)	40	8.35
Anatase TiO_2/Cu 5%	48.10	45.59	6.31(Cu)	28	8.35
Anatase TiO_2/Ag 5%	46.84	49.38	4.94(Ag)	76	7.52
Anatase TiO_2/Ru 1%	51.85	46.20	1.95 (Ru)	85	9.26

NB: The weight percentage of each element in each sample is the average of three EDS runs

Morphological analysis of the photocatalysts was accomplished by SEM (Fig. 4). Photocatalyst

surfaces look rough with small particles that are not evenly distributed. The particles of the

photocatalysts have different shapes and also various sizes (25-100 µm in diameter). XRD

analysis confirmed that the synthesized photocatalysts are polycrystalline (Fig. 3). As shown in Table 4, the % degradation of RhB after 60 min. was in excess of 70% for anatase-TiO_2/Ag 5%; the anatase-TiO_2/Ru 1%, showed the highest efficiency (85%), with the lowest being the P25 TiO_2/Cu 5% (40%). A higher specific surface area typically corresponds to higher catalytic activity as observed for anatase TiO_2/Ru 1% [173] [174].
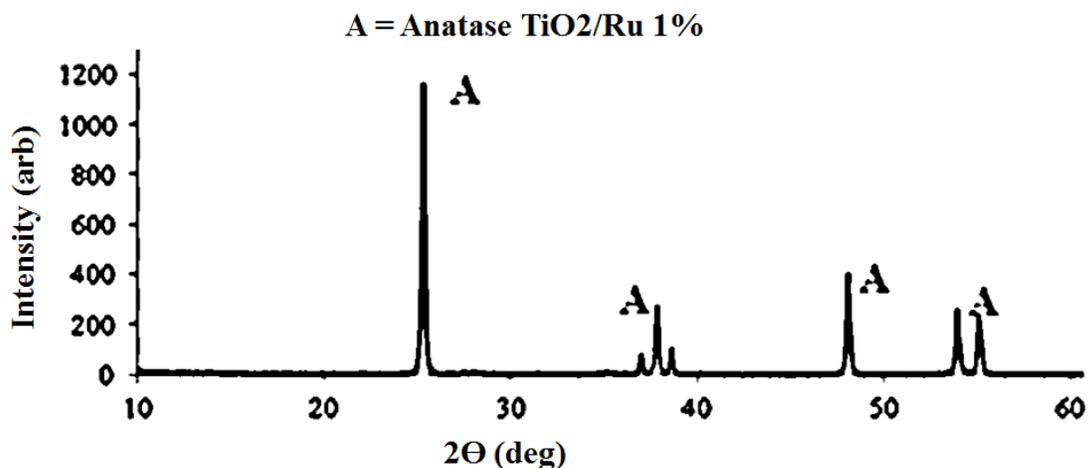
Figure 13 X-ray diffraction powder pattern of the anatase/1% ruthenium sample
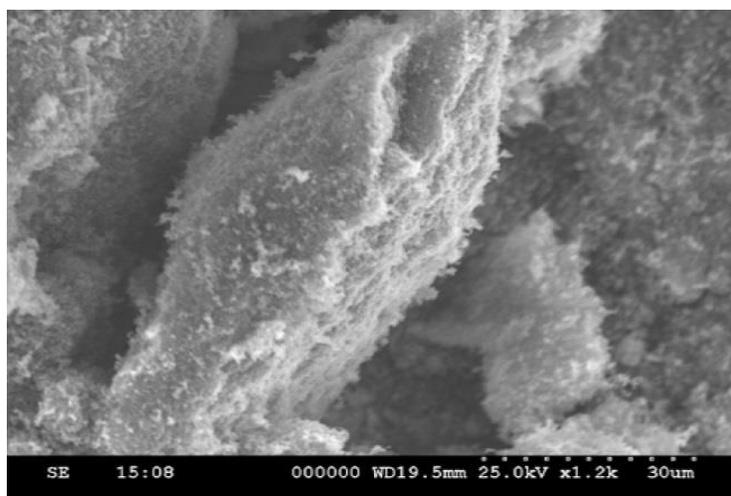
Figure 14 SEM image of anatase TiO_2/Ru 1% photocatalyst

Table 5 X-ray photoelectron spectroscopy data from metal co-promoted TiO$_2$ samples

Metal (Level)	TiO$_2$ Phase(s)	Metal Peak(s)	TiO$_2$ Peaks	Assignment(s)	Reference
Silver (2.0 %)	Anatase	367.6; 373.5	458.1; 464.1	Ag$_2$O (1.5)[a]	[181]
Silver (3.3 %)	Anatase	367.6; 373.6	458.2; 464.1	Ag$_2$O (1.6)[a]	[182]
Copper (5.0 %)	Anatase	932.6; 934.3	458.2; 464.1	Cu$_2$O and CuO[c]	[183]
Copper (3.6 %)	P25[b]	932.4; 934.1	458.2; 464.1	Cu$_2$O[c] and CuO	[183]
Palladium (0.8 %)	Anatase	336.1; 341.3	457.9; 463.7	PdO	[184]
Platinum (1.1 %)	Anatase	70.9 (sh); 71.8; 73.9; 75.4	458.0; 464.2	Pt^0 and PtO[c]	[184]
Ruthenium (~1 %)	Anatase	283; 287[d]	458.2; 464.0	Ru^0 and RuO$_2$[c]	[185]
Ruthenium	P25[b]	281; 285[d]	458.3; 464.2	Ru^{0c} and RuO$_2$	[185]

[a]FWHM = 1.75 eV (AgO); 1.50 eV (Ag$_2$O); 1.15 eV (Ag). [b]P25 = Mixed phase Anatase/Rutile. [c]Majority Phase. [d]Ru XPS peaks obscured by carbon, observed as shoulders.

2.6.1 XPS Studies

The XPS spectrum for Ag gives binding energies for Ag of 367.6 eV (3d$_{5/2}$) and 373.5 eV (3d$_{3/2}$). These values indicate that Ag is present on the TiO$_2$ surface as Ag$_2$O, in the monovalent state. The XPS spectrum of Ti shows two peaks located at 464.1 eV (2p$_{1/2}$) and another one located at 458.1 eV (2p$_{3/2}$). The splitting of ~ 6 eV indicates a normal state of Ti^{4+} in the as-prepared mesoporous anatase TiO$_2$. Data from Cu/TiO$_2$ XPS shows two kinds of copper species on the surface of the sample. Binding energy of 932.1 eV is characteristic for Cu$_2$O, while higher binding energy of 933.68 eV is characteristic for CuO. It is supposed that coexistence of Cu^{2+} and Cu$^+$ can improve the photocatalytic efficiency by fitting results of O 1s and Cu 2p$_{3/2}$ XPS of the catalysts with different dopant concentration. XPS data for Pd/TiO$_2$ reveals the doped catalyst by sol-gel technique depicts a significant (double) impact on the palladium 3d from the electron binding energy of 334–346 eV. By the same method of fabrication, the value of 336.2 eV can be attributed to electron binding energy of palladium (II) oxide (PdO) while the energy of

335.3 eV corresponds to PdxO. In addition, the electron binding values of the oxide of palladium is slightly higher than Pd $3d_{5/2}$ at 337.5eV. Based on the experimental data, it is proposed that the energy of 337.5 eV may have resulted from the diffusion of O_2 atom into the subsurface lattice of the palladium (11) oxide. For the impregnation catalyst, the binding energy of Pd $3d_{5/2}$ at 337.5 eV is slightly lower than that of PdO2. After the reduction reaction, the palladium compounds are converted to metallic Pd which is usually characterized by electron binding energy of 334.7 eV, this will be demonstrated in more detail in future publication.

The chemical state and surface chemistry of platinum was also investigated. Typically, platinum can exist in 3 states: platinum (0), platinum (11) and platinum (IV). Platinum 4f is usually characterized by two major signals within the range of 71.1 eV - 72.3 eV and 72.3 – 75.6 eV which signals corresponds to metallic platinum (0) and oxidized platinum (11), respectively. The oxidation potential of palladium such as from Pd (0) to Pd (11) helps to improve photocalytic performance. The oxidation state of Pt often plays an important role on the enhancement of photocatalytic activity. However, research has reported that Pt (11) shows less photocatalytic activity to Pt (0) in the degradation of 4-chlorophenol and chloroform.

XPS obtained of Ru/TiO_2 catalyst are presented for both anatase and P25 substrates. Ru exist in more reduced state with electron binding energy of ~ 281 eV (Ru(0)) and minor phase RuO_2 on P25, similar to Cu (above). The signal within the range from 279.0 to 283.0 eV is poor due to interference from carbon. These developments can be best clarified by assuming that metallic Ru (denoted as Ru(0) or Ru^0) has occurred due to treatment at elevated temperature, with the higher surface area P25. The contribution of the oxidized RuO_2 (~ 283 eV) is more pronounced on anatase.

Summary of the XPS data are illustrated in table 5. Surface area measurements of all the photo catalysts are shown in Appendix **C**. Topographical images taken by SEM and EDS results, as well as XRD analysis are also illustrated.
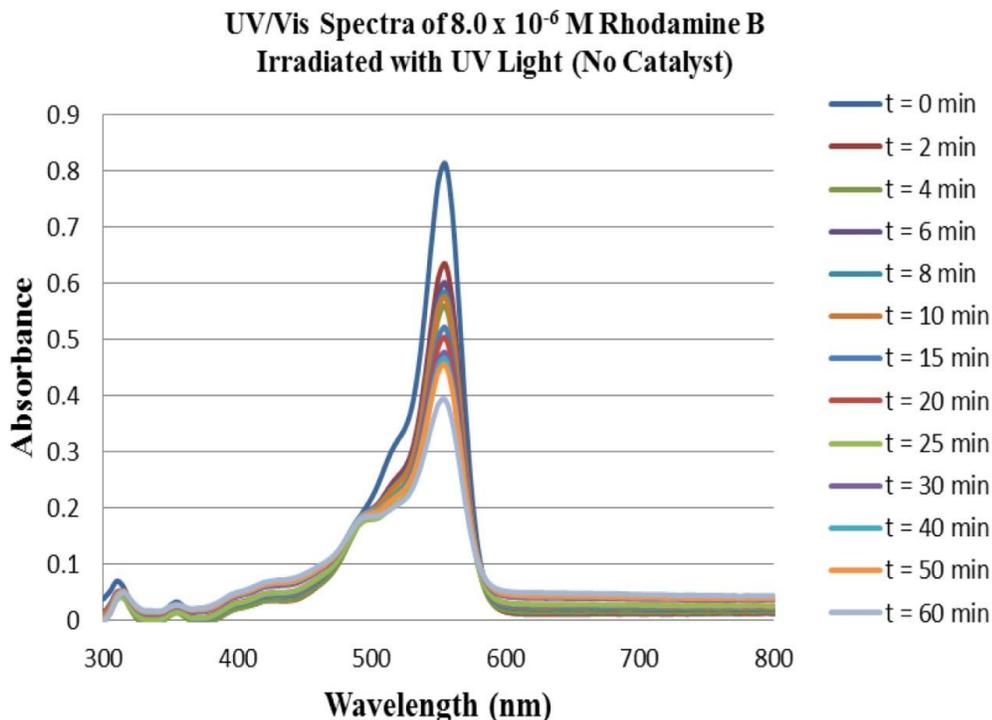
Figure 15 UV-Vis spectra of RhB irradiated without a catalyst for 60 min

2.7 Photocatalytic Results

Figure 15 shows a typical absorbance vs. wavelength relationship for the UV/Vis spectra of 8.0 x 10-6 M RhB irradiated with UV light in the absence of a catalyst. The initial (0 min) and final (60 min) absorbance values were 0.82 and 0.39, respectively. Figure 6 illustrates the degradation of a RhB solution in air, in the absence and the presence of a catalyst, and saturated with nitrogen gas with the catalyst present. The highest and lowest efficiency of degradation of RhB was found in a reaction with anatase-TiO_2/Ru 1% (under aerobic conditions) and anatase-TiO_2/Ru 1% (under nitrogen saturated conditions), respectively. RhB can react even in the

absence of a catalyst under UV light as shown by the red line in Fig. 6, however, the presence of

anatase TiO_2/Ru 1% accelerates this photoreaction significantly.
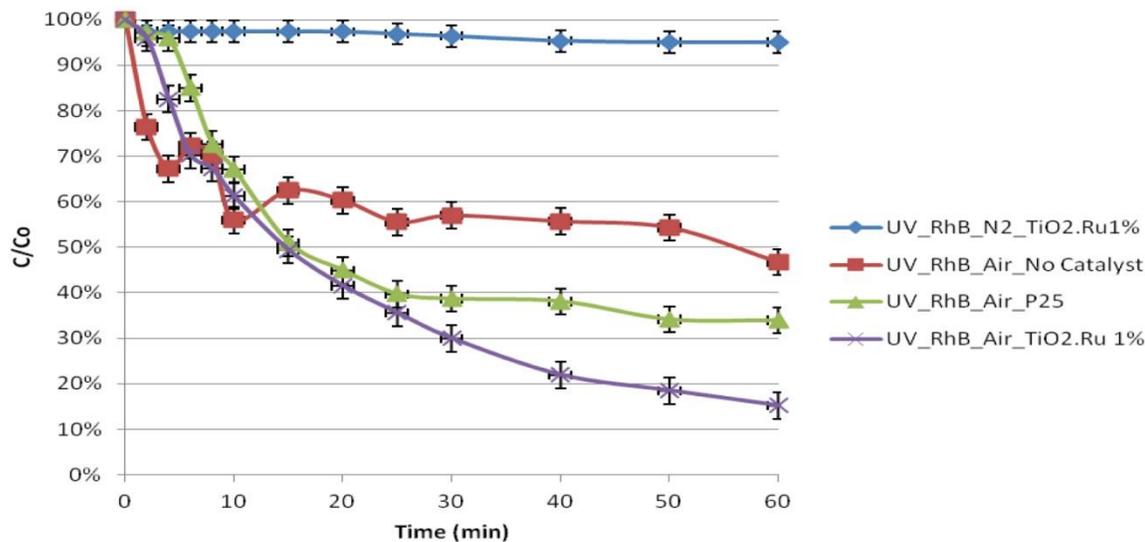
Figure 16 UV-Vis spectra of photocatalytic studies of a metal doped titanium catalyst

2.8 Mechanism of Photocatalysis

There have been a number of investigations to evaluate photocatalytic performance under

both N_2 and O_2 rich environments. Ali et al. [65] investigated photocatalyzed oxidation of methyl

blue using ZnO thin films and suggested that the reaction occurs mostly by a Mars Van Krevlen-

method (i.e. "lattice oxygen atoms are used for oxidation, causing degradation of the ZnO lattice

over time") [65]. This analysis proposes that providing O_2 saturated conditions either minimizes

or inhibits lattice oxygen from participating in the photocatalyzed oxidation reaction, or

replacement of the lattice oxygen atoms are removed during this reaction. It is hypothesized that

oxygen atoms are removed from the photocatalyst lattice and utilized in the radical initiation and

propagation phase of the follow-on reactions type.

Photocorrosion of photocatalysts was reported, as the reaction progresses under O_2 limited conditions, because there is only a partial O_2 supply to replace the lattice oxygen atoms employed [16]. Consequently, under oxygen-rich conditions, the catalyst degradation is reduced because of the regeneration of the lattice oxygen atoms and maintenance of the physical structure. The Mars Van Krevlen-type mechanism has also been reported for TiO_2 and other (doped) ZnO-containing catalysts. For example, Hurum [186] have shown that lattice oxygen atoms are extracted from mixed-phase TiO_2 (Degussa P25) during the photocatalytic decomposition.

In a related study of the photodegradation of RhB, under ultraviolet and visible light irradiation [187]by Lee et al. [188], a new family of $BiO(Cl_xBr_{1-x})$ (x=0, 0.1, 0.2, 0.5,0.7, 1) was synthesized by hydrothermal processing. The Bi-based photoactive material with x = 0.5 exhibited a 74.2% degradation efficiency in 60 min, about 10% less compared to anatase-TiO_2/Ru 1% (Table 5).

Zhong et al. [187] carried out the photocatalytic degradation of RhB using TiO_2 supported on activated carbon (TiO_2-AC) under microwave irradiation. The decomposition of RhB in microwave-enhanced photocatalysis (MPC) 30 mg/L was 96% after 20 min. The reaction rate constant of RhB, a pseudo first-order reaction, using this photocatalyst material was 4.16 times greater than that using Degussa P25.

Houšková et al. [189]" investigated the photocatalytic activity of Ru-doped titanium in the gas phase by the decomposition of acetone during irradiation at both 365 and 400 nm". To study the BG effect of the fabricated Ru-doped TiO2 samples, UV-Vi spectroscopy was used. "They established that the intensity of the absorbance in the visible region increases with the

concentration of doped Ru ions; a value of 3.20 eV is reported in the literature for pure anatase "

[77].

Reaction kinetics provides information about the reaction pathways and the rate of conversion from reactants to products. Kinetics is estimated by both the catalyst and the substrate concentrations. A recent study confirms the use of pseudo-first order kinetics to describe the photocatalytic degradation of RhB with a rate expression of $-dC/dt = k_{obs}C$ [190]. Specific rate constants and correlation to factors such as (photo) catalyst loading, co-promoter and reaction conditions are currently being analyzed and will be reported in a future publication.

2.9 Integration of Photocatalysis into Space Missions

Of particular interest for space missions is the potential applicability of photocatalysis for the decomposition of organics in order to mitigate potential health and environmental problems in the controlled environment of a spacecraft or space station, particularly for long-term manned missions. One resource common to all manned missions in the immediate future is an abundance of sunlight, which presents an opportunity to use concentrated sunlight, through the use of solar concentrators [191], to possibly enhance or augment photocatalytic process(es). Other methods may also be considered for more distant long-term missions.

The most likely scenario for a photocatalytic reactor could include a modest enhancement in the solar intensity brought about by a trough-style reactor, with reactants and catalyst flowing along the axis of the trough and therefore being illuminated for a controlled duration based on flow rate. A rigid concentrator providing a 2000:1 concentration ratio increases the intensity substantially with concurrent undesirable increases in temperature (and potential recombination of electrons and holes). A less stringent concentrator is likely to be far more desirable, one

providing a modest concentration ratio, perhaps a factor of 10:1, akin to flexible Fresnel concentrators developed in the 1990s for photovoltaics [192].

Other concepts utilizing mass produced-composite strips, developed more recently as part of a Small Business Innovative Research effort funded by NASA GRC, may also be considered as they also provide a line focus which is conducive to illuminating a lengthy reactor tube over an extended period of time when utilizing a sun tracking system. More study is needed to better understand the requirements of the receiving tube that would be located along the line focus, including such parameters as transparency, diameter and length. With the degradation reaction occurring in tens of minutes, a modest flow rate on the order of a liter per minute, and a reasonable diameter tubing machined to ensure mixing, one could envision a trough system on the order of a few meters in length to process a few liters of fluid over a few hours, suggesting a reasonable trough size. Identifying mechanisms and technologies for separating gases generated from photocatalytic reactions and recycling the catalyst, in a microgravity environment, also warrant further study.

Another scenario for a photocatalytic reactor could include illumination of the reactants and catalyst utilizing energy derived from fluorescent lamps or light emitting diodes [193]. Of course, such a scenario would need abundant electrical power for the lamps or diodes. Missions in the distant future, to locations beyond Mars where sunlight is far less abundant, could be powered via nuclear reactors, and such fluorescent lamp or light emitting diode concepts could be facilitated by greater available power.

CHAPTER 3: ZnO NANOWIRES PHOTOCATALYST

3.1 Introduction

In our industrial society, excessive amounts of organic waste (>100 kg *per capita*), including dyes, are discharged into wastewater and effluents causing significant environmental problems. Photodegradation of these contaminants via photocatalysis has become a very active research topic in the past several decades [38, 39, 85, 89, 194, 195] A growing list of semiconductor photocatalysts including WO_3, Bi_2O_3, ZnS, titanium dioxide (TiO_2) and zinc oxide (ZnO) have been employed for the remediation of organic pollutants and deactivation of numerous microorganisms due to their photocatalytic properties [42, 43, 196] ; among these, TiO_2 and ZnO are the most often studied materials.

Although, compared to other photocatalysts, TiO_2 has been the most widely investigated photocatalyst by researchers for air and water purification, ZnO is a promising substitute primarily due to its similar bad gap (~3.3 eV) [60], and quite low toxicity relative to the benchmark photocatalyst, TiO_2. Moreover, further advantages of ZnO as a photocatalyst over TiO_2, includes lower cost of production, abundance in nature, chemically-stable crystal structure and potential superior photoactivity during visible light irradiation [10, 63, 78] photocatalytic purification. The issue of ZnO photostability can be resolved by adjusting the water pH prior

---

[2]Portions of this chapter was published in Thin Solid Films (I. Udom, Zhang Y., Ram, M. K., Stefanakos, E. K., Hepp, A. F., Elzein, R., Schlaf, R., Goswami, D. Y., A simple photolytic reactor employing Ag-doped ZnO nanowires for water purification, Thin Solid Films, (2014)).

to photocatalytic decontamination. The higher photocatalytic efficiency of zinc oxide over titanium is due to higher production efficiency of electrons and prevention of electron-hole recombination, for example in the decomposition of phenol and 2-phenylphenol, [80, 82, 83]. Due to ZnO showing good number of electron trapping sites at emission close to 500 nm, Kuo et al. [197] applied a ZnO photocatalyst via a vapor transport grown technique to effectively decompose rhodamine B and 4-hydroxychlorobenzene under sunlight irradiation.

Thus, modification of ZnO photocatalyst morphology is one approach to enhancing the photocatalytic performance and potential practical applicability of the catalyst particularly in the longer-wavelength portion of the solar spectrum. To this end, there has been significant effort in increasing the aspect ratio (among several ZnO nanostructures, i.e. ZnO nanowires (NWs)) to increase the efficiency of photoreaction because molecules are adsorbed on the (relatively) larger surface (area) of the catalyst, and are eventually broken down to simpler and benign products [66, 198]. Additionally, due to its photostability and re-usability, ZnO nanowire arrays grown on inert substrates eliminate the issues (separation or low efficiency) associated with employing other photocatalyst structures, such as nanoparticles, thin films, and bulk materials for water purification [199, 200]. Compared to other fabrication techniques such as chemical vapor deposition [201], physical vapor deposition [93], and vapor liquid-solid [202], hydrothermal processes are low temperature, simple, scalable, and catalyst-free. Moreover, ZnO NWs synthesized by hydrothermal methods typically possess oxygen vacancies in the ZnO crystal [66]. To further improve photocatalytic efficiency, ZnO photocatalysts can be further modified by addition of a dopant that functions as an electron trap by suppressing electron-hole recombination. A number of transition metals including Ni [81], Co [203], Ag [204], and Mn

[205] have been used as dopants. These dopants also help in lowering the activation energy (band gap) so that the electrons are effectively excited by lower energy photons.

Enhanced photocatalytic performance was observed with doped ZnO-Cr NWs over commercial TiO_2 (P25) in the photodegradation of methyl orange (MO) [206], whereas cobalt-doped ZnO (Co-ZnO) NWs showed enhanced deactivation of 1,2-dihydroxyanthraquinone relative to TiO_2 [207]. Further, Korake et al. [208] investigated the degradation of phosphamidon, an organophosphate insecticide, using doped Ag-ZnO nanorods under visible light. Compared to data available in the literature, we observed more efficient photocatalytic decomposition as determined by degradation over time. Although transition metal doping of ZnO nanowire by several metals has been studied via several processing and irradiation methods and reported in the literature, detailed investigation of photocatalytic performance of Ag-doped ZnO NWs prepared by hydrothermal techniques warrants further investigation.

There are a variety of photocatalytic reactor configurations that have been reported in the literature including: a flat-plate reactor [209], compound parabolic collector [210], packed-bed reactors [211, 212] and a shallow solar pond [213]. Several photocatalysts, including TiO_2 and ZnO, have been studied in both suspension and immobilized systems. Photocatalyst suspension in water provides larger surface area compared to an immobilized system. However, difficulty in separation and recovery of photocatalyst is a drawback in practical applications. Goswami et al. studied the design, construction and testing of a solar photocatalytic treatment facility for a commercial site with contaminated groundwater by using flat plate solar reactors. TiO_2 was used as the catalyst in suspended mode, and was settled down at the bottom of the tank overnight at the end of treatment [213]. The result showed the flat plate solar facility worked well in field tests. Nogueira and Jardim [214] investigated a photocatalytic reactor using immobilized TiO_2 on

a flat glass plate as a support and found that reactor performance was influenced by two factors: the fluid thickness film which flowed over the plate and the light intensity that reached the system. A thick film can result in mass and light transfer limitations. In this study, we report the design of a simple, efficient and scalable photocatalytic reactor and the fabrication of an anisotropic doped ZnO and Ag-ZnO nanowire via a conventional seeded hydrothermal technique on a borosilicate glass substrate. Both grown nanowires were tested for the photodegradation of MO, a model contaminant, in water. The results were compared with P25, a benchmark photocatalyst.

3.2 Experimental Procedure

3.2.1 Synthesis of ZnO Nanowires

All chemicals used in this experiment are of analytical grade and used without further purification. Heat-resistant borosilicate glass (area: 7x2 in, 1/8 mm thickness) and aluminum sheets were purchased from the McMaster-Carr Company.

In the preparation of growth solution and seeded ZnO seed particle, a mixture of equimolar ratio (25mM) of hexamethylenetetramine ($C_6H_{12}N_4$) and zinc nitrate hexahydrate ($Zn(NO_3)_2 \cdot 6H_2O$) were dissolved in water to form the growth solution. The preparation of a ZnO seed particle solution involves preparation of an aqueous solution of 5mM zinc acetate ($Zn(CH_3COO)_2$) in ethanol.

In the fabrication of ZnO NWs, an aliquot of 0.5 ml seed particle solution was placed on the substrate (borosilicate glass or silicon wafer) and randomly tilted in different directions to ensure uniform distribution. The seeded substrate was dried in an oven at 100 °C for 10 min to remove moisture and another 30 min. at 350 °C to remove unreacted organic matter. After cooling, the substrate was placed in a reactor containing the growth solution, and stirred for 2

hours at 90 °C. After this step, the substrate was rinsed with water and oven dried at 100 °C for 10 min. and 350 °C for 30 min.

A seed solution of equimolar ratio (5 mM) of $AgNO_3$ and $Zn(CH_3COO)_2$ in ethanol was prepared; a 1.25 ml aliquot of this solution was placed on a substrate. The rest of the growth process was completed similar to the ZnO NW growth. After several growth cycles, the mean weight of doped and undoped ZnO NW photocatalysts was determined as shown in Table 6.

3.2.2 Photocatalyst (P25) Coating

To compare the photoactivity of prepared ZnO NWs (doped and undoped) to P25, a commercial TiO_2 photocatalyst (Degussa P25) was immobilized on borosilicate glass plates by a spray coating method. The plates were cleaned by 190 proof (95%) ethanol prior to spraying. The same amount of nanowires, 100 mg of TiO_2 powder was suspended in 50 ml 95% ethanol to produce a TiO_2-ethanol slurry. The slurry was stirred by a mini-vortexer for 5 min to enhance slurry uniformity. The suspension was evenly sprayed on the cleaned glass plates using a Paasche HAPK airbrush. After spraying, the glasses were maintained at room temperature for 1h and then dried in an oven at 80 °C for 30 min, 105 °C for 30 min, and 400 °C for 2 hours. The catalyst plates were tested in a commercial dishwasher to make sure that the catalyst adhered well to the plates. Due to some uncertainty about TiO_2 being sprayed outside the plate, the amount of TiO_2 sprayed on the plate (W) is calculated from:

$$W = \frac{V_s \times C_{TiO_2}}{A_s} \times A_p \qquad (11)$$

W is the total weight of TiO_2 sprayed on the plate, V_s is the volume sprayed, C_{TiO2} is the concentration of the TiO_2-ethanol solution, A_s is the area of spray and A_p is the area of the plate.

3.2.3 Photolytic Reactor Design and Fabrication

A photolytic reactor was designed and built "in-house" (see Fig. 17). The reactor consists of a water channel with a 25.4×50.8 mm (1×2 in., H×W) cross-section and 380 mm (15 in.) length. A reflective aluminum sheet (0.559 mm thickness) is used to build the reactor channel. Water inlet is at a side-wall under the inlet cover and water outlet is at bottom wall under outlet cover which is shown in the Fig. 17a.
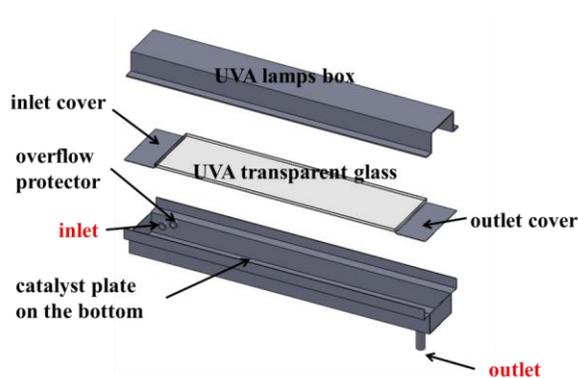
a
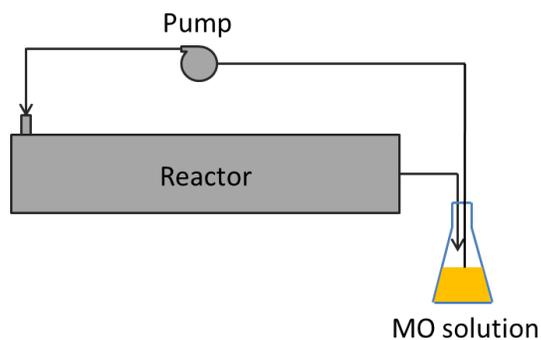
b

Figure 17 Scheme of: (a) photocatalytic reactor and (b) reactor system

The catalyst plates are 50.8×177.8 mm borosilicate glass with photocatalyst coated on it. A UVA transparent glass (76.2×304.8 mm) and two reflective aluminum sheets (76.2×38.1 mm) are used as lid of the channel. A UVA lamp box is placed on the top as the light source. The

lamp box consists of two Southern New England Ultraviolet Company Rayonet RPR-3500 Å

UVA lamps (304.8 mm long) and a reflective cover. The UV lamps were later replaced with a

white light to emit radiation in the visible range in a wavelength range > 400 nm with an

approximate Gaussian spectral distribution (λ_{max} = 350 nm). The spectral distribution shows the

intensity of irradiation at different wavelengths. The reflective cover was made from a reflective

aluminum sheet.

3.2.4 Evaluation of Photocatalytic Activity

The photocatalytic reactor (Fig. 17) was tested in the clean-up of 200 ml of 20 ppm MO

in water. A water pump (Masterflex L/S) was connected to the reactor, and pumped the water

from beaker to the inlet port, see Fig. 17. The water went through the reactor and returned to the

beaker from outlet port. The average UV intensity on the catalyst plate level was measured by an

LI-COR pyranometer and was equal to 70 W/m^2, while the visible was determined to be 80

W/m^2. The experiment was carried out at room temperature (293K). An Ocean Optics

spectrophotometer was employed to analyze the sample and monitor the photodegradation and

decolorization of the MO by detecting the absorption at the maximum of 460 nm.

Table 6 Mass of prepared nanowires on 50.8 x 117.8 mm^2 borosilicate glass

Experiments	1	2	3	4	5	Average
Weight of catalyst (mg)	100.4	98.1	97.5	99.5	102.8	99.7

3.2.5 Characterization

Scanning electron microscopy (Hitachi S-800, 25eV) was used to observe the crystalline

structure and orientation of the prepared nanowires. The diffraction pattern has been measured

using an analytical Philips X-pert Pro X-ray Diffraction (XRD) for 2θ angles ranging from 5 to

50 degrees. An Ocean Optics spectrophotometer was used to acquire the UV-Vis diffuse reflection spectra.

3.3 Results and Discussion

3.3.1 The Weight of Prepared Nanowires

Table 6 lists the individual weights of the NW arrays grown on two catalyst plates (borosilicate glass), place at the bottom of the channel. The homogenously distributed NWs were fabricated for a total of 2 hours with an estimated density of 0.495 mg/cm^2. In the preparation of Ag-ZnO NWs, various volumes of seed solution (1300 ml – 3000 ml) containing equimolar (5 mM) of AgNO$_3$ and zinc acetate in ethanol were used in the formation of the seed layer. Thus, Ag-ZnO film containing different concentrations of Ag atoms is expected to be in the seeding layer. The estimated percentage of Ag atoms in the prepared Ag-ZnO nanowires from 1300 ml, 2300 ml and 3000 ml seeding solutions were 0.7%, 1.2% and 1.6%, respectively.

3.3.2 Structural and Morphological Characterization Studies

The SEM micrographs, depicted in Fig. 18 illustrate the similar morphology of the ZnO and doped Ag-ZnO nanowires with varying in the size of nanowires. The diameter and length of ZnO nanowires vary from 30-70 nm and 280-420 nm with average diameter and length to be 55 nm and 400 nm. The diameter and length of Ag-ZnO nanowires vary from 40-70 nm and 300-500 nm with average diameter and length to be 65 nm and 450 nm, respectively The diameter of the prepared nanowires is influenced by the thickness of the seed layer due to the consumption rate of ZnO $^{2+}$, growth rate of nanowires side walls and nanowires density [43]. Tips of the nanowires are observed to have a predominantly hexagonal structure, in good agreement with results obtained by Wang et al. [215].

The XRD shown in Fig. 19 reveals that both synthesized nanowires show the (002) plane as a dominant reflection, a pattern initiated by the predominant growth of the wires along the c-axis perpendicular to the substrate surface. The XRD results reveal that the ZnO and Ag-ZnO nanowires are highly crystalline. From the XRD data, no significant difference in the diffraction pattern was observed between the undoped (ZnO) and doped ZnO (Ag-ZnO) nanowires, due to extremely low doping of Ag atom in the ZnO lattice. Additional explanation is that Ag atoms are deposited near the surface of the Ag-ZnO samples [27].

UV-Vis (electronic) absorption spectrum comparing both nanostructures is shown in Fig. 20. Within the visible range, 400-700 nm, Ag-ZnO nanowires show better absorption compared to ZnO nanowires. Also, the former shows better absorption in UV irradiation, demonstrating a better catalyst for photocatalytic technologies under solar illumination.

The possible states of Ag element in as-prepared catalyst Ag-ZnO nanowire were investigated by a commercial multichamber system SPECS GmbH (Berlin, Germany) under ultrahigh vacuum conditions (2×10^{-10} mbar base pressure), consisting of two preparation chambers and one x-ray photoemission spectroscopy analyzing chamber. Based on the XPS data (Fig. 21), peaks of Ag 3d5/2 and Ag 3d3/2 are clearly located at 374.1 and 367.6 eV. The binding energies clearly reveal that Ag is deposited on the ZnO nanowires. Further experiment is required to confirm the oxidation state of silver atom in the catalyst, the identity of its nearest-neighbor atom, its bonding hybridization to that nearest-neighbor atom, as well as the bonding hybridization between the Ag atom in question and the next-nearest-neighbor atoms.
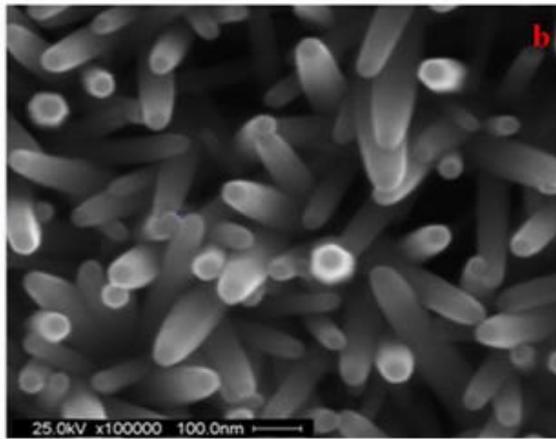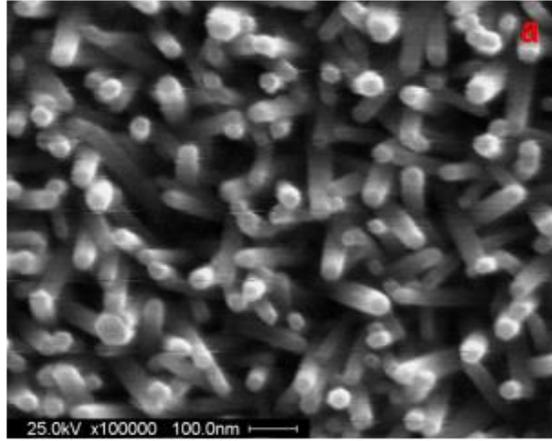
Figure 18 SEM images: a) ZnO nanowires b) ZnO/Ag nanowires
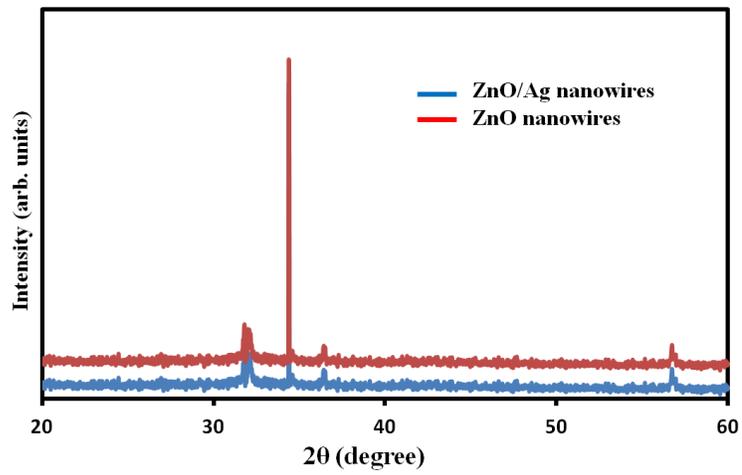
Figure 19 XRD powder patterns of ZnO (blue) and ZnO/Ag (red)
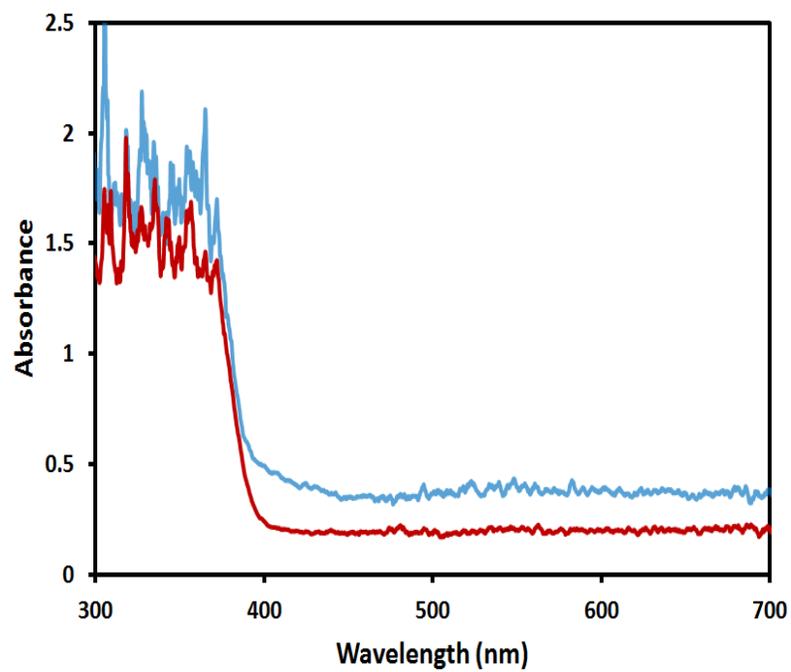
Figure 20 UV-vis absorption spectra of ZnO (blue) and ZnO/Ag (red)
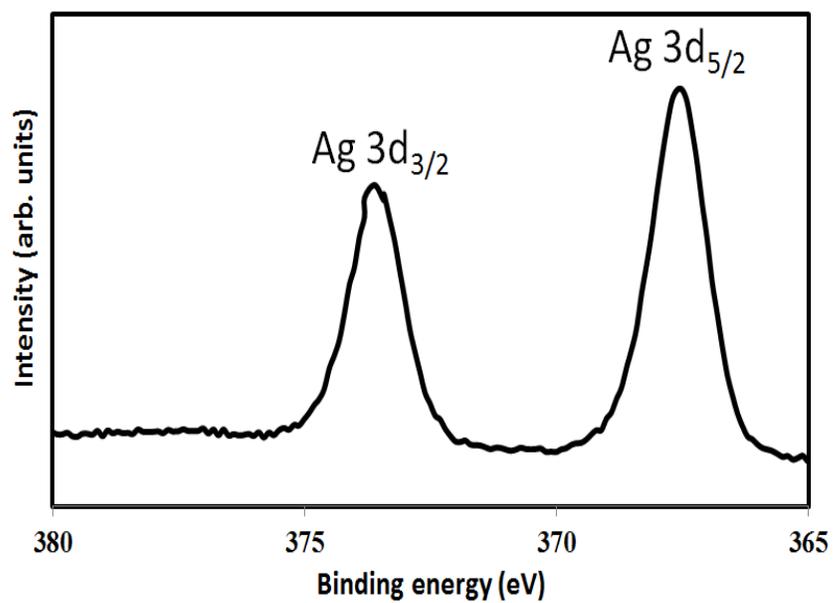
Figure 21 XPS spectra of the as-synthesized sample of Ag-ZnO nanowire

3.3.3 Optimization of Photocatalytic Reactor

Once the photoreactor was designed and fabricated, the operating parameters were optimized for the degradation of MO under visible and UV light irradiation. The reactor was effective using sprayed P25 on borosilicate (or soda lime) glass. The impact of experimental parameters including water flow rate and/or depth was investigated to achieve optimal conditions for effective operation (Table 7). In the degradation of 20 ppm MO with 0.50 mg/cm^2 of TiO$_2$ catalyst sprayed on the glass, there was no significant difference in the photodegradation efficiency within a flow rate range 60-300 ml/min. However, increased water depth reduced the overall reaction, with a net lowering of efficiency. This could be due to the absorption of UV light by the MO solution, blocking photons from reaching the active reaction sites. Optimization values achieved for the fabricated photoreactor for the degradation of 200 ml of MO at initial concentration of 20 ppm at room temperature were found at (Table 7): catalyst loading of 0.50 mg/cm^2, UV light intensity 47.2 W/m^2, flow rate 60 ml/min and water depth 2 mm.

3.3.4 Photocatalysis Studies

Once the optimization of the operational parameters of the photocatalytic reactor using 100 mg of P25 (TiO$_2$) at initial concentration of MO of 20 ppm was established, an initial study was conducted with different doping levels of Ag for the degradation of MO under UV irradiation to determine best dosage for further study (data not shown). It was found that photocatalytic activity and target percentage of Ag doping in ZnO varies in the following order: Pure ZnO<Ag-ZnO (0.5%) < Ag-ZnO (1.0%) > Ag-ZnO (1.9%) < Ag-ZnO (1.2%). Based on these experimental results, Ag-ZnO (1.2%) was selected for further study because it inferred the highest photodegradation efficiency; Ag doping levels beyond the optimal point resulted in reduced efficiency.

56

Subsequently, the photocatalytic activity of ZnO and Ag-ZnO nanowires was evaluated, and compared to P25 for the degradation of MO in water at initial concentration of 20ppm in visible and UV light (Fig. 22). In Figure 22a, Ag-ZnO (1.2%) has shown a significantly higher photodegradation performance than ZnO, while similar results were obtained when compared to TiO_2 under visible light for 4 h. Under UV light irradiation, ZnO nanowires revealed less photocatalytic performance than Ag-ZnO nanowires, while TiO_2 demonstrated the similar performance as the doped Ag-ZnO nanowires.

Variation in the activity of the different dosage (Ag %) were most likely due to the Ag atom which captures electrons and enhances the separation of electron-hole pair. Photocatalytic performance of Ag-ZnO nanowire was parallel to those observed by Ren et al [38]. In a similar result under visible light irradiation, without any surfactant, ZnO/Cr nanowires prepared by

Table 7 Effect of water flow rate and depth in the reactor on photocatalytic degradation of methyl orange after 4 h with sprayed P25 film as catalyst

MO solution flow rate (ml/min)	MO solution depth (mm)	% MO degradation in 4 h	Best operating condition
50	2	88	
62	2	98	62 ml/min
150	2	99	
300	2	99	
62	1	84	
62	2	97	2 mm
62	4.5	94	

solvothermal technique revealed higher photocatalytic degradation of MO solution compared to ZnO nanowire and P25. The visible light photoactivity could be credited to the modification of interactions between the conduction band (CB) and valence bands [216]. Further, doped ZnO/Sb (Antimony) and ZnO nanowires were fabricated via a vapor-solid method and tested for photoactivity performance under visible and UV light. The doped catalyst has shown a superior photocatalytic performance over ZnO nanowires base on the effect of oxygen defect and reduction of electron/hole recombination [217].

In a related work of photocatalytic activity of Ag-ZnO nanorods, though synthesized by a photolytic deposition method, the mechanism of photodegradation of MO typically involves a combination of hydroxylation and demethylation [218]. Hydroxylation breaks the nitrogen–carbon bond of the R-N(CH$_3$)$_2$ group as a result of hydroxyl (OH•) radical attack on an aromatic ring. Subsequently, the terminal R-N(CH$_3$)$_2$ group loses a -(CH$_2$)- via substitution by a hydrogen (H) atom, this process is called demethylation. Further hydroxylation and demethylation reactions break down the intermediate by-products into simpler compounds eventually producing carbon dioxide and water.

3.5 Catalyst Stability and Reusability

A major drawback of ZnO photocatalysts is the photocorrosion induced by electron/hole separation; this is a vital concern for multiple applications of the photocatalyst, particularly for a large-scale production and commercialization. The photocatalytic experiments were conducted over several cycles similar to as-prepared catalysts (ZnO, Ag-ZnO nanowires (1.2 %) and P25) at 20 ppm of MO for 2 h under UV-light irradiation (Figure 23). After each experiment, the catalysts were rinsed repeatedly with water, dried and used for the next experiment. After the fourth cycle, the photoreduction of MO by the catalysts were 61 %, 76 %, 80 %, respectively.
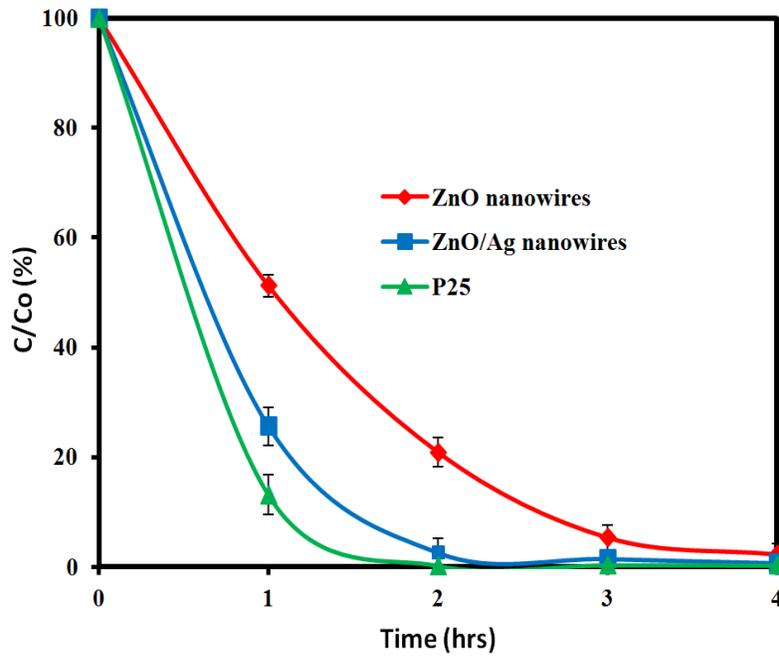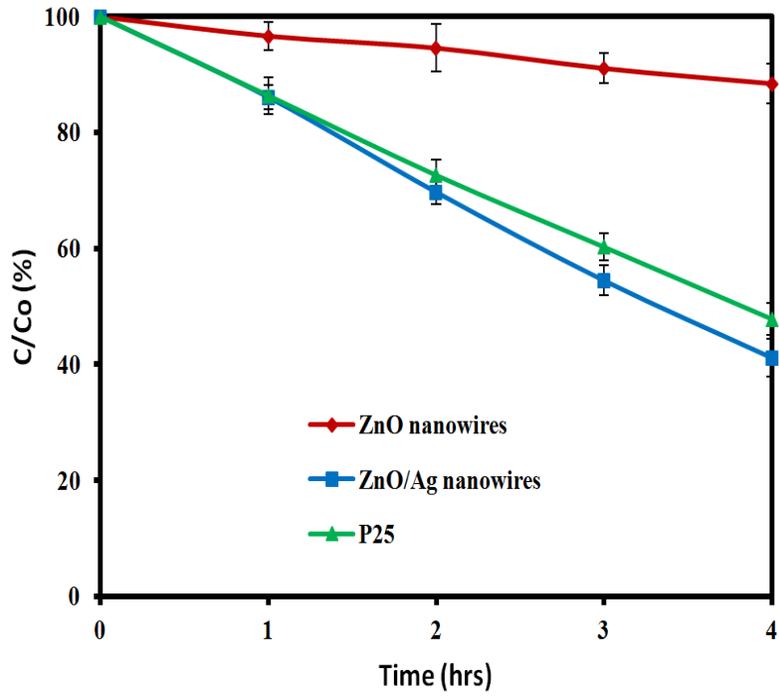
Figure 22 Photodegradation of MO under: visible (top) and UV (bottom) light irradiation

.

Although ZnO nanorods array were fabricated by a combined wet chemical and photolytic deposition method by Ren et al. [219], similar photostability results were reported. Clearly photocorrosion, due to several competing factors, is a complex process requiring further investigation.
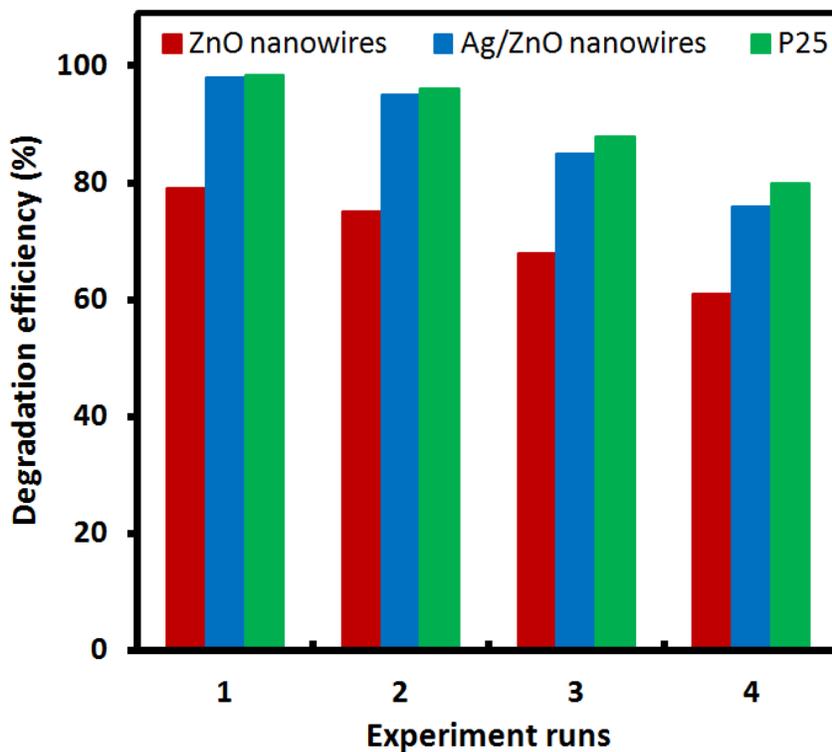
Figure 23 Repeated cycles of MO photodegradation using ZnO, Ag-ZnO nanowires and P25 catalysts under UV irradiation for 2 hours

CHAPTER 4: PHOTOCATALYTIC DEGRADATION OF PHENOL

4.1 Introduction

Phenols are among the numerous organic pollutants and toxic chemicals discharged into the aquatic environment that cause negative flavor and unpleasant odors in potable water. Phenols are recalcitrant and stem from industrial sources, including pesticide, paint, petroleum and petrochemical industries, to mention a few [195, 220, 221]. Despite their low dosage, these pollutants may pose a major health hazard due to their mutagenicity and genotoxicity. Phenols are mutagenic and may be absorbed through the skin and harmful even at low dosage [222, 223]. Hence, degradation of phenol is important. A large body of researchers have worked on a number of remediation processes and come up with several chemical [224-226], biological [227], and physical [228, 229] processes. Since the application of these processes involve high cost and could possibly introduce more contaminants into the environment, developing energy efficient and 'green' technologies to minimize these limitations while producing the desired complete mineralization of organic contaminants is of particular importance. Advanced oxidation processes (AOP), a process of mineralization of organic compounds into simple products such CO_2 and water, has emerged as the most promising technology in the last few decades [230-232]. Among the semiconductors for AOPs, TiO_2 and ZnO are the most often studied materials and

_____

[3]Portions of this chapter is presently in press in American Journal of Analytical Chemistry (I. Udom, P. Meyers, Y. Zhang, M. K. Ram, A. F. Hepp, E. K. Stefanakos, D. Y. Goswami, Optimization of photocatalytic degradation of phenol using simple photocatalytic reactor, American Journal of Analytical Chemistry).

employed due to their ability to produce hydroxyl radicals to destroy numerous types of organic contaminants [233]. Moreover, they are non-toxic, cheap and abundant.

A number of researchers have investigated the photodegradation of phenol using metal-doped photocatalysts, for example, Grabowska et al. [220] reported a three times higher photodegradation with 3% -W-TiO$_2$ compared to pure TiO$_2$ under visible light irradiation. In the presence of W-TiO$_2$ under visible light phenol was degraded to catechol and muconicaldehyde. Devi and Rajashekhar [234] doped TiO$_2$ with N$_2$ gas to mineralized phenol under visible and UV light irradiation. Higher photodegradation was achieved with 0.15% dopant concentration compared to sol-gel TiO$_2$ for the photodecomposition of phenol under UV/solar irradiation employing H$_2$O$_2$and ammonium peroxydisulfate as acceptors. Furthermore, Kavitha and Palanivelu [235] conducted a batch study of using phenol as a model pollutant in industrial water to optimize parameters such as a pH, hydrogen peroxide and ferrous oxide concentrations affecting Fenton-related oxidation reaction. The highest photodegradation efficiencies were Fenton (41%), solar (96%) and UV-Fenton (97%) processes.

As evident from the literature, not much research has been done in optimization of photodegradation of phenol with immobilized ZnO-Ag nanowires using a simple photocatalytic rector under UV irradiation.

4.2 Experimental

4.2.1 Materials

All chemicals are of analytical standard and were used without further purification. Silver nitrate (AgNO$_3$, 99.9%) was purchased from Sigma-Aldrich and used to provide doping, zinc acetate [Zn(CH$_3$COO)$_2$, 99.9%] was procured from Fisher Scientific. Sodium hydroxide

(NaOH, 44%) and hydrochloric acid (37%) were also obtained from Fisher Scientific. The double-distilled water was employed to prepare the desired phenol concentration.

4.2.2 Photoreactor

All experiments were carried out in a laboratory fabricated aluminum photoreactor with dimension of 38.1 cm (15 in) long by 5.1 cm (2 in) wide by 2.5 cm (1 in) high. Aluminum sheet of 5.6 cm was used to build this reactor. A peristaltic pump (Masterflex L/S, 160 ml/min flow) was connected and pumped water from the glass beaker to the reactor. The water circulated through the reactor and returned to the beaker continuously during the experiment. The reactor system contained a lid, a UVA transparent glass, which was employed to prevent evaporation. The vessel top contains a light source. A lamp box which consisted of two Southern New England Ultraviolet Company Rayonet RPR-3500 Å UVA lamps (30.5 cm long) was used; the lamps provided irradiation in the UVA range of 350 – 400 nm. Other information about the photoreactor can be found at Udom et al. [236]. The light intensity at the surface of the reactor in the photoreactor was measured by an LI-COR pyranometer.

4.2.3 Preparation of Ag-Zn NWs

A seed solution of equimolar ratio (5 mM) of $AgNO_3$ and $Zn(CH_3COO)_2$ in ethanol was prepared; a 1.25 ml aliquot of this solution was placed on a substrate. An aliquot of 0.5 ml seed particle solution was placed on the substrate (borosilicate glass) and randomly tilted in different directions to ensure uniform distribution. The seeded substrate was dried in an oven at 100 °C for 10 min to remove moisture and another 30 min. at 350 °C to remove unreacted organic matter. After cooling, the substrate was placed in a reactor containing the growth solution, and stirred for 2 hours at 90 °C. After this step, the substrate was rinsed with water and oven dried at 100 °C for 10 min. and 350 °C for 30 min.

4.2.4 Procedure and Analysis

The reaction mixture was initially placed in the dark for 30 min to establish adsorption equilibrium of phenol solution on the photocatalyst and then UV irradiated for 150 min. At certain interval, aliquots (5ml) were collected and analyzed to assess photodegradation. Gas chromatograph (SRI8600) with 3000 cm DB-624 capillary column and flame ionization detector (FID capability was employed to study the degradation of phenol analytes. To evaluate the impact of initial concentration and catalyst dosage on photocatalytic efficiency, experiments were performed at initial phenol concentration from10 - 60 mg/L and catalyst loading 250 - 7500 mg/L. After determination of the optimal values, additional parameters including pH and light intensity were investigated for optimization and a model was established. Diluted NaOH and HCl were used to adjust pH within range 2.7 to 11 and was measured using Orion 5 Star ThermoScientific. The unadjusted initial phenol solution measured pH 8.2.

4.3 Result and Discussion

4.3.1 Effect of Initial Phenol Concentration

The effect of initial phenol concentration on the removal rate equation is vital for the optimization of the different concentration of phenol and development of a model. The reaction rate constant, K (min^{-1}), decreases as the initial concentration increases while holding other parameters constant. This could be due to saturation of active sites on the photocatalyst by intermediates, hereby creating fewer sites for adsorption and creation of hydroxyl ions. Unlike other contaminants, the transmittance of UV light through the aqueous solution of phenol, due to its transparency, does not contribute to the decrease in rate constant. In the Figure 24, the empirical first-order relationship of different initial concentrations of phenol to the reaction rate constant is illustrated. Shukla et al. [237] examined the role of initial concentration (12.5 -37.5

ppm) in the photodegradation of phenol. Optimum value was achieved at 12.5 ppm, under the conditions studied (ZnO = 0.4 g/L, persulfate = 2g/L and power = 330W). Pardeshi and Patil demonstrated that the degradation of phenol decreased as the phenol concentration increases in range 25 300mg/L [66]. Due to the constant reaction condition, the lesser amount of OH and O_2 radicals are available as more and more substrates molecules are adsorbed on the surface on the photocatalyst.
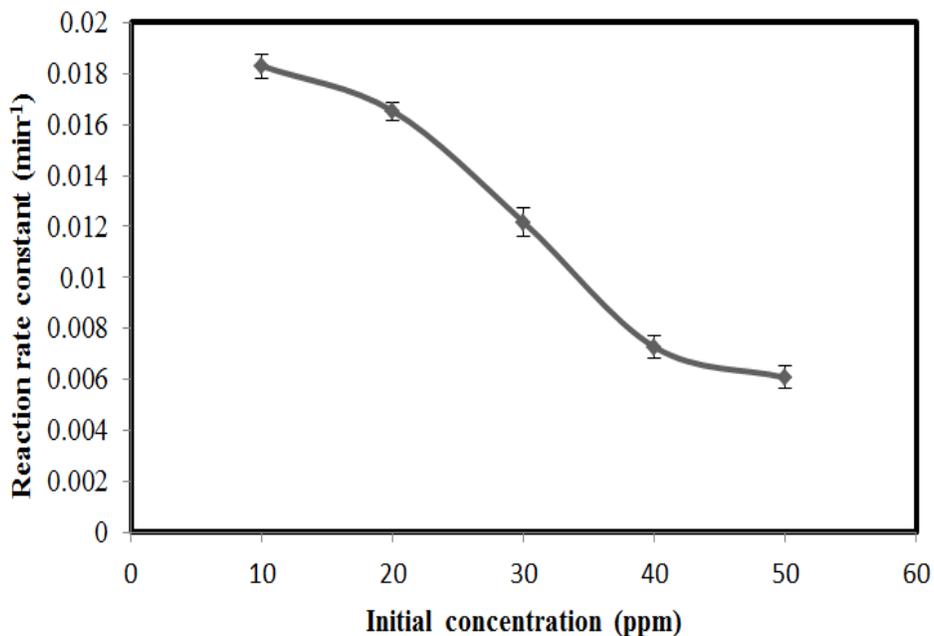
Figure 24 Effect of the initial concentration of phenol on reaction rate constant.
Ag-ZnO NW = 500 mg/L, T = 295 ± 2 K, pH =8.7, Light intensity = 60 W/m^2

4.3.2 Effect of UV Intensity

The effect of UV light intensity on the photocatalytic degradation of aqueous organic compound is significant, as the UV irradiation creates the photons needed to move electrons from the valence band to the conduction band of the semiconductor photocatalyst. The irradiation produces the energy to drives the overall reaction, thus the reaction rate constant depends on the intensity of the irradiation. The rate of photocatalytic mineralization of phenol

65

increases as more photons (increasing radiation) of sufficient energy reach the surface of the catalyst. The light intensity plays a key role in the initiation of electron-hole formation in the photochemical reaction. Chiou et al. [238] examined the effect of UV light intensity (20-40 W) on the phenol degradation. Under UV irradiation over TiO_2 photocatalyst, the reaction rate constants were 0.0083, 0.012 and 0.031 min^{-1} with light intensity of 20, 100 and 400 W, respectively. A more or less linear correlation was established between the rate constants and light intensity. Ollis et al. [239] have studied the photocatalytic degradation of organic pollutants such as benzene and perchloroethylene in UV/TiO_2 system at intensity within the range ≤ 25 mW/cm^2 and above. They reported that the reaction rate was independent of the light intensity at a higher intensity.
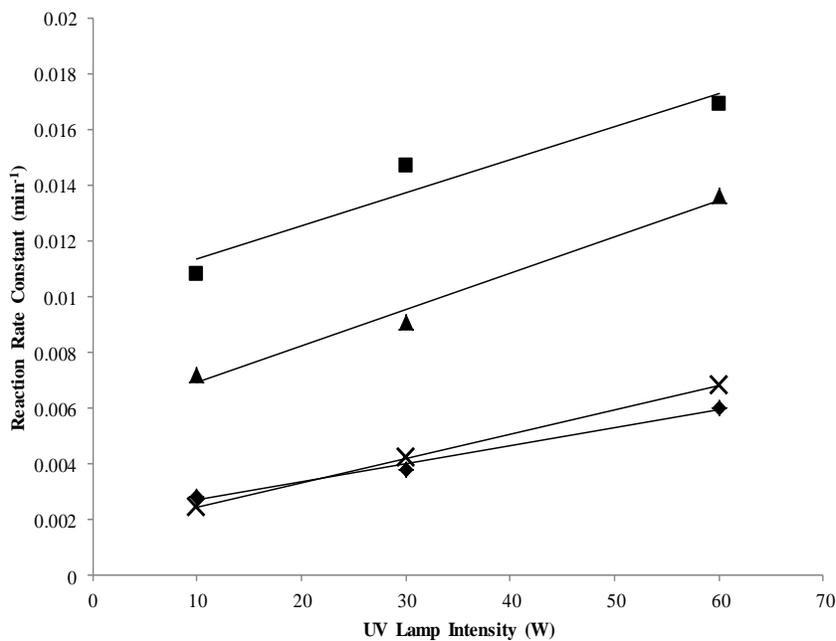
Figure 25 Effect of the UV light intensity on reaction rate constant. Ag-ZnO NW = 500 mg/L, T = 295 ± 2 K, initial concentration = 30 ppm, and pH = 2.7 (♦), 5.0 (■), 8.7 (▲), and 11 (×)

In this study, varying intensities of UV radiation (10, 30, and 60 W) were used with Ag-ZnO NWs to catalyze the degradation of phenol in water at varying pH (2.7, 5.0, 8.1, and 11.0).

The data are plotted in Figure 25 as reaction rate constant versus UV lamp intensity. Approximate linearity with respect to lamp intensity is observed at each pH level considered.

4.3.3 Effect of pH

The role of pH on the performance of photocatalytic degradation of phenol was investigated in the pH range 2.7 – 11; the results are plotted in Figure 26. The three sets of data, reaction rate versus pH level, correspond to data collected at constant UV lamp intensity (10, 30, or 60 W). While the choice of interpolation curve is somewhat arbitrary (for each set of data, a cubic polynomial is fit to the data points), each curve suggests a maximum reaction rate at a pH level of approximately 5.5 – 6.0. At pH (5-6), most of the phenol molecules are adsorbed on the surface of the photocatalyst due to the undissociated nature of the phenol thereby producing higher photocatalytic efficiency. The surface of the photocatalyst is negatively charged, at higher pH (higher alkalinity), phenolate intermediates may be repelled away from the catalyst surface thereby opposing adsorption of contaminant molecules. As a result, lower degradation of phenol is observed in alkaline environments. Similar results were reported by Pardeshi and Patil [66] and Lathasree [240]. Also, Akbar and Onar [241] studied the effect of pH on the photodegradation of phenol at the pH range 3-8. At mildly acidic condition, such as pH 5, the highest photocatalytic activity was observed, while addition of an oxidant/electron acceptor (H_2O_2) to the system increased phenol degradation to 99.2 %.
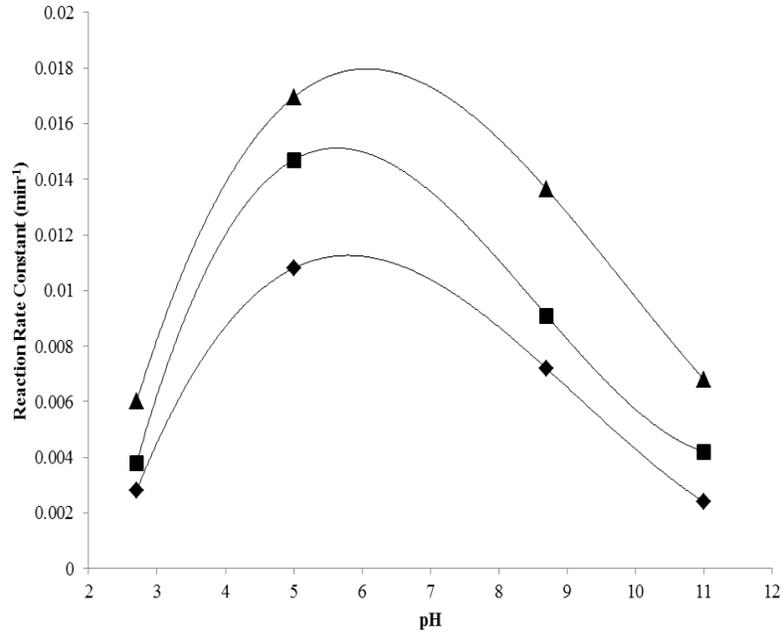
Figure 26 Effect of pH on reaction rate constant. Ag-ZnO NW = 500 mg/L, T = 295 ± 2 K, initial concentration = 30 ppm, and UV lamp intensity = 10 W (◆), 30 W (■), and 60 W (▲)

4.3.4 Empirical Correlation

In formulation of a complete model equation for the degradation of phenol by Ag-ZnO nanowires at varying pH and UV intensities, the data and their dependence on each variable initially were examined separately, as depicted in Figures 23 and 24. As can be seen in Figure 23 the dependence on UV lamp intensity is adequately modeled by a linear equation; that is: $K(I) = a_1 I + a_0$. Here, I is the UV lamp intensity, in W, and , a_1 with units of $W^{-i} \, min^{-1}$, represents the constants that fit the empirical model to the collected data. Similarly, the data suggest that the pH dependence can be captured by a polynomial, albeit with more terms. In other words:

$$K(\text{pH}) = \sum_{i=0} b_i \text{pH}^i$$

For the case of a cubic polynomial, for instance:

68

$$K(\text{pH}) = b_3\text{pH}^3 + b_2\text{pH}^2 + b_1\text{pH} + b_0$$

Here, b_1 (units of min^{-1}) likewise represents the constants of the empirical model. In fitting the multivariate model, the most obvious choice for a mathematical description of the data would be a similar polynomial, which can be formulated as follows;

$$K(I, \text{pH}) = \sum_{i=0}\sum_{j=0} c_{ij}I^i\text{pH}^j$$

In this case, C_{ij} (W^{-i}min^{-1}) represents the constants of the multivariate model. In fleshing out the form of the final model, it is useful to recall the linearity of the data with respect to variable UV lamp intensity; hence, in this study, we neglected any terms of quadratic or higher order in intensity. Similarly, we recognize that, given that cubic polynomials capture the pH dependence quite well, we can neglect quadratic and higher order terms in pH (i.e., $j \le 3$).

The data obtained from experiment were fitted to potential polynomial models using a least-squares regression. The results of the analysis of various potential models are tabulated as shown in Table 8. For each equation, derived constants and the corresponding coefficient of determination (R^2) are given.

Table 8 Derived model parameters and coefficient of determination for candidate model equations

Model equation	c_{00}	c_{10}	c_{01}	c_{11}	c_{02}	c_{12}	c_{03}	c_{13}	R^2
$c_{00} + c_{10}I + c_{01}\text{pH}$ $+ c_{11}I\,\text{pH} + c_{02}pH^2$	-0.01392	8.116E-05	0.007423	2.846E-06	-5.604E-04				0.8943
$c_{00} + c_{10}I + c_{01}\text{pH}$ $+ c_{11}I\,\text{pH} + c_{02}\text{pH}^2$ $+ c_{12}I\,\text{pH}^2$	-0.009616	-4.796E-05	0.005811	5.118E-05	-4.428E-04	-3.528E-06			0.9057
$c_{00} + c_{10}I + c_{01}\text{pH}$ $+ c_{11}I\,\text{pH} + c_{02}\text{pH}^2$ $+ c_{12}I\,\text{pH}^2 + c_{03}\text{pH}^3$	-0.02801	-4.796E-05	0.01637	5.118E-05	-0.002168	-3.528E-06	8.393E-05		0.9934
$c_{00} + c_{10}I + c_{01}\text{pH}$ $+ c_{11}I\,\text{pH} + c_{02}\text{pH}^2$ $+ c_{12}I\,\text{pH}^2 + c_{03}\text{pH}^2$ $+ c_{13}I\,\text{pH}^3$	-0.02819	-4.257E-05	0.01648	4.808E-05	-0.002184	-3.023E-06	8.475E-05	-2.459E-08	0.9934

It can be seen that on the basis of the coefficient of determination, the best fit is given by the following equation:

$$K(I, \text{pH}) = c_{00} + c_{10}I + c_{01}\,\text{pH} + c_{11}I\,\text{pH} + c_{02}\text{pH}^2 + c_{12}I\,\text{pH}^2 + c_{03}\text{pH}^3$$

This equation is plotted in Figure 27 with experimental data for comparison. It is interesting to note that the addition of the $c1^3\,I\,pH^3$ term does nothing appreciable to improve the accuracy of the fit of the model equation. Also, the authors examined higher order polynomials with similar deficiency in accuracy: a simple quadratic polynomial gives an R^2 value of 0.9866. As such, the above equation is recommended for further design calculations and scale up of the bench scale reactor.
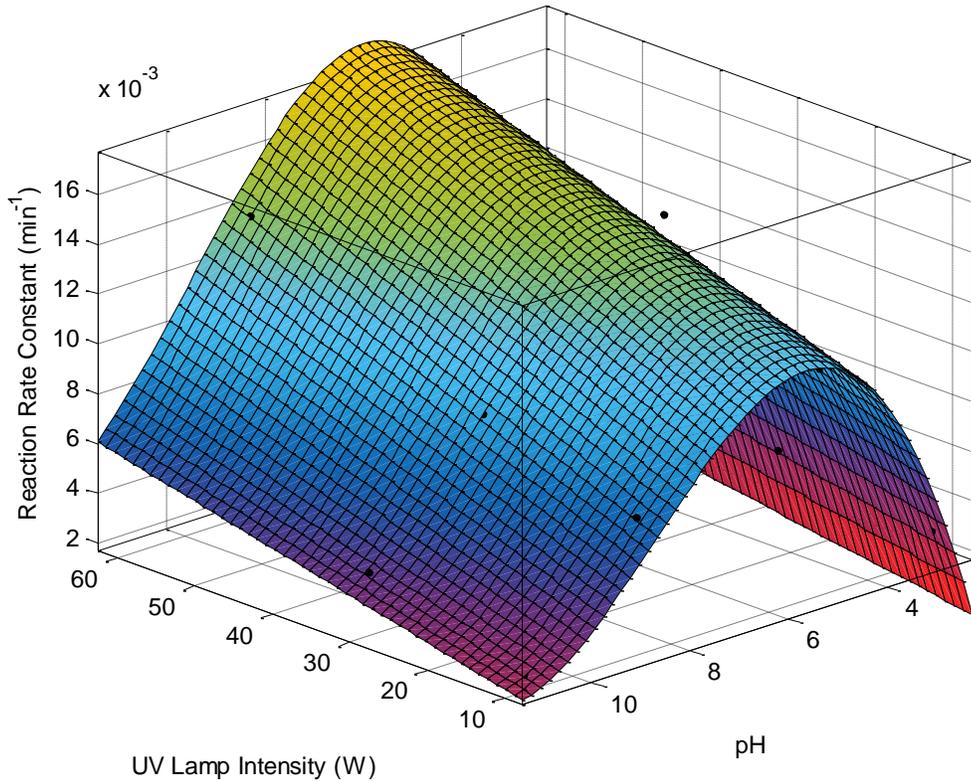
Figure 27 The recommended polynomial model equation plotted on three axes as a surface with experimental data (•) overlain

Finally, we consider the uncertainty in the derived model equation parameters. For the chosen equation, 95% percent confidence intervals were generated for each equation parameter; the results are presented in Table 9. It can be seen that while a good fit was obtained, on the basis of the coefficient of determination, there is a good degree of variability over the 95% confidence intervals for most of the model parameters. It may be beneficial as a part of future investigative work to examine operating conditions of intermediate pH and / or UV intensity to the work considered here; by considering a greater breadth of data, a greater degree of certainty regarding the equation parameters of the resultant model may be obtained.

Table 9 Derived model equation with parameter values of >95% confidence intervals

$c_{00} + c_{10}I + c_{01}\text{pH} + c_{11}I\,\text{pH} + c_{02}\text{pH}^2 + c_{12}I\,\text{pH}^2 + c_{03}\text{pH}^3$		
Parameter	Value	95 % Confidence Interval
c_{00}	-0.02801	-0.03554 – -0.02048
c_{10}	-4.796E-05	-1.710E-04 – 7.504E-05
c_{01}	0.01637	0.01265 – 0.02009
c_{11}	5.118E-05	8.586E-06 – 9.377E-05
c_{02}	-0.002168	-0.002723 – -0.001612
c_{12}	-3.528E-06	-6.599E-06 – -4.564E-07
c_{03}	8.393E-05	5.752E-05 – 1.103E-04

CHAPTER 5: CONCLUSIONS AND FUTURE WORK

As presented in Chapter 1, the research includes three main goals:

a. Determine the effect of transition metal dopants on photocatalytic material performances.

b. Development of a simple, inexpensive, scalable and effective ZnO nanowire (NW) photocatalyst by modifying the morphology via a synthesis method.

c. Optimization of the photocatalytic degradation of phenol using a simple photocatalytic reactor.

Relative to the first goal, Chapter 2 reported the materials characterization analysis which showed that we have successfully produced different photocatalysts promoted using transition metal co-catalysts with various concentrations (1 to 5 percent) and using anatase or mixed anatase and rutile (P25). EDS confirms an approximate elemental composition of each of the promoted photocatalysts. However, some of them did not yield the expected weight percent target. As seen in the SEM photographs, the catalyst particles tend to conglomerate smaller particles on the surface, probably from co-promoters. Five weight-percent Cu in anatase and P25 proved to be ineffective. 1% wt. Pt in P25 proved to be effective. The best catalyst in this study was 1% wt. Ru in anatase. According to the XPS data, Ru is in the more reduced state with a BE of ~ 281 eV (Ru(0)) and minor phase RuO_2 in P25, similar to Cu (above). The resolution between the peaks from 279.0 to 283.0 eV is poor due to interference from C. These trends can be best explained by assuming that metallic Ru (denoted as Ru(0) or Ru^0) has emerged by the

high-temperature treatment, with the higher surface area P25. The contribution of the oxidized

RuO_2 (~ 283 eV) is more pronounced on anatase.

Future work will include testing of the photocatalyst in a UV reactor to determine how

effective it is in the decomposition of other organic compounds.

In Chapter 3, a facile technique, hydrothermal processing, was successfully employed to

fabricate ZnO and Ag-ZnO nanowires on reaction plates. This alternative approach is simple,

scalable, cost effective and environmental friendly for the production of quality Ag-ZnO, with

enhanced photocatalytic activity for water purification. The conclusion of this study also

indicates that Ag-ZnO nanowires shown better photocatalytic performance, in both light sources,

than ZnO nanowires, and a similar level of performance with P25. For future work, the

fabricated photocatalyst should undergo further characterization and be tested on microorganism

for disinfection. In addition to the disinfection application, the fabricated nanowires should be

investigated for photocatalytic efficiency in air purification and under sunlight.

Finally, Chapter 4 demonstrates the successful immobilization of Ag-ZnO NWs on a

borosilicate glass for successful degradation of phenol, relative to the third goal. From a

preliminary study, an optimal initial concentration (30 mg/L) of phenol was attained. An attempt

to form an overall model for the variation in the phenol degradation rate as a function of UV

light intensity and pH level was made. For constant pH, it was found that the reaction rate is

approximately linear with respect to UV light intensity. For constant UV light intensity, the

reaction rate is approximately cubic in pH. As such, a cubic model equation was derived (see

Table 9) with only linear terms in UV light intensity. The equation was found to fit the data with

a coefficient of determination (R^2) of 0.9934, and 95% confidence intervals were generated for

all model parameters. Additional terms to the model equation were found not to improve the

overall fit to the experimental data. Recommendations for future work include the incorporation of more variables in the overall equation to improve the accuracy of the present model. Also, the applicability of the current model should be examined for visible light irradiation with the fabricated catalyst applied to the disinfection of microorganisms.

REFERENCES

[1]   T. Robinson, G. McMullan, R. Marchant, P. Nigam, Remediation of dyes in textile effluent: a critical review on current treatment technologies with a proposed alternative, Bioresource Technology, 77 (2001) 247-255.

[2]   C. Pearce, J. Lloyd, J. Guthrie, The removal of colour from textile wastewater using whole bacterial cells: a review, Dyes and Pigments, 58 (2003) 179-196.

[3]   A.M. Talarposhti, T. Donnelly, G.K. Anderson, Colour removal from a simulated dye wastewater using a two-phase Anaerobic packed bed reactor, Water Research, 35 (2001) 425-432.

[4]   A. Gorenflo, D. Velazquez-Padron, F. Frimmel, Nanofiltration of a German groundwater of high hardness and NOM content: performance and costs, Desalination, 151 (2003) 253-265.

[5]   S. Ghoreishi, R. Haghighi, Chemical catalytic reaction and biological oxidation for treatment of non-biodegradable textile effluent, Chemical Engineering Journal, 95 (2003) 163-169.

[6]   J. Meier, T. Melin, Wastewater reclamation by the PAC-NF process, Desalination, 178 (2005) 27-40.

[7]   W. Mills, S. Bradford, M. Rigby, M. Wehner, Asano T, Groundwater recharge at the Orange County Water District. Wastewater Reclamation and Reuse, (1998).

[8]   L. Ayed, K. Chaieb, A. Cheref, A. Bakhrouf, Biodegradation of triphenylmethane dye Malachite Green by <i>Sphingomonas paucimobilis</i>, World Journal of Microbiology and Biotechnology, 25 (2009) 705-711.

[9]   P. Borker, A. Salker, Photocatalytic degradation of textile azo dye over $Ce_{1-x}Sn_xO_2$ series, Materials Science and Engineering: B, 133 (2006) 55-60.

[10]   A. Sapkota, A.J. Anceno, S. Baruah, O.V. Shipin, J. Dutta, Zinc oxide nanorod mediated visible light photoinactivation of model microbes in water, Nanotechnology, 22 (2011) 215703.

[11]   H.M. Coleman, B.R. Eggins, J.A. Byrne, F.L. Palmer, E. King, Photocatalytic degradation of 17-β-oestradiol on immobilised TiO_2, Applied Catalysis B: Environmental, 24 (2000) L1-L5.

[12]   C.-S. Hong, Y. Wang, B. Bush, Kinetics and products of the TiO_2, photocatalytic degradation of 2-chlorobiphenyl in water, Chemosphere, 36 (1998) 1653-1667.

[13]   Y. Ohko, I. Ando, C. Niwa, T. Tatsuma, T. Yamamura, T. Nakashima, Y. Kubota, A. Fujishima, Degradation of bisphenol A in water by TiO2 photocatalyst, Environmental Science & Technology, 35 (2001) 2365-2368.

[14]   H.-W. Wang, C.-F. Ting, M.-K. Hung, C.-H. Chiou, Y.-L. Liu, Z. Liu, K.R. Ratinac, S.P. Ringer, Three-dimensional electrodes for dye-sensitized solar cells: synthesis of indium–tin-oxide nanowire arrays and ITO/TiO2 core–shell nanowire arrays by electrophoretic deposition, Nanotechnology, 20 (2009) 055601.

[15]   I.K. Konstantinou, T.A. Albanis, TiO_2-assisted photocatalytic degradation of azo dyes in aqueous solution: kinetic and mechanistic investigations: A review, Applied Catalysis B: Environmental, 49 (2004) 1-14.

[16]   N. Allen, Color Chemistry: Synthesis, Properties and Applications of Organic Dyes and Pigments (2nd Edition) : By H. Zollinger, published by VCH, Cambridge, ISBN 3-527-28352-8, £84.00 (Sterling), Journal of Photochemistry and Photobiology A: Chemistry, 67 (1992) 385-386.

[17]   U. Akpan, B. Hameed, Parameters affecting the photocatalytic degradation of dyes using TiO_2-based photocatalysts: A review, Journal of Hazardous Materials, 170 (2009) 520-529.

[18]   B.R. Bradley, G.T. Daigger, R. Rubin, G. Tchobanoglous, Evaluation of onsite wastewater treatment technologies using sustainable development criteria, Clean Technologies and Environmental Policy, 4 (2002) 87-99.

[19]   W. Ahmed, R. Neller, M. Katouli, Evidence of septic system failure determined by a bacterial biochemical fingerprinting method, Journal of Applied Microbiology, 98 (2005) 910-920.

[20]   S. Carroll, A. Goonetilleke, E. Thomas, M. Hargreaves, R. Frost, L. Dawes, Integrated Risk Framework for Onsite Wastewater Treatment Systems, Environmental Management, 38 (2006) 286-303.

[21]   P. Padmanabhan, K. Sreekumar, T. Thiyagarajan, R. Satpute, K. Bhanumurthy, P. Sengupta, G. Dey, K. Warrier, Nano-crystalline titanium dioxide formed by reactive plasma synthesis, Vacuum, 80 (2006) 1252-1255.

[22]   U.I. Gaya, A.H. Abdullah, Heterogeneous photocatalytic degradation of organic contaminants over titanium dioxide: a review of fundamentals, progress and problems, Journal of Photochemistry and Photobiology C: Photochemistry Reviews, 9 (2008) 1-12.

[23]   S.J. Ergas, B.M. Therriault, D.A. Reckhow, Evaluation of water reuse technologies for the textile industry, Journal of Environmental engineering, 132 (2006) 315-323.

[24]   Z. He, C. Sun, S. Yang, Y. Ding, H. He, Z. Wang, Photocatalytic degradation of rhodamine B by Bi_2WO_6 with electron accepting agent under microwave irradiation: Mechanism and pathway, Journal of Hazardous Materials, 162 (2009) 1477-1486.

[25]   H. Li, H. Li, W.-L. Dai, W. Wang, Z. Fang, J.-F. Deng, XPS studies on surface electronic characteristics of Ni–B and Ni–P amorphous alloy and its correlation to their catalytic properties, Applied Surface Science, 152 (1999) 25-34.

[26]   I. Arslan, I.A. Balcioglu, T. Tuhkanen, Advanced oxidation of synthetic dyehouse effluent by O3, H2O2/O3 and H2O2/UV processes, Environmental Technology, 20 (1999) 921-931.

[27]   E. Forgacs, T. Cserhati, G. Oros, Removal of synthetic dyes from wastewaters: a review, Environment international, 30 (2004) 953-971.

[28]   P. Schröder, J. Navarro-Aviñó, H. Azaizeh, A. Goldhirsh, S. DiGregorio, T. Komives, G. Langergraber, A. Lenz, E. Maestri, A. Memon, A. Ranalli, L. Sebastiani, S. Smrcek, T. Vanek, S. Vuilleumier, F. Wissing, Using phytoremediation technologies to upgrade waste water treatment in Europe, Environmental Science and Pollution Research, 14 (2007) 490-497.

[29]   J. Radjenović, M. Petrović, F. Ventura, D. Barceló, Rejection of pharmaceuticals in nanofiltration and reverse osmosis membrane drinking water treatment, Water Research, 42 (2008) 3601-3610.

[30]   N.N. Mahamuni, Y.G. Adewuyi, Advanced oxidation processes (AOPs) involving ultrasound for waste water treatment: a review with emphasis on cost estimation, Ultrasonics Sonochemistry, 17 (2010) 990-1003.

[31]   J. De Koning, D. Bixio, A. Karabelas, M. Salgot, A. Schaefer, J. De Koning, D. Bixio, A. Karabelas, M. Salgot, A. Schaefer, Characterisation and assessment of water treatment technologies for reuse, Desalination, 218 (2008) 92-104.

[32]   F.L. Rosario-Ortiz, E.C. Wert, S.A. Snyder, Evaluation of UV/H2O2 treatment for the oxidation of pharmaceuticals in wastewater, Water Research, 44 (2010) 1440-1448.

[33]   S. Sanches, M.T. Barreto Crespo, V.J. Pereira, Drinking water treatment of priority pesticides using low pressure UV photolysis and advanced oxidation processes, Water Research, 44 (2010) 1809-1818.

[34]   S. Esplugas, J. Gimenez, S. Contreras, E. Pascual, M. Rodríguez, Comparison of different advanced oxidation processes for phenol degradation, Water Research, 36 (2002) 1034-1042.

[35]   S.S. Srinivasan, J. Wade, E.K. Stefanakos, Synthesis and characterization of photocatalytic TiO 2-ZnFe 2 O 4 nanoparticles, Journal of Nanomaterials, 2006 (2006).

[36]   H. Zhang, X. Lv, Y. Li, Y. Wang, J. Li, P25-Graphene Composite as a High Performance Photocatalyst, ACS Nano, 4 (2009) 380-386.

[37]   D.Y. Goswami, Decontamination of ventilation systems using photocatalytic air cleaning technology, Journal of solar energy engineering, 125 (2003) 359-365.

[38]   A. Vohra, D. Goswami, D. Deshpande, S. Block, Enhanced photocatalytic inactivation of bacterial spores on surfaces in air, Journal of Industrial Microbiology and Biotechnology, 32 (2005) 364-370.

[39]   S. Srinivasan, D. Escobar, Y. Goswami, E. Stefanakos, Effects of catalysts doping on the thermal decomposition behavior of Zn (BH$_4$)$_2$, International Journal of Hydrogen Energy, 33 (2008) 2268-2272.

[40] S. Vijayaraghavan, D. Goswami, Photocatalytic oxidation of toluene in water from an algae pond with high dissolved oxygen content, in: ASME Solar 2002: International Solar Energy Conference, American Society of Mechanical Engineers, 2002, pp. 261-267.

[41] R.M. Alberici, W.F. Jardim, Photocatalytic destruction of VOCs in the gas-phase using titanium dioxide, Applied Catalysis B: Environmental, 14 (1997) 55-68.

[42] D.Y. Goswami, D.M. Trivedi, S. Block, Photocatalytic disinfection of indoor air, Journal of solar energy engineering, 119 (1997) 92-96.

[43] S. Baruah, M.A. Mahmood, M.T.Z. Myint, T. Bora, J. Dutta, Enhanced visible light photocatalysis through fast crystallization of zinc oxide nanorods, Beilstein journal of nanotechnology, 1 (2010) 14-20.

[44] S. Rehman, R. Ullah, A. Butt, N. Gohar, Strategies of making TiO_2 and ZnO visible light active, Journal of Hazardous Materials, 170 (2009) 560-569.

[45] T. Essam, M. Aly Amin, O. El Tayeb, B. Mattiasson, B. Guieysse, Solar-based detoxification of phenol and p-nitrophenol by sequential TiO2 photocatalysis and photosynthetically aerated biological treatment, Water Research, 41 (2007) 1697-1704.

[46] M. Goel, J.-M. Chovelon, C. Ferronato, R. Bayard, T.R. Sreekrishnan, The remediation of wastewater containing 4-chlorophenol using integrated photocatalytic and biological treatment, Journal of Photochemistry and Photobiology B: Biology, 98 (2010) 1-6.

[47] A.M. Pedroza, R. Mosqueda, N. Alonso-Vante, R. Rodríguez-Vázquez, Sequential treatment via Trametes versicolor and UV/TiO2/RuxSey to reduce contaminants in waste water resulting from the bleaching process during paper production, Chemosphere, 67 (2007) 793-801.

[48] P.A. Pekakis, N.P. Xekoukoulotakis, D. Mantzavinos, Treatment of textile dyehouse wastewater by TiO2 photocatalysis, Water Research, 40 (2006) 1276-1286.

[49] L. Yang, L.E. Yu, M.B. Ray, Degradation of paracetamol in aqueous solutions by TiO2 photocatalysis, Water Research, 42 (2008) 3480-3488.

[50] B. Ohtani, O. Prieto-Mahaney, D. Li, R. Abe, What is Degussa (Evonik) P25? Crystalline composition analysis, reconstruction from isolated pure particles and photocatalytic activity test, Journal of Photochemistry and Photobiology A: Chemistry, 216 (2010) 179-182.

[51] K.E. Rajashekhar, L.G. Devi, Polymorphic phase transformation of Degussa P25 TiO_2 by the chelation of diaminopyridine on TiO_6^{2-} octahedron: Correlation of anatase to rutile phase ratio on the photocatalytic activity, Journal of Molecular Catalysis A: Chemical, 374 (2013) 12-21.

[52] S. Ahmed, M.G. Rasul, W.N. Martens, R. Brown, M.A. Hashib, Heterogeneous photocatalytic degradation of phenols in wastewater: A review on current status and developments, Desalination, 261 (2010) 3-18.

[53] C. Shifu, C. Lei, G. Shen, C. Gengyu, The preparation of coupled WO_3/TiO_2 photocatalyst by ball milling, Powder technology, 160 (2005) 198-202.

[54]   M. Dhayal, S. Sharma, C. Kant, K. Saini, S. Jain, Role of Ni doping in surface carbon removal and photo catalytic activity of nano-structured TiO_2 film, Surface Science, 602 (2008) 1149-1154.

[55]   M.B. Fisher, D.A. Keane, P. Fernández-Ibáñez, J. Colreavy, S.J. Hinder, K.G. McGuigan, S.C. Pillai, Nitrogen and copper doped solar light active TiO_2 photocatalysts for water decontamination, Applied Catalysis B: Environmental, 130 (2013) 8-13.

[56] N. Guettai, H. Ait Amar, Photocatalytic oxidation of methyl orange in presence of titanium dioxide in aqueous suspension. Part I: Parametric study, Desalination, 185 (2005) 427-437.

[57] T. Ohno, M. Akiyoshi, T. Umebayashi, K. Asai, T. Mitsui, M. Matsumura, Preparation of S-doped TiO_2 photocatalysts and their photocatalytic activities under visible light, Applied Catalysis A: General, 265 (2004) 115-121.

[58] H. Zhang, J.F. Banfield, Understanding polymorphic phase transformation behavior during growth of nanocrystalline aggregates: insights from TiO2, The Journal of Physical Chemistry B, 104 (2000) 3481-3487.

[59] K. Lv, H. Zuo, J. Sun, K. Deng, S. Liu, X. Li, D. Wang, (Bi, C and N) codoped TiO2 nanoparticles, Journal of Hazardous Materials, 161 (2009) 396-401.

[60] L.M. Kukreja, S. Barik, P. Misra, Variable band gap ZnO nanostructures grown by pulsed laser deposition, Journal of crystal growth, 268 (2004) 531-535.

[61] J. Zhang, C. Pan, P. Fang, J. Wei, R. Xiong, Mo+ C Codoped TiO2 using thermal oxidation for enhancing photocatalytic activity, ACS Applied Materials & Interfaces, 2 (2010) 1173-1176.

[62]   J. Cui, Zinc oxide nanowires, Materials Characterization, 64 (2012) 43-52.

[63] M. Ladanov, M.K. Ram, G. Matthews, A. Kumar, Structure and opto-electrochemical properties of ZnO nanowires grown on n-Si substrate, Langmuir, 27 (2011) 9012-9017.

[64] B.B. Sapkota, S.R. Mishra, Preparation and Photocatalytic Activity Study of p-CuO/n-ZnO composites, in: MRS Proceedings, Cambridge Univ Press, 2012, pp. mrss12-1443-r1406-1403.

[65] A.M. Ali, E.A. Emanuelsson, D.A. Patterson, Photocatalysis with nanostructured zinc oxide thin films: The relationship between morphology and photocatalytic activity under oxygen limited and oxygen rich conditions and evidence for a Mars Van Krevelen mechanism, Applied Catalysis B: Environmental, 97 (2010) 168-181.

[66]   S.K. Pardeshi, A.B. Patil, Effect of morphology and crystallite size on solar photocatalytic activity of zinc oxide synthesized by solution free mechanochemical method, Journal of Molecular Catalysis A: Chemical, 308 (2009) 32-40.

[67]   M. Qamar, M. Muneer, A comparative photocatalytic activity of titanium dioxide and zinc oxide by investigating the degradation of vanillin, Desalination, 249 (2009) 535-540.

[68]   I. Poulios, D. Makri, X. Prohaska, Photocatalytic treatment of olive milling waste water: oxidation of protocatechuic acid, Global Nest: Int. J, 1 (1999) 55-62.

[69]   E.R. Carraway, A.J. Hoffman, M.R. Hoffmann, Photocatalytic oxidation of organic acids on quantum-sized semiconductor colloids, Environmental Science & Technology, 28 (1994) 786-793.

[70]   L. Wang, X. Zhang, S. Zhao, G. Zhou, Y. Zhou, J. Qi, Synthesis of well-aligned ZnO nanowires by simple physical vapor deposition on c-oriented ZnO thin films without catalysts or additives, Applied Physics Letters, 86 (2005) 024108-024108-024103.

[71]   O. Dulub, L.A. Boatner, U. Diebold, STM study of the geometric and electronic structure of ZnO(0 0 0 1)-Zn, (0 0 0 1̄)-O, (1 0 1̄ 0), and (1 1 2̄ 0) surfaces, Surface Science, 519 (2002) 201-217.

[72]   B. Meyer, D. Marx, Density-functional study of the structure and stability of ZnO surfaces, Physical Review B, 67 (2003) 035403.

[73]   G.L. Hornyak, J. Dutta, H. Tibbals, A. Rao, Introduction to nanoscience, CRC Press UK, 2008.

[74]   Z.L. Wang, Zinc oxide nanostructures: growth, properties and applications, Journal of Physics: Condensed Matter, 16 (2004) R829.

[75]   O.K. Dalrymple, D.H. Yeh, M.A. Trotz, Removing pharmaceuticals and endocrine-disrupting compounds from wastewater by photocatalysis, Journal of Chemical Technology & Biotechnology, 82 (2007) 121-134.

[76]   S. Linic, P. Christopher, D.B. Ingram, Plasmonic-metal nanostructures for efficient conversion of solar to chemical energy, Nat Mater, 10 (2011) 911-921.

[77]   D.S. Bhatkhande, V.G. Pangarkar, A.A.C.M. Beenackers, Photocatalytic degradation for environmental applications – a review, Journal of Chemical Technology & Biotechnology, 77 (2002) 102-116.

[78]   D.M. Fouad, M.B. Mohamed, Comparative study of the photocatalytic activity of semiconductor nanostructures and their hybrid metal nanocomposites on the photodegradation of malathion, Journal of Nanomaterials, 2012 (2012) 2.

[79]   B. Neppolian, S. Sakthivel, B. Arabindoo, M. Palanichamy, V. Murugesan, Degradation of textile dye by solar light using TiO2 and ZnO photocatalysts, Journal of Environmental Science and Health, Part A, 34 (1999) 1829-1838.

[80]   A.A. Khodja, T. Sehili, J.-F. Pilichowski, P. Boule, Photocatalytic degradation of 2-phenylphenol on TiO$_2$ and ZnO in aqueous suspensions, Journal of Photochemistry and Photobiology A: Chemistry, 141 (2001) 231-239.

[81]   G. Marci, V. Augugliaro, M.J. Lopez-Munoz, C. Martin, L. Palmisano, V. Rives, M. Schiavello, R.J. Tilley, A.M. Venezia, Preparation characterization and photocatalytic activity of polycrystalline ZnO/TiO2 systems. 2. Surface, bulk characterization, and 4-nitrophenol photodegradation in liquid-solid regime, The Journal of Physical Chemistry B, 105 (2001) 1033-1040.

[82]   N. Sobana, M. Swaminathan, The effect of operational parameters on the photocatalytic degradation of acid red 18 by ZnO, Separation and Purification Technology, 56 (2007) 101-107.

[83]   Q. Wan, T. Wang, J. Zhao, Enhanced photocatalytic activity of ZnO nanotetrapods, Applied Physics Letters, 87 (2005) 083105-083105-083103.

[84]   N.V. Kaneva, D.T. Dimitrov, C.D. Dushkin, Effect of nickel doping on the photocatalytic activity of ZnO thin films under UV and visible light, Applied Surface Science, 257 (2011) 8113-8120.

[85]   E. Evgenidou, K. Fytianos, I. Poulios, Semiconductor-sensitized photodegradation of dichlorvos in water using TiO2 and ZnO as catalysts, Applied Catalysis B: Environmental, 59 (2005) 81-89.

[86]   D. Lin, H. Wu, R. Zhang, W. Pan, Enhanced Photocatalysis of Electrospun Ag−ZnO Heterostructured Nanofibers, Chemistry of Materials, 21 (2009) 3479-3484.

[87]   C. Ma, Z. Zhou, H. Wei, Z. Yang, Z. Wang, Y. Zhang, Rapid large-scale preparation of ZnO nanowires for photocatalytic application, Nanoscale research letters, 6 (2011) 1-5.

[88]   S. Baruah, R.F. Rafique, J. Dutta, Visible light photocatalysis by tailoring crystal defects in zinc oxide nanostructures, Nano, 3 (2008) 399-407.

[89]   Y. Zhang, M.K. Ram, E.K. Stefanakos, D.Y. Goswami, Synthesis, Characterization, and Applications of ZnO Nanowires, Journal of Nanomaterials, 2012 (2012) 22.

[90]   E.W. Petersen, E.M. Likovich, K.J. Russell, V. Narayanamurti, Growth of ZnO nanowires catalyzed by size-dependent melting of Au nanoparticles, Nanotechnology, 20 (2009) 405603.

[91]   L.N. Protasova, E.V. Rebrov, T.S. Glazneva, A. Berenguer-Murcia, Z.R. Ismagilov, J.C. Schouten, Control of the thickness of mesoporous titania films for application in multiphase catalytic microreactors, Journal of Catalysis, 271 (2010) 161-169.

[92]   S. Ashraf, A.C. Jones, J. Bacsa, A. Steiner, P.R. Chalker, P. Beahan, S. Hindley, R. Odedra, P.A. Williams, P.N. Heys, MOCVD of Vertically Aligned ZnO Nanowires Using Bidentate Ether Adducts of Dimethylzinc, Chemical Vapor Deposition, 17 (2011) 45-53.

[93]   S.C. Lyu, Y. Zhang, C.J. Lee, H. Ruh, H.J. Lee, Low-temperature growth of ZnO nanowire array by a simple physical vapor-deposition method, Chemistry of Materials, 15 (2003) 3294-3299.

[94]   J. Wang, C. Yang, P. Chen, C. Su, W. Chen, K. Chiu, W. Chou, Catalyst-free highly vertically aligned ZnO nanoneedle arrays grown by plasma-assisted molecular beam epitaxy, Applied Physics A: Materials Science & Processing, 97 (2009) 553-557.

[95]   Y.W. Heo, D. Norton, L. Tien, Y. Kwon, B. Kang, F. Ren, S. Pearton, J. LaRoche, ZnO nanowire growth and devices, Materials Science and Engineering: R: Reports, 47 (2004) 1-47.

[96]   G.-C. Yi, C. Wang, W.I. Park, ZnO nanorods: synthesis, characterization and applications, Semiconductor Science and Technology, 20 (2005) S22.

[97]   R. Wagner, W. Ellis, Vapor-liquid-solid mechanism of single crystal growth, Applied Physics Letters, 4 (1964) 89-90.

[98]   D.-I. Suh, C.C. Byeon, C.-L. Lee, Synthesis and optical characterization of vertically grown ZnO nanowires in high crystallinity through vapor–liquid–solid growth mechanism, Applied Surface Science, 257 (2010) 1454-1456.

[99]   W. Wang, Song, P. Li, J.H. Ryou, R.D. Dupuis, C.J. Summers, Z.L. Wang, Growth of Uniformly Aligned ZnO Nanowire Heterojunction Arrays on GaN, AlN, and Al0.5Ga0.5N Substrates, Journal of the American Chemical Society, 127 (2005) 7920-7923.

[100]   W. Wang, J. Song, C.J. Summers, J.H. Ryou, P. Li, R.D. Dupuis, Z.L. Wang, Density-Controlled Growth of Aligned ZnO Nanowires Sharing a Common Contact: A Simple, Low-Cost, and Mask-Free Technique for Large-Scale Applications, The Journal of Physical Chemistry B, 110 (2006) 7720-7724.

[101]   X. Wang, X. Wang, J. Song, C.J. Summers, J.H. Ryou, P. Li, R.D. Dupuis, Z.L. Wang, Density-controlled growth of aligned ZnO nanowires sharing a common contact: a simple, low-cost, and mask-free technique for large-scale applications, The Journal of Physical Chemistry B, 110 (2006) 7720-7724.

[102]   F.-H. Chu, C.-W. Huang, C.-L. Hsin, C.-W. Wang, S.-Y. Yu, P.-H. Yeh, W.-W. Wu, Well-aligned ZnO nanowires with excellent field emission and photocatalytic properties, Nanoscale, 4 (2012) 1471-1475.

[103]   Y.-J. Zeng, Z.-Z. Ye, W.-Z. Xu, L.-P. Zhu, B.-H. Zhao, Well-aligned ZnO nanowires grown on Si substrate via metal–organic chemical vapor deposition, Applied Surface Science, 250 (2005) 280-283.

[104]   O. Tigli, J. Juhala, ZnO nanowire growth by physical vapor deposition, in: Nanotechnology (IEEE-NANO), 2011 11th IEEE Conference on, IEEE, 2011, pp. 608-611.

[105]   B. Zhang, S. Zhou, B. Liu, H. Gong, X. Zhang, Fabrication and green emission of ZnO nanowire arrays, Science in China Series E: Technological Sciences, 52 (2009) 883-887.

[106]   S.K. Kim, H. Chang, K. Cho, D.S. Kil, S.W. Cho, H.D. Jang, J.-W. Choi, J. Choi, Enhanced photocatalytic property of nanoporous TiO$_2$/SiO$_2$ micro-particles prepared by aerosol assisted co-assembly of nanoparticles, Materials Letters, 65 (2011) 3330-3332.

[107]   J. Song, S. Baek, H. Lee, S. Lim, Selective Growth of Vertical ZnO Nanowires with the Control of Hydrothermal Synthesis and Nano-Imprint Technology, Journal of nanoscience and nanotechnology, 9 (2009) 3909-3913.

[108] V. Zalamai, V. Ursaki, E. Rusu, P. Arabadji, I. Tiginyanu, L. Sirbu, Photoluminescence and resonant Raman scattering in highly conductive ZnO layers, Applied Physics Letters, 84 (2004) 5168-5170.

[109] S. Baruah, J. Dutta, Hydrothermal growth of ZnO nanostructures, Science and Technology of Advanced Materials, 10 (2009) 013001.

[110] J.D. Prades, A. Cirera, J.R. Morante, Ab initio calculations of NO2 and SO2 chemisorption onto non-polar ZnO surfaces, Sensors and Actuators B: Chemical, 142 (2009) 179-184.

[111] T.-K. Huang, T.-H. Cheng, M.-Y. Yen, W.-H. Hsiao, L.-S. Wang, F.-R. Chen, J.-J. Kai, C.-Y. Lee, H.-T. Chiu, Growth of Cu Nanobelt and Ag Belt-Like Materials by Surfactant-Assisted Galvanic Reductions, Langmuir, 23 (2007) 5722-5726.

[112] L. Demianets, D. Kostomarov, I. Kuz'mina, S. Pushko, Mechanism of growth of ZnO single crystals from hydrothermal alkali solutions, Crystallography Reports, 47 (2002) S86-S98.

[113] R. Viswanatha, H. Amenitsch, D. Sarma, Growth kinetics of ZnO nanocrystals: a few surprises, Journal of the American Chemical Society, 129 (2007) 4470-4475.

[114] L.N. Demianets, D.V. Kostomarov, Mechanism of zinc oxide single crystal growth under hydrothermal conditions, in: Annales de Chimie Science des Matériaux, Elsevier, 2001, pp. 193-198.

[115] L. Demyanets, N. Sizova, L. Li, Zinc oxide single crystals: Influence of temperature and orientation of crystals on their mechanical properties, Crystallography Reports, 50 (2005) 646-653.

[116] M.N. Ashfold, R.P. Doherty, N.G. Ndifor-Angwafor, D.J. Riley, Y. Sun, The kinetics of the hydrothermal growth of ZnO nanostructures, Thin Solid Films, 515 (2007) 8679-8683.

[117] H.E. Unalan, P. Hiralal, N. Rupesinghe, S. Dalal, W.I. Milne, G.A. Amaratunga, Rapid synthesis of aligned zinc oxide nanowires, Nanotechnology, 19 (2008) 255608.

[118] S.H. Jung, E. Oh, K.H. Lee, W. Park, S.H. Jeong, A sonochemical method for fabricating aligned ZnO nanorods, Advanced Materials, 19 (2007) 749-753.

[119] Q. Tang, W. Zhou, J. Shen, W. Zhang, L. Kong, Y. Qian, A template-free aqueous route to ZnO nanorod arrays with high optical property, Chemical Communications, (2004) 712-713.

[120] D.S. Boyle, K. Govender, P. O'Brien, Novel low temperature solution deposition of perpendicularly orientated rods of ZnO: substrate effects and evidence of the importance of counter-ions in the control of crystallite growth, Chemical Communications, (2002) 80-81.

[121] L. Vayssieres, N. Beermann, S.-E. Lindquist, A. Hagfeldt, Controlled aqueous chemical growth of oriented three-dimensional crystalline nanorod arrays: application to iron (III) oxides, Chemistry of Materials, 13 (2001) 233-235.

[122] B. Cheng, E.T. Samulski, Hydrothermal synthesis of one-dimensional ZnO nanostructures with different aspect ratios, Chemical Communications, (2004) 986-987.

[123] B. Liu, H.C. Zeng, Hydrothermal synthesis of ZnO nanorods in the diameter regime of 50 nm, Journal of the American Chemical Society, 125 (2003) 4430-4431.

[124] H. Cao, X. Qian, Q. Gong, W. Du, X. Ma, Z. Zhu, Shape-and size-controlled synthesis of nanometre ZnO from a simple solution route at room temperature, Nanotechnology, 17 (2006) 3632.

[125] X. Hou, F. Zhou, Y. Sun, W. Liu, Ultrasound-assisted synthesis of dentritic ZnO nanostructure in ionic liquid, Materials Letters, 61 (2007) 1789-1792.

[126] T. Alammar, A.-V. Mudring, Facile ultrasound-assisted synthesis of ZnO nanorods in an ionic liquid, Materials Letters, 63 (2009) 732-735.

[127] C. Cheng, B. Yan, S.M. Wong, X. Li, W. Zhou, T. Yu, Z. Shen, H. Yu, H.J. Fan, Fabrication and SERS performance of silver-nanoparticle-decorated Si/ZnO nanotrees in ordered arrays, ACS Applied Materials & Interfaces, 2 (2010) 1824-1828.

[128] L.E. Greene, M. Law, J. Goldberger, F. Kim, J.C. Johnson, Y. Zhang, R.J. Saykally, P. Yang, Low-Temperature Wafer-Scale Production of ZnO Nanowire Arrays, Angewandte Chemie International Edition, 42 (2003) 3031-3034.

[129] T.-Y. Liu, H.-C. Liao, C.-C. Lin, S.-H. Hu, S.-Y. Chen, Biofunctional ZnO nanorod arrays grown on flexible substrates, Langmuir, 22 (2006) 5804-5809.

[130] A. Manekkathodi, M.Y. Lu, C.W. Wang, L.J. Chen, Direct Growth of Aligned Zinc Oxide Nanorods on Paper Substrates for Low-Cost Flexible Electronics, Advanced Materials, 22 (2010) 4059-4063.

[131] Y. Qin, X. Wang, Z.L. Wang, Microfibre–nanowire hybrid structure for energy scavenging, Nature, 451 (2008) 809-813.

[132] J. Bae, M.K. Song, Y.J. Park, J.M. Kim, M. Liu, Z.L. Wang, Fiber Supercapacitors Made of Nanowire-Fiber Hybrid Structures for Wearable/Flexible Energy Storage, Angewandte Chemie International Edition, 50 (2011) 1683-1687.

[133] J.-S. Na, B. Gong, G. Scarel, G.N. Parsons, Surface polarity shielding and hierarchical ZnO nano-architectures produced using sequential hydrothermal crystal synthesis and thin film atomic layer deposition, ACS Nano, 3 (2009) 3191-3199.

[134] B. Kang, S. Pearton, F. Ren, Low temperature (< 100 C) patterned growth of ZnO nanorod arrays on Si, Applied Physics Letters, 90 (2007) 083104.

[135] L.E. Greene, M. Law, D.H. Tan, M. Montano, J. Goldberger, G. Somorjai, P. Yang, General Route to Vertical ZnO Nanowire Arrays Using Textured ZnO Seeds, Nano Letters, 5 (2005) 1231-1236.

[136] M. Yin, Y. Gu, I.L. Kuskovsky, T. Andelman, Y. Zhu, G. Neumark, S. O'Brien, Zinc oxide quantum rods, Journal of the American Chemical Society, 126 (2004) 6206-6207.

[137] Y. Tak, K. Yong, Controlled growth of well-aligned ZnO nanorod array using a novel solution method, The Journal of Physical Chemistry B, 109 (2005) 19263-19269.

[138]   Y. Fang, Q. Pang, X. Wen, J. Wang, S. Yang, Synthesis of ultrathin ZnO nanofibers aligned on a zinc substrate, Small, 2 (2006) 612-615.

[139]   H. Ghayour, H. Rezaie, S. Mirdamadi, A. Nourbakhsh, The effect of seed layer thickness on alignment and morphology of ZnO nanorods, Vacuum, 86 (2011) 101-105.

[140]   L.-W. Ji, S.-M. Peng, J.-S. Wu, W.-S. Shih, C.-Z. Wu, I. Tang, Effect of seed layer on the growth of well-aligned ZnO nanowires, Journal of Physics and Chemistry of Solids, 70 (2009) 1359-1362.

[141]   J. Liu, J. She, S. Deng, J. Chen, N. Xu, Ultrathin Seed-Layer for Tuning Density of ZnO Nanowire Arrays and Their Field Emission Characteristics, The Journal of Physical Chemistry C, 112 (2008) 11685-11690.

[142]   F. Solís-Pomar, E. Martínez, M. Meléndrez, E. Pérez-Tijerina, Growth of vertically aligned ZnO nanorods using textured ZnO films, Nanoscale Research Letters, 6 (2011) 1-11.

[143]   J.-H. Tian, J. Hu, S.-S. Li, F. Zhang, J. Liu, J. Shi, X. Li, Z.-Q. Tian, Y. Chen, Improved seedless hydrothermal synthesis of dense and ultralong ZnO nanowires, Nanotechnology, 22 (2011) 245601.

[144]   W. Baiqi, S. Xudong, F. Qiang, J. Iqbal, L. Yan, F. Honggang, Y. Dapeng, Photoluminescence properties of Co-doped ZnO nanorods array fabricated by the solution method, Physica E Low Dimens Syst Nanostruct, 41 (2009) 5-5.

[145]   D. Li, L. Zhao, R. Wu, C. Ronning, J.G. Lu, Temperature-dependent photoconductance of heavily doped ZnO nanowires, Nano Research, 4 (2011) 1110-1116.

[146]   D. Wang, G. Xing, M. Gao, L. Yang, J. Yang, T. Wu, Defects-mediated energy transfer in red-light-emitting Eu-doped ZnO nanowire arrays, The Journal of Physical Chemistry C, 115 (2011) 22729-22735.

[147]   K.-P. Kim, D. Chang, S.K. Lim, S.-K. Lee, H.-K. Lyu, D.-K. Hwang, Thermal annealing effects on the dynamic photoresponse properties of Al-doped ZnO nanowires network, Current Applied Physics, 11 (2011) 1311-1314.

[148]   T. Kataoka, Y. Yamazaki, V. Singh, A. Fujimori, F.-H. Chang, H.-J. Lin, D. Huang, C. Chen, G. Xing, J. Seo, Ferromagnetic interaction between Cu ions in the bulk region of Cu-doped ZnO nanowires, Physical Review B, 84 (2011) 153203.

[149]   Z. Zhang†, R. Zou†, L. Yu, J. Hu, Recent research on one-dimensional silicon-based semiconductor nanomaterials: synthesis, structures, properties and applications, Critical Reviews in Solid State and Materials Sciences, 36 (2011) 148-173.

[150]   Z. Dai, A. Nurbawono, A. Zhang, M. Zhou, Y.P. Feng, G.W. Ho, C. Zhang, C-doped ZnO nanowires: Electronic structures, magnetic properties, and a possible spintronic device, The Journal of chemical physics, 134 (2011) 104706.

[151]   H. Xu, A. Rosa, T. Frauenheim, R. Zhang, N-doped ZnO nanowires: Surface segregation, the effect of hydrogen passivation and applications in spintronics, physica status solidi (b), 247 (2010) 2195-2201.

[152] J. Gao, Q. Zhao, Y. Sun, G. Li, J. Zhang, D. Yu, A novel way for synthesizing phosphorus-doped ZnO nanowires, Nanoscale Research Letters, 6 (2011) 1-6.

[153] J. Fan, A. Shavel, R. Zamani, C. Fábrega, J. Rousset, S. Haller, F. Gueell, A. Carrete, T. Andreu, J. Arbiol, Control of the doping concentration, morphology and optoelectronic properties of vertically aligned chlorine-doped ZnO nanowires, Acta Materialia, 59 (2011) 6790-6800.

[154] S.-M. Zhou, X.-H. Zhang, X.-M. Meng, K. Zou, X. Fan, S.-K. Wu, S.-T. Lee, The fabrication and optical properties of highly crystalline ultra-long Cu-doped ZnO nanowires, Nanotechnology, 15 (2004) 1152.

[155] D. Li, Z.T. Liu, Y.H. Leung, A.B. Djurišić, M.H. Xie, W.K. Chan, Transition metal-doped ZnO nanorods synthesized by chemical methods, Journal of Physics and Chemistry of Solids, 69 (2008) 616-619.

[156] C. Gu, C. Cheng, H. Huang, T. Wong, N. Wang, T.-Y. Zhang, Growth and photocatalytic activity of dendrite-like ZnO@ Ag heterostructure nanocrystals, Crystal Growth and Design, 9 (2009) 3278-3285.

[157] X. Wang, H. Zhu, Y. Xu, H. Wang, Y. Tao, S. Hark, X. Xiao, Q. Li, Aligned ZnO/CdTe core− shell nanocable arrays on indium tin oxide: synthesis and photoelectrochemical properties, ACS Nano, 4 (2010) 3302-3308.

[158] O. Lupan, V. Guérin, I. Tiginyanu, V. Ursaki, L. Chow, H. Heinrich, T. Pauporté, Well-aligned arrays of vertically oriented ZnO nanowires electrodeposited on ITO-coated glass and their integration in dye sensitized solar cells, Journal of Photochemistry and Photobiology A: Chemistry, 211 (2010) 65-73.

[159] X. Zhao, B. Zhang, K. Ai, G. Zhang, L. Cao, X. Liu, H. Sun, H. Wang, L. Lu, Monitoring catalytic degradation of dye molecules on silver-coated ZnO nanowire arrays by surface-enhanced Raman spectroscopy, Journal of Materials Chemistry, 19 (2009) 5547-5553.

[160] S. Baruah, M. Jaisai, R. Imani, M.M. Nazhad, J. Dutta, Photocatalytic paper using zinc oxide nanorods, Science and Technology of Advanced Materials, 11 (2010) 055002.

[161] O. Lupan, T. Pauporté, L. Chow, B. Viana, F. Pellé, L. Ono, B. Roldan Cuenya, H. Heinrich, Effects of annealing on properties of ZnO thin films prepared by electrochemical deposition in chloride medium, Applied Surface Science, 256 (2010) 1895-1907.

[162] O. Lupan, V. Ursaki, G. Chai, L. Chow, G. Emelchenko, I. Tiginyanu, A. Gruzintsev, A. Redkin, Selective hydrogen gas nanosensor using individual ZnO nanowire with fast response at room temperature, Sensors and Actuators B: Chemical, 144 (2010) 56-66.

[163] S.N. Das, J.-H. Choi, J.P. Kar, T.I. Lee, J.-M. Myoung, Fabrication of p-type ZnO nanowires based heterojunction diode, Materials Chemistry and Physics, 121 (2010) 472-476.

[164] L. Vayssieres, Growth of arrayed nanorods and nanowires of ZnO from aqueous solutions, Advanced Materials, 15 (2003) 464-466.

[165] T. Pauporté, E. Jouanno, F. Pellé, B. Viana, P. Aschehoug, Key growth parameters for the electrodeposition of ZnO films with an intense UV-light emission at room temperature, The Journal of Physical Chemistry C, 113 (2009) 10422-10431.

[166] A. Sugunan, V.K. Guduru, A. Uheida, M.S. Toprak, M. Muhammed, Radially Oriented ZnO Nanowires on Flexible Poly-l-Lactide Nanofibers for Continuous-Flow Photocatalytic Water Purification, Journal of the American Ceramic Society, 93 (2010) 3740-3744.

[167] X. Li, Y. Cheng, S. Kang, J. Mu, Preparation and enhanced visible light-driven catalytic activity of ZnO microrods sensitized by porphyrin heteroaggregate, Applied Surface Science, 256 (2010) 6705-6709.

[168] H. Liu, J. Yang, J. Liang, Y. Huang, C. Tang, ZnO nanofiber and nanoparticle synthesized through electrospinning and their photocatalytic activity under visible light, Journal of the American Ceramic Society, 91 (2008) 1287-1291.

[169] M. Guo, M. Fung, F. Fang, X. Chen, A. Ng, A. Djurišić, W. Chan, ZnO and TiO$_2$ 1D nanostructures for photocatalytic applications, Journal of Alloys and Compounds, 509 (2011) 1328-1332.

[170] T. Sun, J. Qiu, C. Liang, Controllable fabrication and photocatalytic activity of ZnO nanobelt arrays, The Journal of Physical Chemistry C, 112 (2008) 715-721.

[171] N.F. Hamedani, A.R. Mahjoub, A.A. Khodadadi, Y. Mortazavi, Microwave assisted fast synthesis of various ZnO morphologies for selective detection of CO, CH$_4$ and ethanol, Sensors and Actuators B: Chemical, 156 (2011) 737-742.

[172] R. Mohan, K. Krishnamoorthy, S.-J. Kim, Enhanced photocatalytic activity of Cu-doped ZnO nanorods, Solid State Communications, 152 (2012) 375-380.

[173] P.V. Kamat, Photochemistry on nonreactive and reactive (semiconductor) surfaces, Chemical Reviews, 93 (1993) 267-300.

[174] Z. Deng, M. Chen, G. Gu, L. Wu, A facile method to fabricate ZnO hollow spheres and their photocatalytic property, The Journal of Physical Chemistry B, 112 (2008) 16-22.

[175] T. Melin, R. Rautenbach, Membranverfahren, Springer, 2007.

[176] C. Ma, W. Chu, Photodegradation mechanism and rate improvement of chlorinated aromatic dye in non-ionic surfactant solutions, Water Research, 35 (2001) 2453-2459.

[177] Y. Wong, Y. Szeto, W. Cheung, G. McKay, Equilibrium studies for acid dye adsorption onto chitosan, Langmuir, 19 (2003) 7888-7894.

[178] C. Domınguez, J. Garcıa, M. Pedraz, A. Torres, M. Galan, Photocatalytic oxidation of organic pollutants in water, Catalysis Today, 40 (1998) 85-101.

[179] S.D. Richardson, C.S. Willson, K.A. Rusch, Use of rhodamine water tracer in the marshland upwelling system, Ground water, 42 (2004) 678-688.

[180] A.F. Hepp, M.J. Kulis, B. Ana, R. Zubrin, M. Berggren, J.D. Hensel, M.C. Kimble, Green Aerospace Fuels from Nonpetroleum Sources, National Aeronautics and Space Administration, Glenn Research Center, 2011.

[181]   G. Silversmit, G. De Doncker, R. De Gryse, A mineral TiO2 (001) anatase crystal examined by XPS, Surface Science Spectra, 9 (2002) 21-29.

[182]   J.F. Weaver, G.B. Hoflund, Surface Characterization Study of the Thermal Decomposition of AgO, The Journal of Physical Chemistry, 98 (1994) 8519-8524.

[183]   A. Amri, X. Duan, C.-Y. Yin, Z.-T. Jiang, M.M. Rahman, T. Pryor, Solar absorptance of copper–cobalt oxide thin film coatings with nano-size, grain-like morphology: Optimization and synchrotron radiation XPS studies, Applied Surface Science, 275 (2013) 127-135.

[184]   J.C. Colmenares, A. Magdziarz, M.A. Aramendia, A. Marinas, J.M. Marinas, F.J. Urbano, J.A. Navio, Influence of the strong metal support interaction effect (SMSI) of Pt/TiO2 and Pd/TiO2 systems in the photocatalytic biohydrogen production from glucose solution, Catalysis Communications, 16 (2011) 1-6.

[185]   N. Hamzah, N.M. Nordin, A.H.A. Nadzri, Y.A. Nik, M.B. Kassim, M.A. Yarmo, Enhanced activity of Ru/TiO$_2$ catalyst using bisupport, bentonite-TiO$_2$ for hydrogenolysis of glycerol in aqueous media, Applied Catalysis A: General, 419 (2012) 133-141.

[186]   D.C. Hurum, K.A. Gray, T. Rajh, M.C. Thurnauer, Recombination pathways in the Degussa P25 formulation of TiO2: surface versus lattice mechanisms, The Journal of Physical Chemistry B, 109 (2005) 977-980.

[187]   Z. He, S. Yang, Y. Ju, C. Sun, Microwave photocatalytic degradation of Rhodamine B using TiO$_2$ supported on activated carbon: Mechanism implication, Journal of Environmental Sciences, 21 (2009) 268-272.

[188]   S.-H. Lee, E. Yamasue, K.N. Ishihara, H. Okumura, Photocatalysis and surface doping states of N-doped TiO$_x$ films prepared by reactive sputtering with dry air, Applied Catalysis B: Environmental, 93 (2010) 217-226.

[189]   V. Houšková, V. Štengl, S. Bakardjieva, N. Murafa, V. Tyrpekl, Efficient gas phase photodecomposition of acetone by Ru-doped Titania, Applied Catalysis B: Environmental, 89 (2009) 613-619.

[190]   M. Salehi, H. Hashemipour, M. Mirzaee, Experimental Study of Influencing Factors and Kinetics in Catalytic Removal of Methylene Blue with TiO$_2$ Nanopowder, American Journal of Environmental Engineering, 2 (2012) 1-7.

[191]   P.E. Gordon, A.J. Colozza, A.F. Hepp, R.S. Heller, R. Gustafson, T. Stern, T. Nakamura, Thermal energy for lunar in situ resource utilization: technical challenges and technology opportunities, (2011).

[192]   M. O'Neill, A. McDanal, P. George, M. Piszczor, H. Brandhorst, M. Eskenazi, M. Botke, D. Edwards, Prototype Wing Testing of the Stretched Lens Array (SLA), in: 1st International Energy Conversion Engineering Conference, AIAA, 2003.

[193]   L.H. Levine, J.T. Richards, R. Soler, F. Maxik, J. Coutts, R.M. Wheeler, UV LED as a Light Source for Photocatalytic Oxidation of Trace Organic Contaminants, in: 40th International Conference on Environmental Systems.

[194] N. Kislov, J. Lahiri, H. Verma, D.Y. Goswami, E. Stefanakos, M. Batzill, Photocatalytic degradation of methyl orange over single crystalline ZnO: orientation dependence of photoactivity and photostability of ZnO, Langmuir, 25 (2009) 3310-3315.

[195] I. Udom, M.K. Ram, E.K. Stefanakos, A.F. Hepp, D.Y. Goswami, One dimensional-ZnO nanostructures: Synthesis, properties and environmental applications, Materials Science in Semiconductor Processing, 16 (2013) 2070-2083.

[196] J. Tian, L. Chen, Y. Yin, X. Wang, J. Dai, Z. Zhu, X. Liu, P. Wu, Photocatalyst of TiO< sub> 2</sub>/ZnO nano composite film: Preparation, characterization, and photodegradation activity of methyl orange, Surface and Coatings Technology, 204 (2009) 205-214.

[197] T.-J. Kuo, C.-N. Lin, C.-L. Kuo, M.H. Huang, Growth of ultralong ZnO nanowires on silicon substrates by vapor transport and their use as recyclable photocatalysts, Chemistry of Materials, 19 (2007) 5143-5147.

[198] H. Chen, X. Wu, L. Gong, C. Ye, F. Qu, G. Shen, Hydrothermally grown ZnO micro/nanotube arrays and their properties, Nanoscale Research Letters, 5 (2010) 570-575.

[199] F. Mai, C. Chen, J. Chen, S. Liu, Photodegradation of methyl green using visible irradiation in ZnO suspensions: Determination of the reaction pathway and identification of intermediates by a high-performance liquid chromatography–photodiode array-electrospray ionization-mass spectrometry method, Journal of Chromatography A, 1189 (2008) 355-365.

[200] J. Nayak, S. Sahu, J. Kasuya, S. Nozaki, CdS–ZnO composite nanorods: synthesis, characterization and application for photocatalytic degradation of 3, 4-dihydroxy benzoic acid, Applied Surface Science, 254 (2008) 7215-7218.

[201] Z. Fan, D. Wang, P.-C. Chang, W.-Y. Tseng, J.G. Lu, ZnO nanowire field-effect transistor and oxygen sensing property, Applied Physics Letters, 85 (2004) 5923-5925.

[202] M.H. Huang, Y. Wu, H. Feick, N. Tran, E. Weber, P. Yang, Catalytic growth of zinc oxide nanowires by vapor transport, Advanced Materials, 13 (2001) 113-116.

[203] B. Wang, C. Xia, J. Iqbal, N. Tang, Z. Sun, Y. Lv, L. Wu, Influences of Co doping on the structural, optical and magnetic properties of ZnO nanorods synthesized by hydrothermal route, Solid State Sciences, 11 (2009) 1419-1422.

[204] Z. Li, Q. Zhao, W. Fan, J. Zhan, Porous SnO2 nanospheres as sensitive gas sensors for volatile organic compounds detection, Nanoscale, 3 (2011) 1646-1652.

[205] T. Meron, G. Markovich, Ferromagnetism in colloidal Mn2+-doped ZnO nanocrystals, The Journal of Physical Chemistry B, 109 (2005) 20232-20236.

[206] C. Wu, L. Shen, Y.-C. Zhang, Q. Huang, Solvothermal synthesis of Cr-doped ZnO nanowires with visible light-driven photocatalytic activity, Materials Letters, 65 (2011) 1794-1796.

[207] Y. Lu, Y. Lin, D. Wang, L. Wang, T. Xie, T. Jiang, A high performance cobalt-doped ZnO visible light photocatalyst and its photogenerated charge transfer properties, Nano Research, 4 (2011) 1144-1152.

[208] P. Korake, R. Sridharkrishna, P. Hankare, K. Garadkar, Photocatalytic degradation of phosphamidon using Ag-doped ZnO nanorods, Toxicological & Environmental Chemistry, 94 (2012) 1075-1085.

[209] R.J. Brandi, O.M. Alfano, A.E. Cassano, Modeling of radiation absorption in a flat plate photocatalytic reactor, Chemical Engineering Science, 51 (1996) 3169-3174.

[210] P. Fernández, J. Blanco, C. Sichel, S. Malato, Water disinfection by solar photocatalysis using compound parabolic collectors, Catalysis Today, 101 (2005) 345-352.

[211] J. M Stokke, D.W. Mazyck, C. Wu, R. Sheahan, Photocatalytic oxidation of methanol using silica-titania composites in a packed-bed reactor, Environmental progress, 25 (2006) 312-318.

[212] M. Mehrvar, W.A. Anderson, M. Moo-Young, Preliminary analysis of a tellerette packed-bed photocatalytic reactor, Advances in Environmental Research, 6 (2002) 411-418.

[213] D. Goswami, S. Sharma, G. Mathur, C. Jotshi, Techno-economic analysis of solar detoxification systems, Journal of solar energy engineering, 119 (1997) 108-113.

[214] R.F. Nogueira, W.F. Jardim, TiO$_2$-fixed-bed reactor for water decontamination using solar light, Solar energy, 56 (1996) 471-477.

[215] Y. Wang, X. Li, G. Lu, X. Quan, G. Chen, Highly oriented 1-D ZnO nanorod arrays on zinc foil: direct growth from substrate, optical properties and photocatalytic activities, The Journal of Physical Chemistry C, 112 (2008) 7332-7336.

[216] C. Xu, L. Cao, G. Su, W. Liu, X. Qu, Y. Yu, Preparation, characterization and photocatalytic activity of Co-doped ZnO powders, Journal of Alloys and Compounds, 497 (2010) 373-376.

[217] J.M. Wu, C.-W. Fang, L.-T. Lee, H.-H. Yeh, Y.-H. Lin, P.-H. Yeh, L.-N. Tsai, L.-J. Lin, Photoresponsive and ultraviolet to visible-light range photocatalytic properties of ZnO: Sb nanowires, Journal of the Electrochemical Society, 158 (2011) K6-K10.

[218] Y. He, F. Grieser, M. Ashokkumar, The mechanism of sonophotocatalytic degradation of methyl orange and its products in aqueous solutions, Ultrasonics Sonochemistry, 18 (2011) 974-980.

[219] C. Ren, B. Yang, M. Wu, J. Xu, Z. Fu, T. Guo, Y. Zhao, C. Zhu, Synthesis of Ag/ZnO nanorods array with enhanced photocatalytic performance, Journal of Hazardous Materials, 182 (2010) 123-129.

[220] E. Grabowska, J. Reszczyńska, A. Zaleska, Mechanism of phenol photodegradation in the presence of pure and modified-TiO2: A review, Water Research, 46 (2012) 5453-5471.

[221] R.J. Schmidt, Industrial catalytic processes—phenol production, Applied Catalysis A: General, 280 (2005) 89-103.

[222] N. Calace, E. Nardi, B.M. Petronio, M. Pietroletti, Adsorption of phenols by papermill sludges, Environmental Pollution, 118 (2002) 315-319.

[223] A. Arques, A.M. Amat, A. García-Ripoll, R. Vicente, Detoxification and/or increase of the biodegradability of aqueous solutions of dimethoate by means of solar photocatalysis, Journal of Hazardous Materials, 146 (2007) 447-452.

[224] Y.B. Acar, H. Li, R.J. Gale, Phenol removal from kaolinite by electrokinetics, Journal of geotechnical engineering, 118 (1992) 1837-1852.

[225] J.D. Rodgers, W. Jedral, N.J. Bunce, Electrochemical oxidation of chlorinated phenols, Environmental Science & Technology, 33 (1999) 1453-1457.

[226] G.C. Yang, Y.-W. Long, Removal and degradation of phenol in a saturated flow by in-situ electrokinetic remediation and Fenton-like process, Journal of Hazardous Materials, 69 (1999) 259-271.

[227] A.S. Whiteley, M.J. Bailey, Bacterial community structure and physiological state within an industrial phenol bioremediation system, Applied and environmental microbiology, 66 (2000) 2400-2407.

[228] A.a.H. Al-Muhtaseb, K.A. Ibrahim, A.B. Albadarin, O. Ali-Khashman, G.M. Walker, M.N. Ahmad, Remediation of phenol-contaminated water by adsorption using poly (methyl methacrylate)(PMMA), Chemical Engineering Journal, 168 (2011) 691-699.

[229] E. Riser-Roberts, Remediation of petroleum contaminated soils: biological, physical, and chemical processes, CRC Press, 1998.

[230] M. Pera-Titus, V. García-Molina, M.A. Banos, J. Giménez, S. Esplugas, Degradation of chlorophenols by means of advanced oxidation processes: a general review, Applied Catalysis B: Environmental, 47 (2004) 219-256.

[231] E.J. Rosenfeldt, K.G. Linden, Degradation of endocrine disrupting chemicals bisphenol A, ethinyl estradiol, and estradiol during UV photolysis and advanced oxidation processes, Environmental Science & Technology, 38 (2004) 5476-5483.

[232] M. Antonopoulou, E. Evgenidou, D. Lambropoulou, I. Konstantinou, A review on advanced oxidation processes for the removal of taste and odor compounds from aqueous media, Water Research, (2014).

[233] V.K. Gupta, R. Jain, A. Mittal, T.A. Saleh, A. Nayak, S. Agarwal, S. Sikarwar, Photo-catalytic degradation of toxic dye amaranth on TiO2/UV in aqueous suspensions, Materials Science and Engineering: C, 32 (2012) 12-17.

[234] L.G. Devi, K.E. Rajashekhar, A kinetic model based on non-linear regression analysis is proposed for the degradation of phenol under UV/solar light using nitrogen doped TiO2, Journal of Molecular Catalysis A: Chemical, 334 (2011) 65-76.

[235] V. Kavitha, K. Palanivelu, The role of ferrous ion in Fenton and photo-Fenton processes for the degradation of phenol, Chemosphere, 55 (2004) 1235-1243.

[236] I. Udom, Zhang Y., Ram, M. K., Stefanakos, E. K., Hepp, A. F., Elzein, R., Schlaf, R., Goswami, D. Y., A simple photolytic reactor employing Ag-doped ZnO nanowires for water purification, Thin Solid Films, (2014).

[237]   P.R. Shukla, S. Wang, H.M. Ang, M.O. Tadé, Photocatalytic oxidation of phenolic compounds using zinc oxide and sulphate radicals under artificial solar light, Separation and Purification Technology, 70 (2010) 338-344.

[238]   C.-H. Chiou, R.-S. Juang, Photocatalytic degradation of phenol in aqueous solutions by Pr-doped TiO2 nanoparticles, Journal of Hazardous Materials, 149 (2007) 1-7.

[239]   D.F. Ollis, E. Pelizzetti, N. Serpone, Photocatalyzed destruction of water contaminants, Environmental Science & Technology, 25 (1991) 1522-1529.

[240]   S. Lathasree, A.N. Rao, B. SivaSankar, V. Sadasivam, K. Rengaraj, Heterogeneous photocatalytic mineralisation of phenols in aqueous solutions, Journal of Molecular Catalysis A: Chemical, 223 (2004) 101-105.

[241]   F. Akbal, A. Nur Onar, Photocatalytic Degradation of Phenol, Environ Monit Assess, 83 (2003) 295-302.

APPENDICES

Appendix A Copyright Permissions

A.1 Permission for Use of Material in Abstract

A.2 Permission for Use of Material in Chapter 1

A.3 Permission for Use of Material in Chapter 2

Permission to use the" Enhanced TiO2" work

3 messages

Innocent Udom <iudom@mail.usf.edu>   Tue, Jun 10, 2014 at 8:45 AM
To: "Hepp, Aloysius F. (GRC-REB0)" <Aloysius.F.Hepp@nasa.gov>
Bcc: "Prof. Hepp" <profhepp@yahoo.com>

Al - How do I get the permission to use the work **"Enhanced TiO2 Photocatalytic Processing of Organic Wastes for Green Space Exploration"**, as a portion in my dissertation. Please let me know.

Thanks,

Innocent

Hepp, Aloysius F. (GRC-REB0) <aloysius.f.hepp@nasa.gov>   Tue, Jun 10, 2014 at 9:10 AM
To: Innocent Udom <iudom@mail.usf.edu>

Hi Innocent,

As a result of being a "declared work of the U.S. Government," and the fact that you were part of the project as a result of being a NASA-funded student, you are certainly entitled to include this work in your thesis.

How is everything going?

All the best,

Al

Aloysius F. Hepp, Ph.D.
Senior Scientist
NASA John H. Glenn Research Center at Lewis Field
MS 302-1
21000 Brookpark Rd.
Cleveland, OH 44135
P: (216) 433-3835
F: (216) 433-6106
C: (440) 720-4377
E: Aloysius.F.Hepp@nasa.gov
----- ----- ----- ----- ----- ----- ----- ----- ----- -----
"Chemistry is all about getting lucky."
Robert Curl (1996 Nobel Laureate)

From: Innocent Udom <iudom@mail.usf.edu>
Date: Tuesday, June 10, 2014 8:45 AM
To: "A.F. Hepp" <Aloysius.F.Hepp@nasa.gov>
Subject: Permission to use the" Enhanced TiO2" work

A.4 Permission for Use of Material in Chapter 3

A.5 Permission for Use of Material in Chapter 4

98

Appendix B Supplemental Data
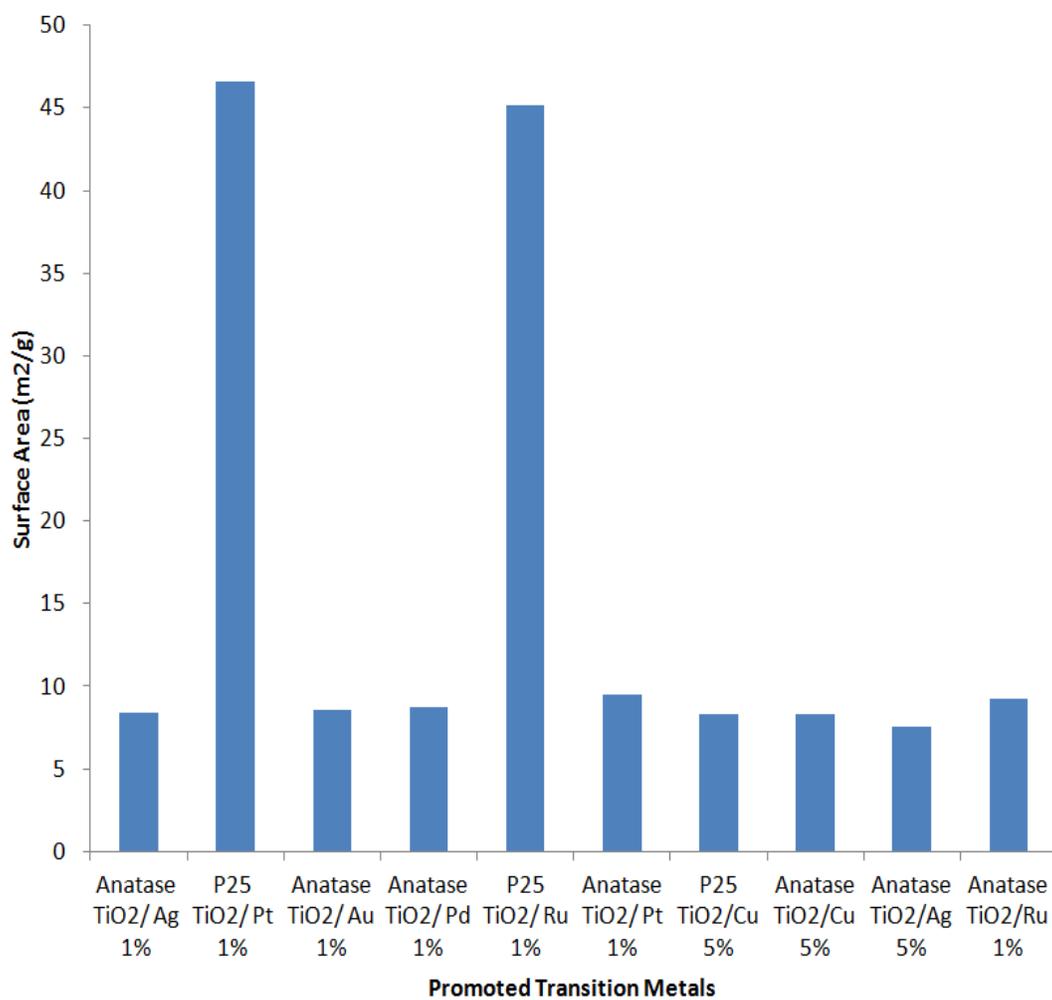
Figure B.1 Surface area measurements of all the photo catalysts
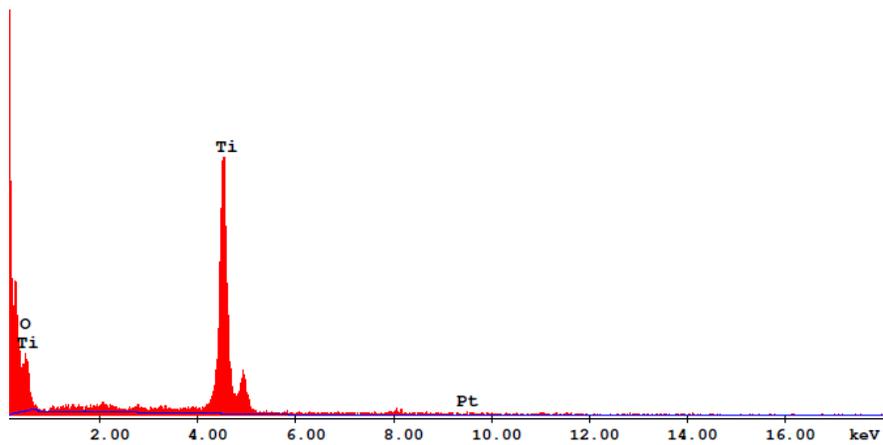
Figure B.2 EDS graphical elemental composition analysis of anatase TiO_2/Pt 1%
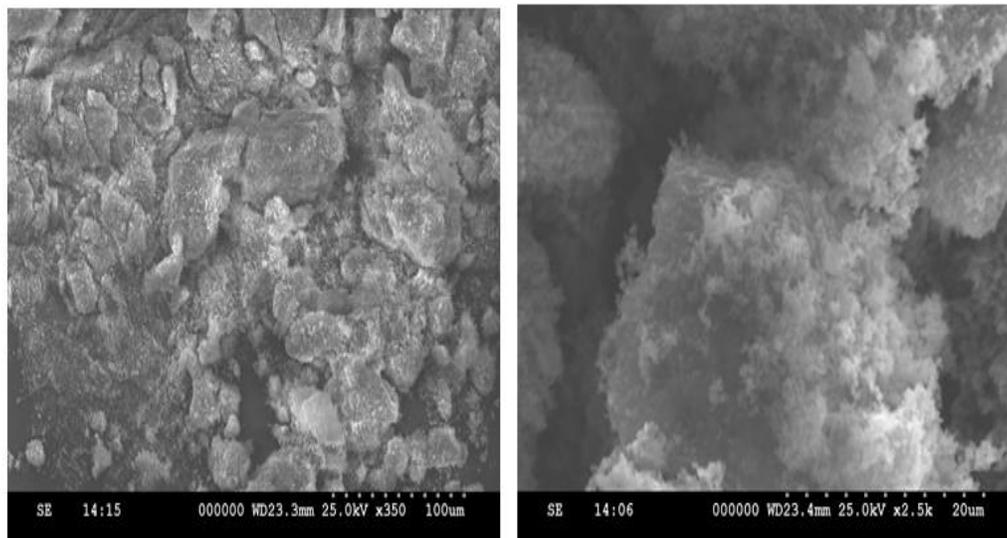
Figure B.3 Topographical images of photocatalyst made of anatase TiO_2/Pt 1%
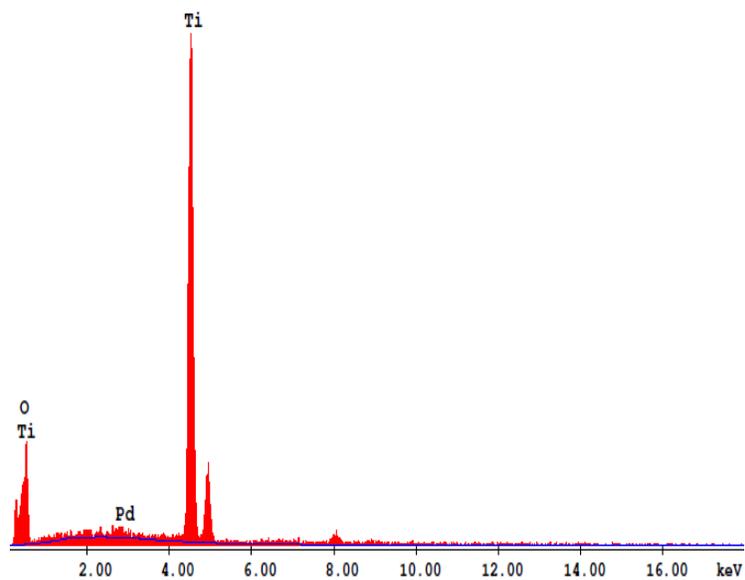
Figure B.4 EDS graphical elemental composition analysis of anatase TiO_2/Pd 1% photocatalyst (MDM-2-Pd 1%)
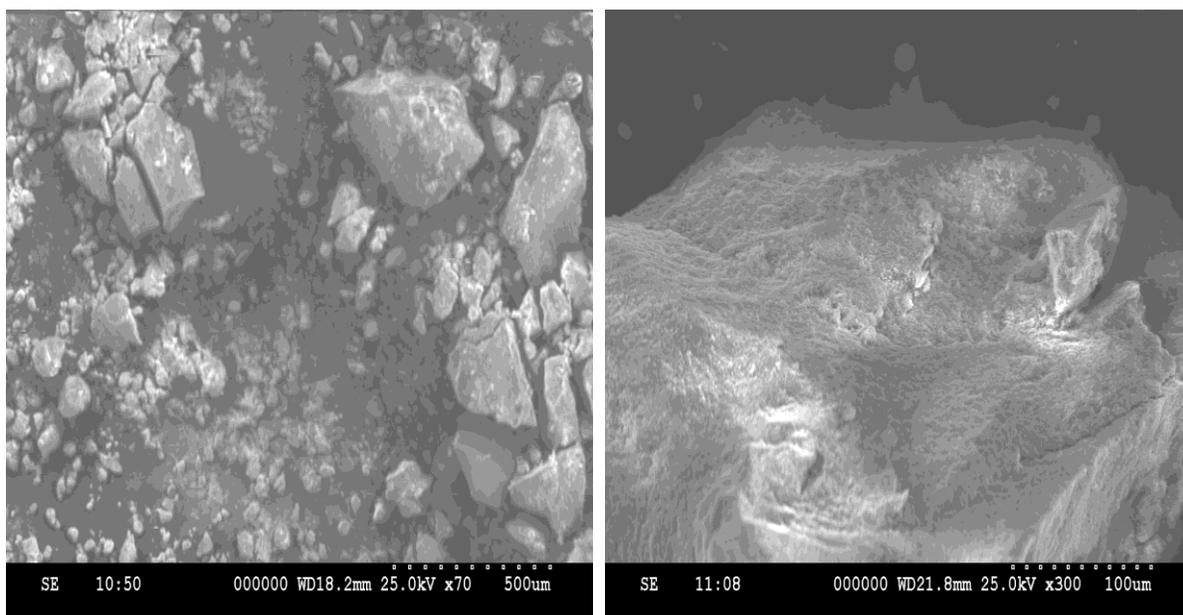
Figure B.5 Topographical images of photocatalyst made of anatase TiO_2/Pd 1%
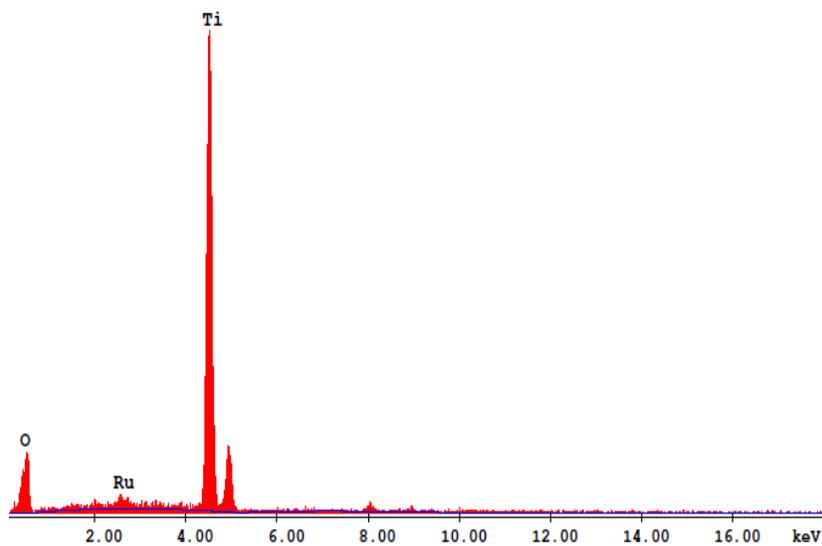
Figure B.6 EDS graphical elemental composition analysis of anatase TiO_2/Ru 1% photocatalyst (MDM-3-Ru 1%)
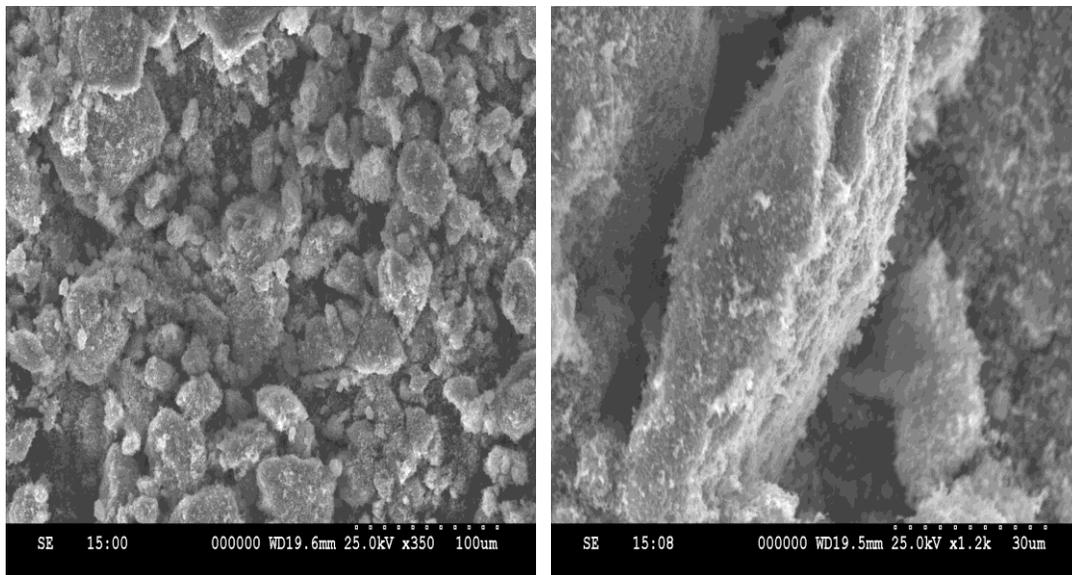
Figure B.7 Topographical images captured of anatase TiO_2/Ru 1%
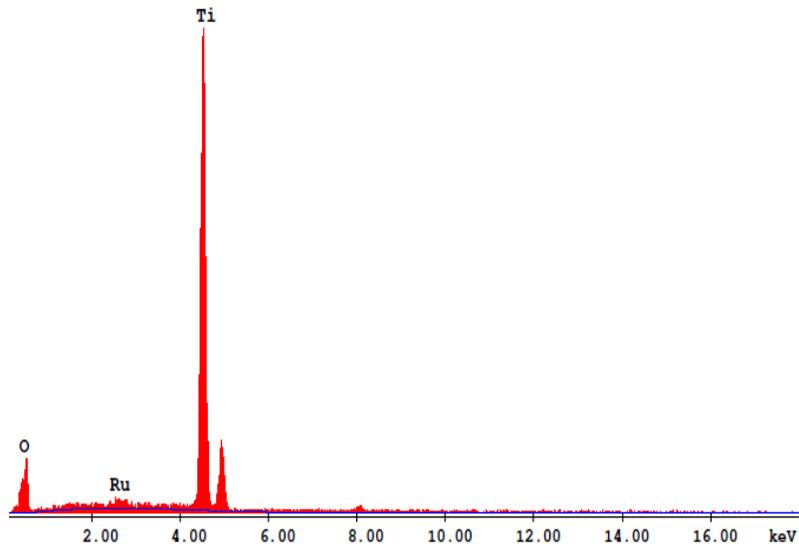
Figure B.8 EDS catalyst elemental composition of photocatalyst made of P25 TiO$_2$/Ru 1%
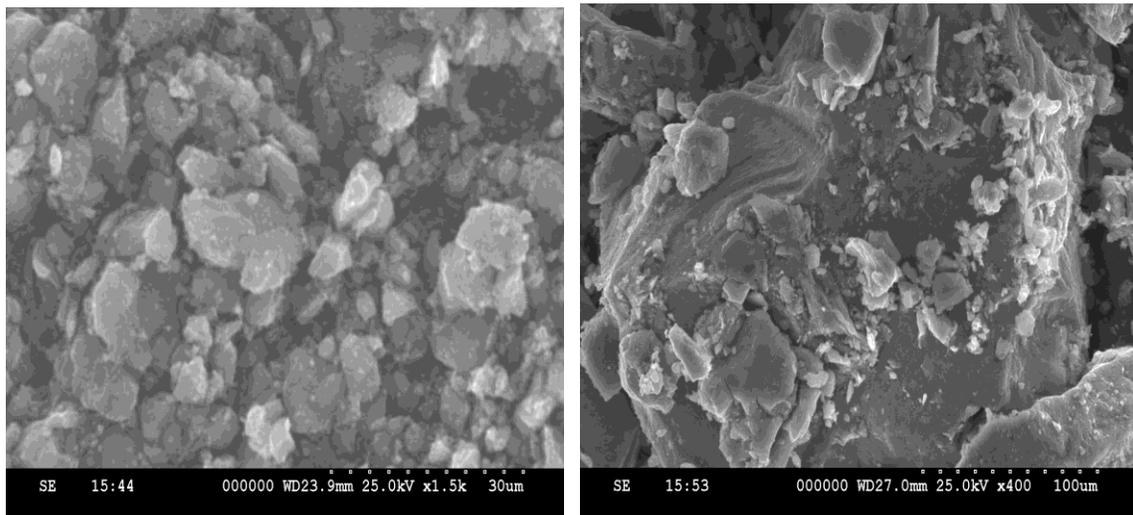
Figure B.9 Topographical images of photocatalyst made of P25 TiO$_2$/Ru 1%
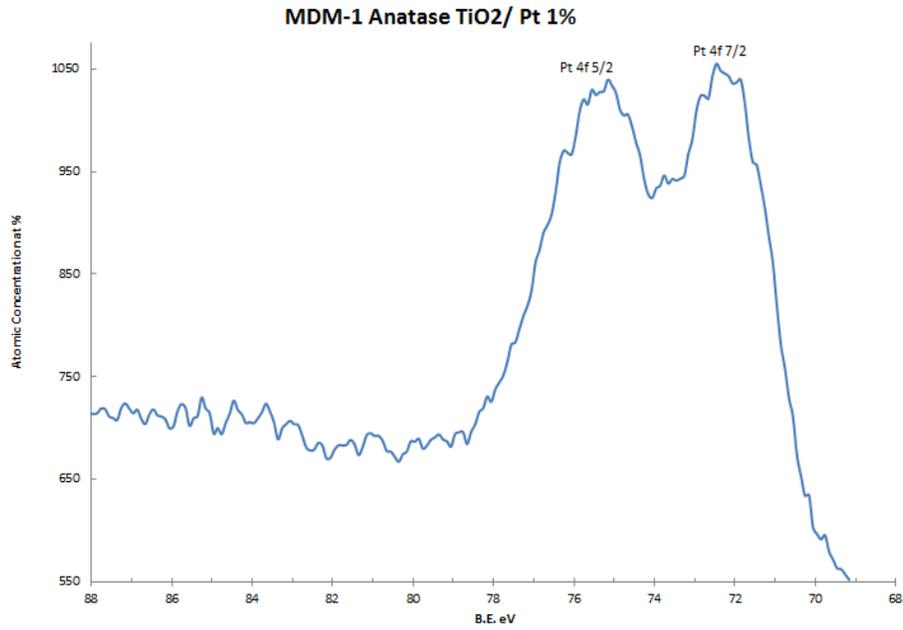
Figure B.10 XPS data for anatase titanium/Pt 1%
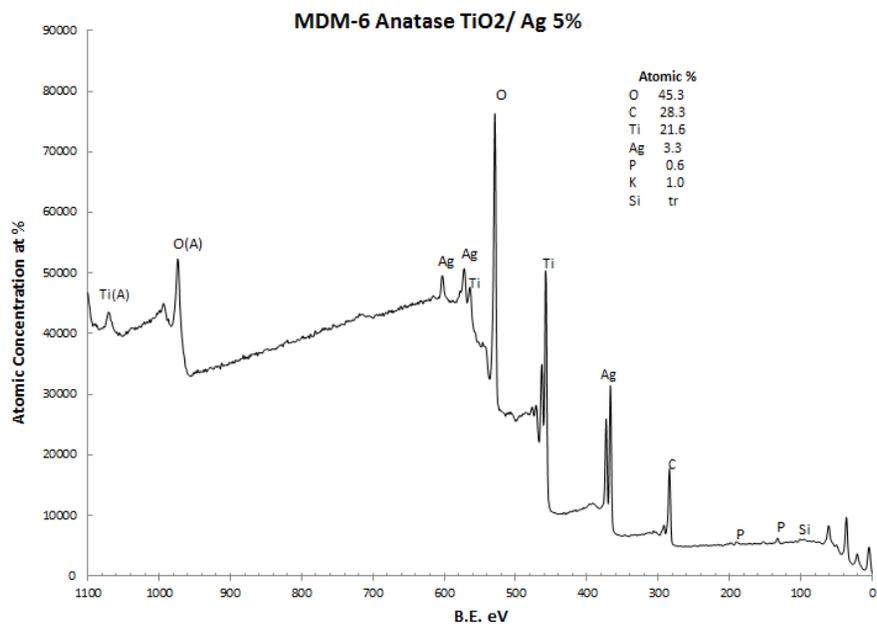
Figure B.11 XPS data for anatase titanium/Ag 5%
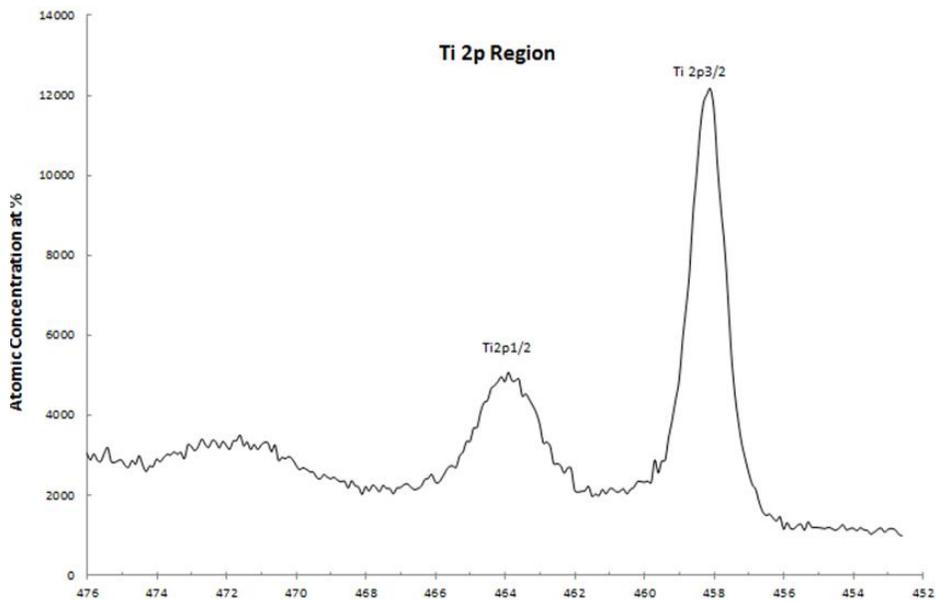
Figure B.12 XPS data for titanium/Ag 5% (Ti 2p region)
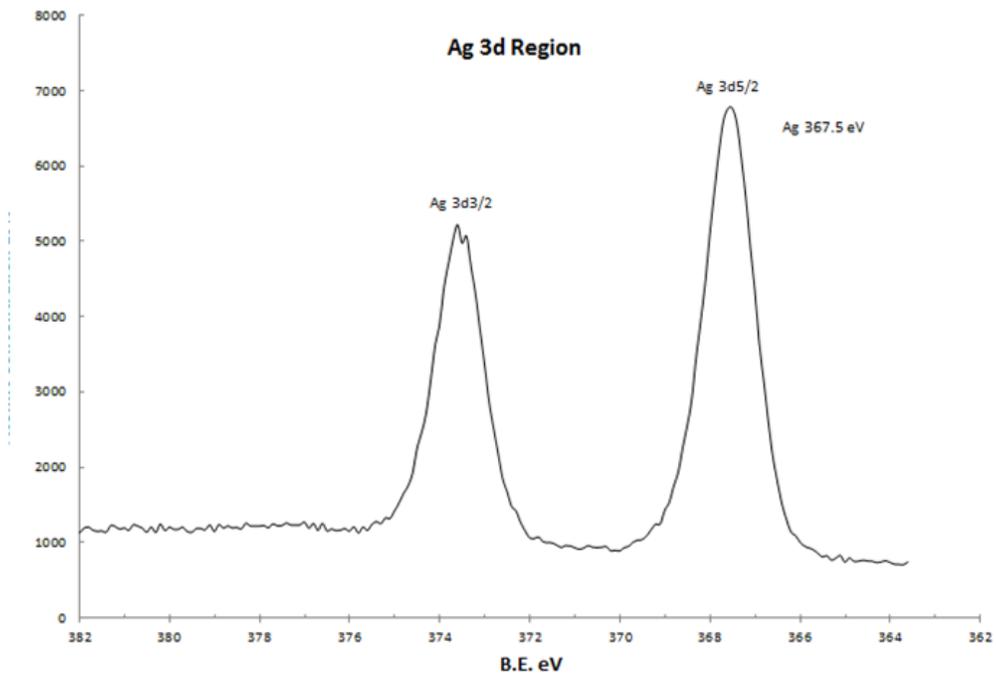
Figure B.13 XPS data for anatase TiO2/Ag 5% (Ag 3d region)